論文 / 著書情報
Article / Book Information

題目(和文)	
Title(English)	Elucidating the Influence of Carbonaceous Electrodes and Metal/Metal Oxide Promoters in Non-aqueous Li-O2 Batteries
著者(和文)	Wong Raymond Albert
Author(English)	Raymond Wong
出典(和文)	学位:博士(工学), 学位授与機関:東京工業大学, 報告番号:甲第10525号, 授与年月日:2017年3月26日, 学位の種別:課程博士, 審査員:脇 慶子,金 有洙,肖 鋒,沖野 晃俊,平山 雅章,田巻 孝敬
Citation(English)	Degree:Doctor (Engineering), Conferring organization: Tokyo Institute of Technology, Report number:甲第10525号, Conferred date:2017/3/26, Degree Type:Course doctor, Examiner:,,,,,
学位種別(和文)	博士論文
Type(English)	Doctoral Thesis

Elucidating the Influence of Carbonaceous Electrodes and Metal/Metal Oxide Promoters in Non-aqueous Li-O_2 Batteries

Doctoral thesis

by

Raymond A. Wong

Tokyo Institute of Technology

Interdisciplinary Graduate School of Science and Engineering

Department of Energy Sciences

Abstract

The realization of electrochemical energy storage with ultra-high energy densities is one of the most pressing needs in the area of transportation and renewable energy. Amongst post Li-ion batteries, the non-aqueous lithium-oxygen (Li-O_2) battery is very attractive as it processes the very high theoretical specific energy (~3.5 kWh kg^{-1}), one of the highest of all battery chemistries. The ideal electrochemistry of gaseous oxygen and lithium ions in an aprotic electrolyte yields the reversible reaction, $2Li^+ + O_2 + 2e^- \leftrightarrow Li_2O_2$ (E^o = 2.96 V vs Li/Li^+), with insoluble and insulating Li_2O_2 forming as the discharge product. The Li-O_2 is still much in its infancy with its many challenges and our approach is to investigate this potential next generation battery chemistry in the following ways:

In Chapter 1, the broader context of the present work relating to global warming and climate change acting as an impetus for the improvement in electrochemical energy storage is introduced. Additionally, related background on electrochemistry, redox reactions, and the dependence of energy density on battery chemistry is introduced. The central topic of the thesis relating to Li-O_2 batteries is discussed including the discharge and recharge electrochemistry, and the current shortcomings, challenges and which are hampering Li-O_2 battery development consisting of electrolyte and electrode instability, poor reversibility and cycleability, low rate capability and lower-than-theoretical capacity.

In Chapter 2, the experimental methods used throughout this thesis is elaborated upon, the electrochemical cells, testing conditions, and post-mortem analysis techniques. Our analyses can be separated into three categories, where we complement standard electrochemical testing with (1) morphological (2) chemical and (3) quantitative analysis. Our approach of correlating these three characterisation aspects allows for a much more complete picture of the processes occurring in our Li-O_2 cells. Of particular emphasis is

quantitative *in situ* on-line electrochemical mass spectrometry (OEMS) to evaluate gas evolution and reversibility. We discuss the construction and utilization of OEMS including the operating principles and importance within the Li-O_2 battery field.

In Chapter 3, we highlight the importance of carbon surface chemistry towards the behavior of Li-O_2 cells by systematically investigating the role of surface properties by decoupling oxygen functional groups, defective edges, and graphitization in carbon nanotubes. Our findings show that discharge capacity is enhanced with the increasing degree of order and uniformity of the carbon surfaces causing an absence of nucleation sites and bias towards solvation-based nucleation and growth of Li_2O_2. The subsequent recharge potential is predominantly dependent on the Li_2O_2 structure formed from the preceding discharge, where the presence of oxygen-functional groups promotes the formation of amorphous Li_2O_2 which can more facilely decompose in comparison to crystalline Li_2O_2. The highly active oxygen-functional groups and defective edges, however, inactivate during cycling, providing insights into future strategies regarding enhancement of chemical stability as electrode platform. Our study provides improved understanding of the general role of carbonaceous electrode surfaces towards discharge capacity, the notorious rise in recharge potential and stability.

In Chapter 4, we address the controversial issue regarding the use of nanostructured metal and metal oxides towards mitigating the large polarization (>1 V) observed on recharge. The origin of the large recharge overpotential has been attributed to the sluggish kinetics of Li_2O_2 decomposition and also concurrent parasitic side reactions arising from electrolyte and carbon electrode degradation forming side products which require high potential to decompose (> 4 V). We have synthesized metal and metal-oxide nanoparticles (NPs) of Au, Pt, Pd, Ru and Co_3O_4 on carbon nanotubes to investigate their efficacy in reducing the recharge overpotential, the predominant processes occurring during cell operation and lastly, the probable reasons for the observed behavior. We identify that while the metal/metal oxide

NPs (exception is Au) reduce the recharge overpotential with Ru exhibiting the lowest recharge potential. More importantly, we reveal that the reduced overpotential is not accompanied by an increase in reversibility with all metal/metal oxide materials exhibiting ~60% O_2 reversibility. Our findings also identify that that metal/metal oxide NPs (in particular Pt and Ru) have activity toward electrolyte oxidation. Lastly, we further extend this study to examine the effect of particle size, where our results indicate that when the NP particle size is <10 nm, there is a relatively weak correlation between recharge potential and NP size. Our findings indicate that metal and metal oxide NPs do not mitigate the underlying issue of reversibility affirming the need to identify electrolyte and electrode materials that promote reversible Li-O_2 electrochemistry.

In Chapter 5, we conclude this thesis with a broader perspective of the lessons learned within the Li-O_2 battery field and potential directions for future work. Lessons learned is highlighted by the importance of a comprehensive array of characterization techniques with the emphasis on quantitative analysis which allows for a fuller picture of the process occurring in Li-O_2 cells. Recent developments occuring after the experimental work of this thesis was completed, is mentioned including the detection of singlet oxygen, and the potential promising development of molten nitrate electrolytes.

Table of Contents

List of abbreviations

ADC	analog-to-digital converter
AN	acceptor number (measure of Lewis acidity)
CNT	carbon nanotube (can denote multi-walled carbon nanotube)
COP21	21st conference of the parties
DC	discharge
DEMS	differential electrochemical mass spectrometry (in situ technique)
DME	dimethoxyethane, also referred to as monoglyme (solvent)
DN	donor number (measure of Lewis basicity)
DMSO	dimethyl sulfoxide (solvent)
EPR	electron paramagnetic resonance
PEY	partial electron yield (XANES detection mode)
PFY	partial florescence yield (XANES detection mode)
GC/MS	gas chromatography-mass spectrometry
GF	glassfibre (battery separator material)
HOMO	highest occupied molecular orbital
HSAB	hard soft acid base theory
LiTFSI	lithium bis(trifluoromethane)sulfonamide (Li salt)
LUMO	lowest unoccupied molecular orbital
LSV	linear sweep voltammetry or voltammogram (electrochemical technique)
M(O)	metal and metal oxide
MWNT	multi-walled carbon nanotube (material)
NP	nanoparticle
OEMS	on-line electrochemical mass spectrometry (in situ technique)
OER	oxygen evolution reaction
ORR	oxygen reduction reaction
PVDF	polyvinylidene fluoride (polymer for binder)
RC	recharge
RRDE	rotating ring disk electrode (electrochemical method)
SEI	solid-electrolyte interface (electrode/electrolyte interface)

SEM	scanning electron microscopy
TBA^+	tetrabutylammonium ion
TEM	transmission electron microscopy
TEY	total electron yield (XANES detection mode)
TGA	thermogravimetric analysis
VI	virtual instrument (LabVIEW interface)
XANES	X-ray absorption near edge structure
XPS	X-ray photoelectron spectroscopy
XRD	X-ray diffraction

Acknowledgements

I am grateful for the guidance, support and patience I have received from Prof. Keiko Waki, Prof Hye Ryung Byon and Prof Yousoo Kim. I also indebted to my labmates including Drs. Misun Hong, Arghya Dutta, Morgan Thomas, Chunzhen Yang, Georgios Nikifordis, Haryo Oktaviano, Ms. Nadege Bonnet-Mercier and many others who have supported and mentored me during my time at Byon lab, Waki lab and Kim lab. The opportunities given and the different perspectives I experienced, along with the many wonderful people I had the absolute pleasure in working with made the experience truly enjoyable. Essentially I was part of *four* laboratories starting with Byon Initiative Research Unit at RIKEN and Waki laboratory at Tokyo Tech concurrently, then participating in the launch of the Byon lab at KAIST in Korea and finally returning back to RIKEN and joining the Surface and Interface Science Laboratory (SISL).

Chapter 4 of this thesis was a collaborative project within the group with the notable contribution from Drs Chunzhen Yang and Arghya Dutta with the synthesis of the metal and metal oxide nanoparticles used in the study and their related characterisations. The XANES studies presented in this thesis was performed by Keisuke Yamanaka and Prof. Toshiaki Ohta at the SR Center in Ritsumeikan University. Their contribution is greatly appreciated.

Raymond A. Wong

November 2016

Chapter 1

Introduction

1.1 – Importance of sustainable energy conversion and storage

Fossil fuels have served humanity for the past 200 years, providing an impetus for unprecedented development.[1,2] As an unintended consequence, continuous CO_2 emissions has led to critical issues relating to global warming and climate change.[1] In response, the recent 21st Conference of the parties (COP21) also known as the Paris agreement in 2016 [3,4] is an important attempt at mitigating the effects of further global warming. The major aim of this agreement is to limit global warming "to well below 2^{o}C and pursue efforts to limit the temperature increase to 1.5^{o}C."[4] These aggressive targets that will require significant innovation to change the status quo of how we produce, distribute and use energy.[5]

The most critical challenge is the intricate relationship between energy creation and energy consumption. Assuming that effective energy storage for grid-level and transportation is implemented, if the energy is not harvested from sustainable sources, the issue of CO_2 emissions is completely mitigated. **Figure 1.1a** shows the world's energy source where oil, coal and gas continue to be the dominant sources of energy with renewables consisting of less than 5% of energy production and needs to be vastly increased.[1] The intermittent nature of many renewables (ie. solar and wind) inherently causes the balance between energy supply and demand to be extremely challenging, thus makes effective grid level storage a necessary component.[6] Also important is the transportation sector which constitutes a significant source of CO_2 emissions (16% of direct emissions in Japan)[7] (**Figure 1.1b**) and more in automobile intensive countries (26% of emissions for the US).[8] For mobile applications

there are strict requirements not only on cost but also gravimetric and volumetric energy densities due to the limitation of space.[9] While continued efforts should be made towards steady incremental gains, there is the immense need for the realization of disruptive energy storage and conversion technologies with extremely high gravimetric and volumetric energy densities at levels that rival fossil fuels.

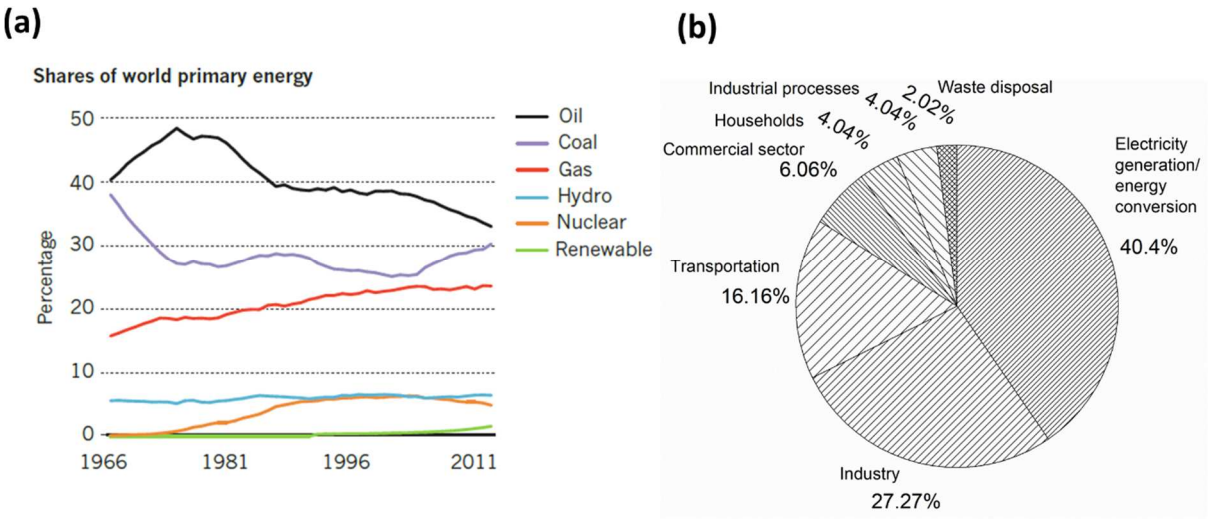

Figure 1.1 – The low energy production from renewables and current influence of CO_2 emissions in transportation sector (a) Percentage breakdown of energy sources in the world.[1] (b) Breakdown of direct CO_2 emissions within Japan with transportation consisting of roughly 16% of CO_2 emissions.[7]

1.2– Background on batteries

Batteries are electrochemical energy storage devices that convert chemical energy into electricity. In terms of definitions, primary batteries are defined as batteries that are only capable of discharge (DC) while on the other hand, batteries capable of being recharged (RC), are referred to as secondary batteries. Batteries offer many advantages to conventional energy storage and conversion technologies (ie. fossil fuels), such as no mechanically moving parts, relative compactness, ability to operate in the absence of air (dependant on chemistry), and

more importantly if utilizing renewable source of energy the overall environmental footprint is relatively low.

Batteries consist of three components which are the negative electrode, positive electrode and ion conducting media (electrolyte). During DC, the negative electrode or anode undergoes oxidation and provides electrons to the external circuit. The positive electrode or cathode, undergoes reduction and accepts the incoming electrons from the external circuit. Conversely upon recharge the electrodes reverse roles with the negative electrode becoming the cathode and the positive electrode as the anode. The electrolyte (liquid or solid) allows the movement of charged ions between the two electrodes. Note that in terms of terminology, the convention is that negative and positive electrodes do not change, however, the anode and cathode terms do change depending on the electrode where oxidation and reduction occur, respectively. To avoid confusion, through this thesis, the term negative and positive electrode will be used.

Regarding thermodynamics, given two electrodes where reduction and oxidation occur in an electrochemical cell (in a generic cell):

Reduction in the forward direction: $a\mathrm{A} + ne \leftrightharpoons c\mathrm{C}$

Oxidation in the forward direction: $b\mathrm{B} \leftrightharpoons d\mathrm{D} + ne$

Overall: $a\mathrm{A} + b\mathrm{B} \leftrightharpoons c\mathrm{C} + d\mathrm{D}$

The change in Gibbs free energy (ΔG), defined as the amount of obtainable work (in kJ) is determined by the relation:

$$\Delta G = -nFE^{o},$$

Where n is the electron number (unitless), F is Faraday's constant (96 500 C mol^{-1}) and E^{o} is the standard potential (V) or electromotive force (emf) of the cell. Given that ΔG is that

difference in energy between the reactants and products, negative ΔG indicates the relative spontaneity (when products are lower in energy than reactants). E^o of the cell is the net potential of reduction and oxidation reactions occurring at the anode and cathode, respectively:

$$E^o = E_{reduction} + E_{oxidation}$$

Therefore, E^o governs ΔG in determining spontaneity with respect to the forward reaction (E^o >0 means the reaction is spontaneous in the forward direction, and $E^o < 0$ means not spontaneous in the forward direction). This definition the standard potential (E^o) is applicable for standard conditions defined as 1M in concentration and at 1 atm. The complete definition of the cell emf (denoted as *E*) for non-standard conditions includes additional parameters such as temperature and the activity of the chemical species in the cell and is given by the relation referred to as the Nernst equation:

$$E = E^o - \frac{RT}{nF} \ln Q$$

Where *R* is the gas constant (8.314 J mol^{-1} K^{-1}), *T* is temperature (K), and *Q* is the reaction quotient.

Aside from thermodynamics defining the cell emf (*E*), from the practical point of view, electrode reactions do not occur at the potential value determined by the Nernst equation due the involvement of parameters influencing the kinetics or rate of electrode reactions (**Figure 1.2**). The difference between cell emf (E) from Nernst equation and the observed potential (E_{actual}) is known as overpotential (denoted as η) in the relation:

$$\eta = E - E_{actual}$$

The aggregate of all potential losses is referred to as the overpotential. Overpotential can be further separated into individual losses in the steps involved with the redox reaction (**Figure**

1.2),[10] including (1) mass transport of reactants from the bulk to electrode, (2) adsorption/desorption of reactants/products, (3) losses associated with electron transfer and (4) possible chemical reactions before/after electron transfer.

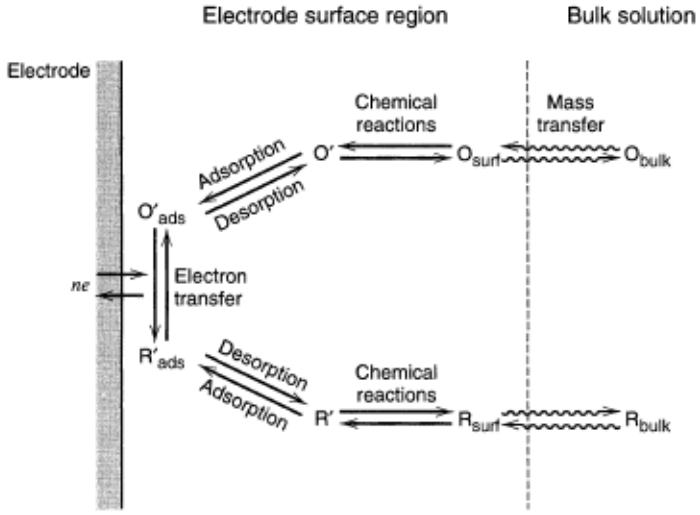

Figure 1.2 – More detailed diagram of the electrode processes involving mass transport, possible chemical reactions, adsorption/desorption of reactants/products, and charge transfer.[10]

The common figure of merit used in the electrochemical energy storage field is gravimetric energy (energy per unit mass, (Ah kg^{-1})) and volumetric energy density (energy per unit volume (Ah L^{-1})). From a practical point of view, higher energy densities are desired as this will allow for smaller and lighter devices with implications relating to driving range for EVs, and smaller and more compact power tools and electronic devices. Therefore, for any given active material, theoretical gravimetric capacity can be determined

Theoretical gravimetric capacity: $\rho = \left(\frac{F \times n}{M}\right)\ [Ah\ kg^{-1}]$

Theoretical specific energy: $(\rho \times E^o)\ [Wh\ kg^{-1}]$

Where, F is Faraday's constant (96500 C mol^{-1} or 26.81 Ah mol^{-1}), n is the electron number (unitless), M is the molar mass of the active material (kg mol^{-1}), and E^o is the standard

potential (V). From this, the volumetric specific energy can also be determined based on the given density of the active materials. Taking for example $LiCoO_2$, as the representative Li-ion battery positive electrode material, its theoretical capacity equates to ~274 mAh g^{-1} (Although note that only 0.5 electrons per unit formula can be reversibly intercalated meaning ~137 mAh g^{-1}) leading to theoretical specific energy of ~500 Wh kg^{-1} when considering just $LiCoO_2$ (**Figure 1.3**). Taking this together with the graphite negative electrode ($(Li)C_6$ at ~370 mAh g^{-1}) leads to a theoretical specific energy of ~400 Wh kg^{-1} for Li-ion batteries.[11] In terms of the active materials, the cobalt (Co^{3+}/Co^{4+} redox couple) provides charge compensation which means that the oxide component for the positive electrode and carbon on the negative electrode are in a sense 'inactive' and do not constructively contribute to energy density. Additionally, from a practical sense, batteries typically require many inactive components (ie. separator, casing, electrolyte, binders, current collectors, additional safety features and electronics), which lowers the actual specific energy of practical systems. Therefore, typical values for practical Li-ion batteries its ~150 Wh kg^{-1} (**Figure 1.3**).[11]

Strictly in terms of theoretical specific energy, one can quickly determine that the two elements lithium and oxygen will be very attractive. Accordingly, amongst post Li-ion battery chemistries (**Figure 1.3**), lithium-oxygen ($Li\text{-}O_2$) is extremely appealing due to the theoretical gravimetric density and specific energy (based on Li_2O_2) equating to 1169 Ah kg^{-1} and ~3.5 kWh kg^{-1}, respectively. While practical values for the projected specific energy for $Li\text{-}O_2$ batteries ranges from 200 Wh kg^{-1}[12] to highly optimistic estimates of up to 1700 Wh kg^{-1}.[11]

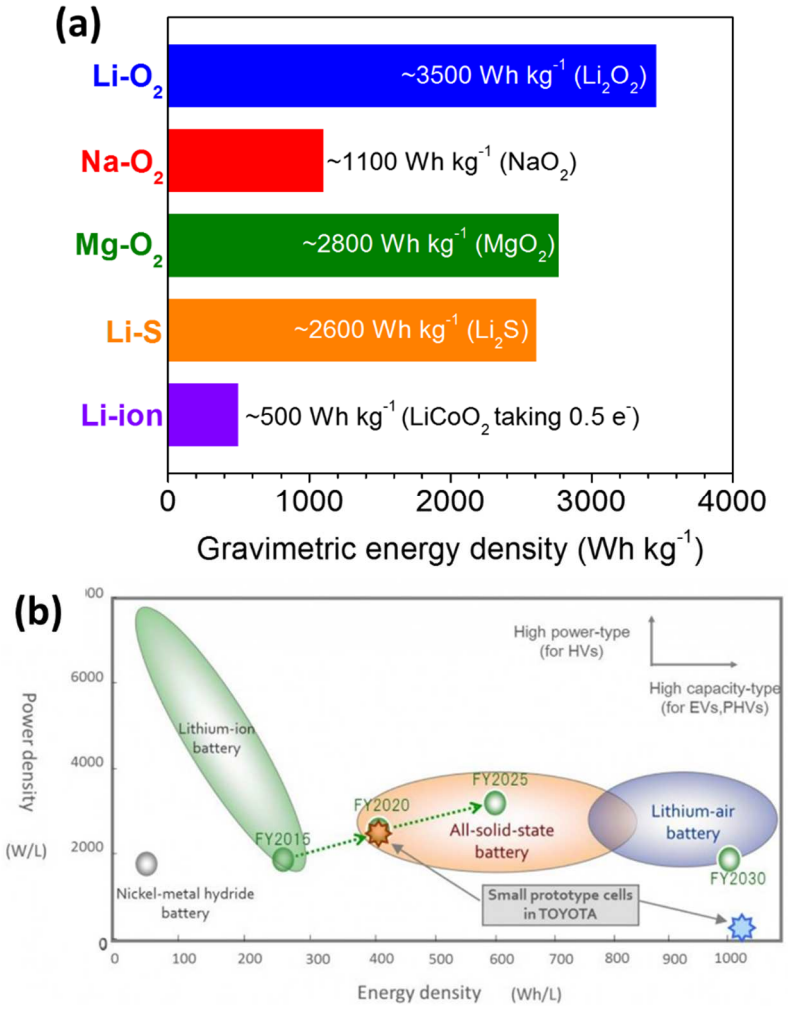

Figure 1.3 – (a) Comparison of various post Li-ion battery and Li-ion chemistries in terms theoretical and practical gravimetric energy densities.[11] (b) Ragone plot (power density versus energy density) and the battery development roadmap from Toyota Motor Corporation.[13]

1.3 - Lithium-oxygen ($Li-O_2$) batteries

The first published report of the Li-air battery is attributed to Abraham and Jiang in 1996.[14] In terms of nomenclature, "Li-air" batteries refers to utilizing mixtures of gas, where O_2 is a component or this simply means unpurified atmospheric air. On the other hand, "$Li-O_2$ batteries" refers to operation under a pure O_2 environment. The scope of this thesis deals with $Li-O_2$ batteries utilizing pure O_2 and as a result the term $Li-O_2$ is used. Additionally, it should be noted that there are other types of $Li-O_2$ batteries including hybrid (involving separated aqueous and non-aqueous compartments), solid state electrolyte

involving , and aprotic Li-O_2 batteries.[15,16] However, the scope of this thesis is on aprotic (non-aqueous) Li-O_2 batteries and the other Li-O_2 battery types will not be discussed further.

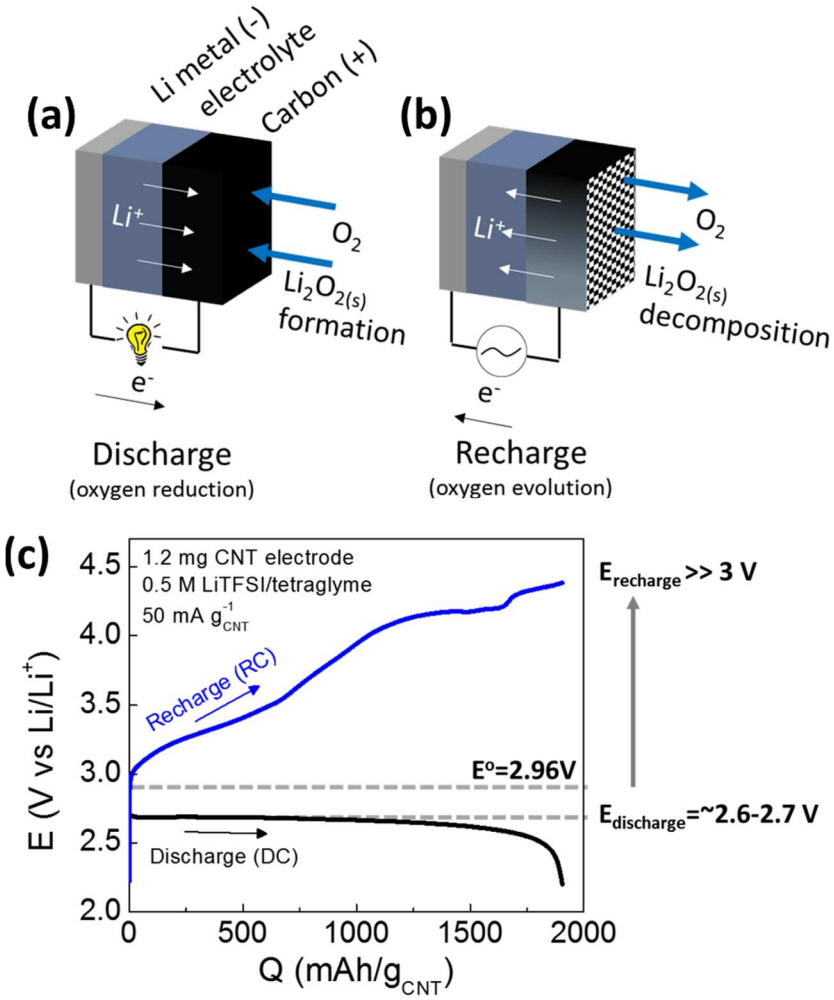

Figure 1.4 - Schematic of the non-aqueous Li-O_2 battery (a) Negative and positive electrodes consist of Li metal and carbon, respectively. During DC, oxygen reduction (ORR) occurs forming Li_2O_2 (b) On the subsequent recharge, Li_2O_2 decomposes and *via* oxygen evolution reaction (OER) (c) Representative galvanostatic (constant current) discharge-recharge (DC-RC) cycle of the Li-O_2 battery utilizing 0.5M LiTFSI/tetraglyme with current density of 50 mA g^{-1}.

The non-aqueous Li-O_2 battery (**Figure 1.4a-b**), consists of metallic Li as the negative electrode, an aprotic solvent containing dissolved Li salt, and the porous positive electrode, typically consisting of carbon. The discharge-recharge (DC-RC) reactions essentially involves three phases with O_2 gas and Li^+ ions dissolved in the electrolyte, forming solid and insulating Li_2O_2 as the DC product.[17,18] A representative galvanostatic

(constant-current) DC-RC cycle is shown in **Figure 1.4c**, with its characteristic features discussed further in the subsequent sections.

1.4 – Li-O_2 electrochemistry

The electrochemistry within the Li-O_2 framework are summarized in the equations below [17,19,20]:

Discharge (Oxygen reduction (ORR) and Li_2O_2 formation):

Negative (anode): $Li \rightarrow Li^+ + e^-$ (1)

Positive (cathode): $Li^+ + O_2 + e^- \rightarrow LiO_2$ (2)

$2LiO_2 \rightarrow Li_2O_2 + O_2$ (3) (chemical step)

$2LiO_2 + Li^+ + e^- \rightarrow Li_2O_2$ (4)

$Li_2O_2 + Li^+ + 2e^- \rightarrow Li_2O$ (5)

Discharge overall: $2Li + O_2 \rightarrow Li_2O_2$ $(E^o = 2.96\ V\ vs\ Li/Li^+)$ (6)

$4Li + O_2 \rightarrow 2Li_2O$ $(E^o = 2.91\ V\ vs\ Li/Li^+)$ (7)

Charge (Oxygen evolution (OER) and Li_2O_2 decomposition):

Negative (cathode): $Li^+ + e^- \rightarrow Li$ (8)

Positive (anode): $Li_2O_2 \rightarrow 2Li^+ + O_2 + 2e^-$ (9)

Charge overall: $Li_2O_2 \rightarrow 2Li + O_2$ (10)

The Li-O_2 electrochemistry operates with the oxygen-peroxide (O_2/O_2^{2-}) redox couple through an overall $2e^-$ transfer process. The formation of Li_2O_2 is analogous to the aqueous oxygen reduction (ORR) involving H_2O_2, with no cleavage of the O=O bond.[19,21] In contrast, however, the Li_2O_2 discharge product is an insoluble solid and is immobile once formed.[19] The negative electrode operates identically to typical Li-based batteries with lithium metal de-plating and plating with equation (1) and (8). The positive electrode operates

with the first ORR step yielding lithium superoxide (LiO_2) *via* equation (2). Aside from very few reports,[22,23] the overwhelming consensus is that the intermediate LiO_2 is not stable and reacts either through disproportionation with equation (3) or further reduction with reaction (4) to form the final discharge product, Li_2O_2 (see section 1.4.1 below).[24] Unlike aqueous ORR producing H_2O, despite having similar E^o at 2.91V, the formation of Li_2O *via* equation (5) is not kinetically favored within the operating potential (2 to 4.5 V) of Li-O_2 cells [19] which has been supported by techniques including X-ray diffraction, spectroscopic, pressure drop, and mass spectrometry measurements utilizing isotope labeled $^{18}O_2$ [25-27]. Lastly, to complete the reversible cycle, reaction (9) and (10) leads to Li_2O_2 decomposition to yield Li^+ and O_2 evolution.[17]

1.4.1 – Non-aqueous oxygen reduction and role of Li^+ ions

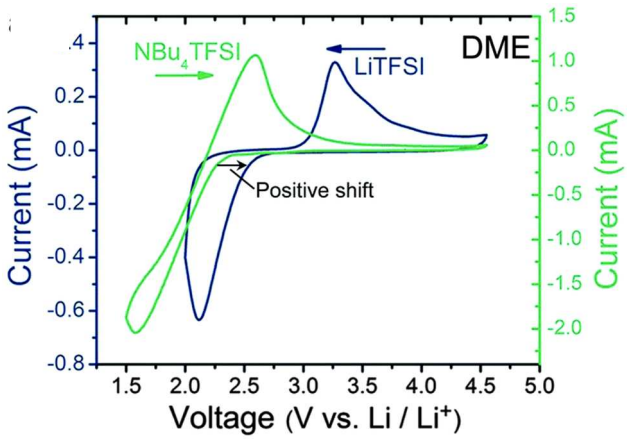

Figure 1.5 – Bulk 3-electrode cell with cyclic voltammogrammetry utilizing glassy carbon in saturated O_2 comparing 1M NBu_4TFSI and 1M LiTFSI in DME (dimethoxyethane).[28] The counter and reference electrodes are Li metal where in the case with NBu_4TFSI, the volume and concentration of NBu_4TFSI is sufficent to ensure minimal Li^+ contrubution to the electorchemistry.[19]

The mechanism of non-aqueous ORR has important consequences in understanding the nature of the formed DC product (ie. formation of insoluble Li_2O_2) and its impact toward electrolyte stability and DC capacity. Pearson's "Hard-Soft Acid-Base" (HSAB) theory,[16,24] has been invoked to rationalize the ORR reduction behavior in the presence and absence of Li^+ cations. HSAB is used to explain why soluble products form with large

cations and conversely why small cations (ie. Li^+) lead to the formation of solid/insoluble Li_2O_2. From HSAB theory, depending on the qualitative size of the ion, allows the ion to be categorized as “hard or soft” (small and large, respectively) and “acid or base” (electron accepting versus donating). The O_2^- ion, being a moderately “soft base” from its large size and lower charge density can be stabilized with large sized “soft and acidic” cations such as tetrabutylammonium (often denoted as TBA^+ or NBu_4) forming stable the soluble $TBA^+\cdots O_2^-$ complex as evidenced by the highly reversible O_2/O_2^- redox couple ($O_2 + e^- \rightleftharpoons O_2^-$) (**Figure 1.5**) [28-30]. Additionally, larger alkali metal cations (K^+ and Na^+) have been shown to electrochemically form stable KO_2 and NaO_2, respectively without further disproportionation.[31,32] On the other hand, in the presence of Li^+, there is an observed positive potential shift in the onset of reduction indicating LiO_2 formation that has greater thermodynamic stability (**Figure 1.5**). Additionally, in the presence of the highly Lewis acidic Li^+, subsequent disproportionation or second 1 e^- reduction to form O_2^{2-} (peroxide), which has higher Lewis basicity is favored, causing the final and stable product as Li_2O_2.[33] Confirmation through pressure drop measurements during DC and reduction (**Figure 1.6a-c**) indicates that there does not appear to be any stable LiO_2 at during DC or at any specific potential (between 2 to 5 V vs Li/Li^+) indicative of predominantly Li_2O_2 formation (2 e^-/O_2 process). While the charge transferred at potentials >2.7 V is insignificant (**Figure 1.6b-c**), the galvanostatic result (**Figure 1.6a**) clearly follows the 2 e^-/O_2 process.

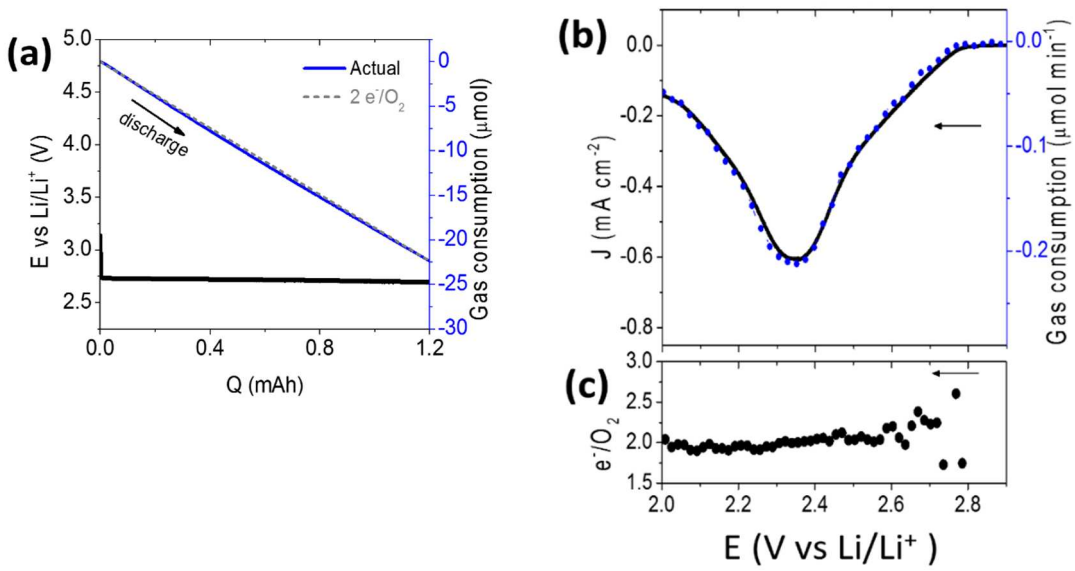

Figure 1.6 – (a) Galvanostatic DC performed with *in situ* pressure monitoring with integral O_2 consumption performed with 0.5M LiTFSI/tetraglyme, CNT positive electrode at 50 mA g^{-1} to the fixed capacity of 1.2 mAh. The dotted line indicates 2 e^-/O_2 (b) Cathodic scan with gas consumption rates performed with 0.5M $LiClO_4$/tetraglyme at 0.05 mV s-1 and (c) corresponding e^-/O_2 as a function of reduction potential. Note that in (c), the e^-/O_2 values in> 2.7 V is accompanied by insignificant amounts of charge transfer and care should be taken in its interpretation.

1.4.2 –Discharge (DC) and Li_2O_2 formation

Now that non-aqueous ORR has been elaborated upon (section 1.4.1), the mechanism of Li_2O_2 deposition can occur through different pathways. The Li_2O_2 nucleation and growth occurs through the so-called "surface" and "solvation-based" pathways (illustrated in **Figure 1.7a**), which influence the DC capacity, Li_2O_2 crystallinity and morphology. The factors which govern these two pathways are influenced by several parameters including (1) Gutmann donor number and acceptor number (DN and AN) of the electrolyte,[34,35] (2) adsorption affinity of Li_2O_2 intermediates with the electrode surface and,[36,37] (3) the reduction overpotential.[34,38]

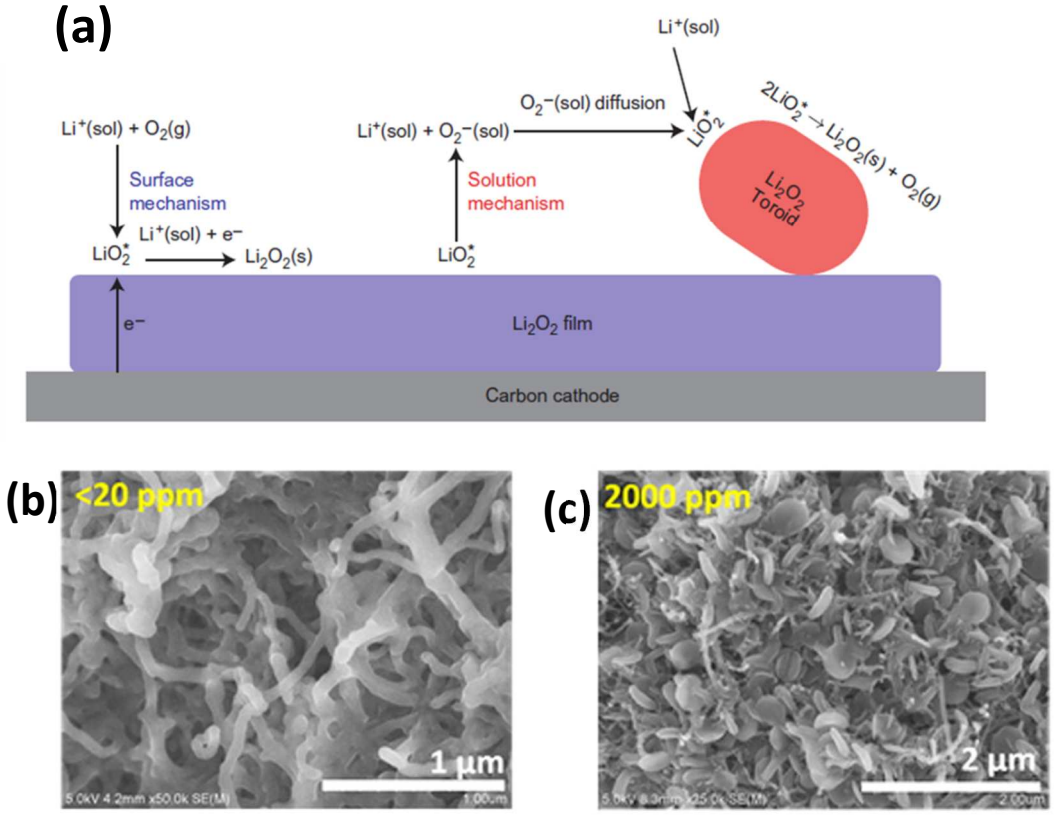

Figure 1.7 – Li_2O_2 nucleation and growth pathways. (a) Schematic showing the surface-based and solvation/solution-based mechanism for Li_2O_2 formation.[39] (b) and (c) SEM images of carbon nanotube electrode discharged with 0.5M $LiClO_4$/tetraglyme in the presence of <20 ppm and 2000 ppm of H_2O, respectively.[36] The addition of H_2O promotes the solvation-based pathway and results in toroidal Li_2O_2 crystal growth which can bypass charge transport limitations of the insulting Li_2O_2.

The DN and AN is a measure of the Lewis basicity and acidity, respectively. Following the first step of ORR ($Li^+ + O_2 + e^- \rightarrow LiO_2$*, where * denotes surface adsorbed species), LiO_2* can remain adsorbed on the electrode or become mobile in the electrolyte. The mobile LiO_2(sol) can disproportionate which can allow formation of large and aggregated Li_2O_2 crystals *via* growth from the solution-phase (**Figure 1.7c**), which forms Li_2O_2 with apparent crystalline features.[36,38] The interaction of high DN (ie. dimethyl sulfoxide (DMSO)), and AN (ie. H_2O additives) electrolytes essentially modulate the Lewis acidity and basicity of the cations (Li^+) and anions (O_2^-) allowing them to be solubilized/stabilized thus, promotes the kinetics of LiO_2 solvation and disproportionation being favored.[39,40] Conversely, low DN/AN electrolytes tend to promote the surface-based

pathway leading to the tendency of more conformal and amorphous Li_2O_2 thin-films (**Figure 1.7b**) resulting in comparatively lower capacities.[35,36,40] Aetukuri *et al*.[39] has shown that the AN of the electrolyte can be modulated with the addition of H_2O additives (ppm quantities), promoting solvation-based Li_2O_2 nucleation and growth, although this is accompanied by increased parasitic side reactions. Additionally, by modulating the Li salts with different DNs, can also modulate the level of Li^+ association with the Li salt anion and in effect can provide a means for low DN solvents to promote the formation of solvation-based Li_2O_2.[35,40]

The adsorption affinity of Li_2O_2 intermediates with the electrode surface has been shown to influence Li_2O_2 formation as demonstrated by Yang *et al*.[36] and the work in Chapter 2 of this thesis, exploring the effect of carbon surface chemistry.[37] For instance, the presence of metal or metal-oxide nanoparticles[36,41] or the introduction of surface functional groups[37,42] are methods to modulate the adsorption affinity of Li_2O_2 intermediates. After the formation of LiO_2 *via* the first Li^+/e^- in the case where the LiO_2 surface binding affinity is greater than the solvation affinity, the formation of Li_2O_2 *via* second electron transfer ($LiO_2* + Li^+ + e^- \rightarrow Li_2O_2$) is presumed to be favored. On the other hand, when the solvation affinity of LiO_2 is predominant over the surface binding affinity of the electrode surface tends to result in the bias towards solution-based Li_2O_2 nucleation and growth.

Regarding reduction overpotential, it has been shown that low reduction overpotentials can lead to the bias towards the solvation-based mechanism, while conversely, high reduction overpotentials leads to the surface-based mechanism being favored. Work from Adams et al.[38] and Gallant et al.[43] have demonstrated the effect of overpotential towards the Li_2O_2 formation pathway and have also shown that this affects the behavior of Li_2O_2 decomposition during RC (see below, section 1.4.2).

1.4.3 – Recharge (RC) and Li_2O_2 decomposition

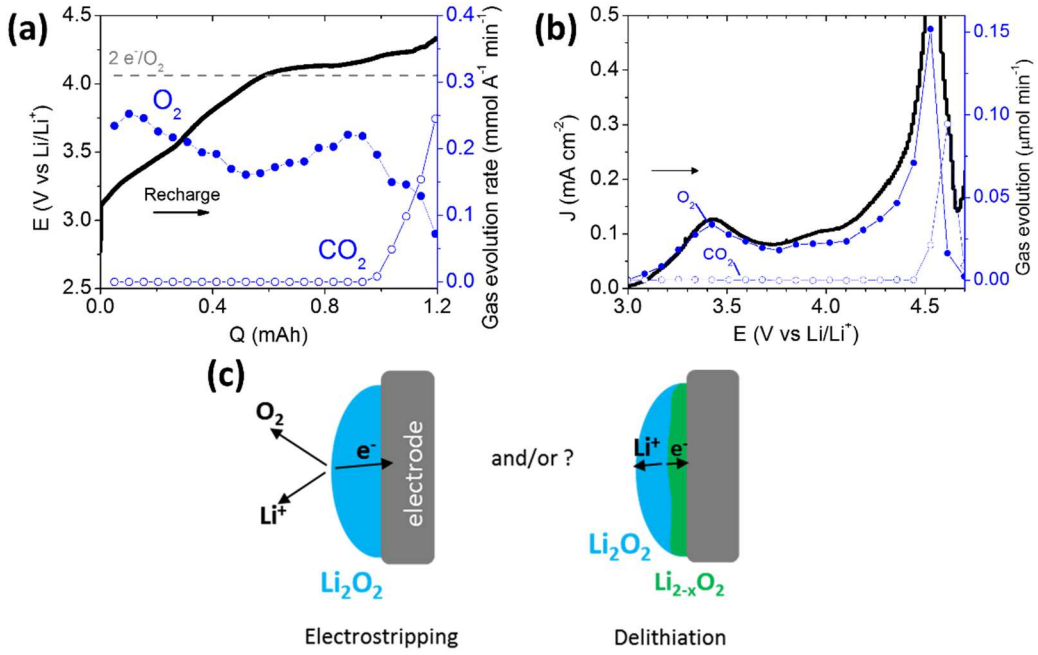

Figure 1.8. (a) Representative Li-O_2 battery galvanostatic recharge behavior with *in situ* gas analysis performed with 0.5M LiTFSI/tetraglyme containing 1.2 mg CNT electrode at current density of 50 mA g^{-1}. The dash line indicate 2 e^-/O_2 evolution rate (b) Anodic linear sweep voltammogram (LSV) with gas analysis following cathodic scan from 3 to 2 V performed with 0.5M $LiClO_4$/tetraglyme containing 1.2 mg CNT electrode at scan rate of 0.05 mV/s (c) Schematic representation of the RC process possibly involving either direct 2 e^- pathway *via* electrostripping and/or the involvement of delithiation.

Li_2O_2 decomposition occurs overall *via* $Li_2O_2 \rightarrow 2Li^+ + O_2 + 2e^-$. In comparison to the DC process exhibiting a relatively flat voltage plateau, the RC potential is different and typically increases from ~3 V at the onset of recharge to ~4.5 V at 100% Coulombic efficiency (RC to equivalent capacity) (**Figure 1.8**) [17]. The RC process is complex due to the following factors: (1) RC occurs following DC, and consequently will be influenced by the preceding DC process and the parameters affecting the DC including the Li_2O_2 formation mechanism and parasitic side reactions (2) the RC process itself is a combination of Li_2O_2 decomposition occurring concurrently with side product formation and decomposition.[44,45]

The DC parameters (discussed above in section 1.4.2) affects Li_2O_2 morphology,[43] crystallinity[46] and side reactions,[47,48] which consequently affect the RC process.

Typically, thin-film-like Li_2O_2 morphologies from the surface-based mechanism lead to lower RC overpotential in comparison to more aggregated and Li_2O_2 formed through the solution-based mechanism, which consequently require higher RC potential to decompose.[41] Our findings and those in the literature show that predominant surface-based surface-based Li_2O_2 nucleation and growth leads to the formation of amorphous Li_2O_2[37] which possesses higher electronic and ionic conductivities (5.02×10^{-9} and 7.10×10^{-8} S cm^{-1}, respectively) in comparison to crystalline Li_2O_2 (~10^{-20} S cm^{-1} for both electronic and ionic conductivities).[46,49] Therefore, promoting the formation of amorphous Li_2O_2, has potential advantages with respect to RC overpotential.[37]

Parasitic side reactions also play a significant role as shown through mass spectrometry measurements with *in situ* gas analysis (**Figure 1.8**). Clearly, contrary to the observed 2 e^-/O_2 during DC indicative of Li_2O_2 formation, the entirety of RC shows that the 2 e^-/O_2 evolution rate is not reached (meaning not exclusive Li_2O_2 oxidation) (**Figure 1.8**) which is attributed to concurrent processes of Li_2O_2 oxidation, side product formation and oxidation (see below, section 1.5). The oxidation of Li_2O_2 involving the formation of singlet O_2 (highly reactive form of oxygen) has also been proposed in the literature.[50,51] Our Li_2O_2 titration results in quantifying the amount of Li_2O_2 formed after DC indicate ~70-80% of the expected yield and our *in situ*, gas analysis of RC typically results in O_2 evolution amounting to ~60% of expected O_2,[36,37] indicating (1) Li_2O_2 deposition on inactive components of the cell (ie. separator)[38] and (2) Li_2O_2 is lost in parasitic processes during RC.[45]

There is evidence pointing to Li_2O_2 oxidation occurring through an direct $2e^-$ pathway, where *in situ* spectroscopic characterisations (surface enhanced Raman (SERS) and gas analysis) have indicated the absence LiO_2 and O_2^- during Li_2O_2 oxidation.[17,30] However, there is some discrepancy in the literature on the precise manner of how this overall $2e^-$

process occurs as to whether there is the involvement of delithation[52], direct $2e^-$ process[17] or a combination of the two (**Figure 1.8**). In an effort to rationalize the sloping and plateau regions of the Li-O_2 RC profiles, the Ceder and Shao-horn groups[52,53] proposed that delithiation of Li_2O_2 is kinetically preferred at low overpotentials (0.3-0.4 V). Their suggestion is that at low potentials delithiation occurs (ie. $Li_2O_2 \rightarrow LiO_2 + Li^+ + e^-$) followed by LiO_2 disproportionation to yield an overall 2 e^-/O_2. After this delithiation stage, the increase in potential coinciding with the direct 2e- oxidation of Li_2O_2 corresponding "bulk" Li_2O_2 is presumed to occur. We note that our recent publication (as seen in Chapter 3) has shown evidence for soluble LiO_2 at low anodic potentials by utilizing rotating ring disk electrode (RRDE).[37]

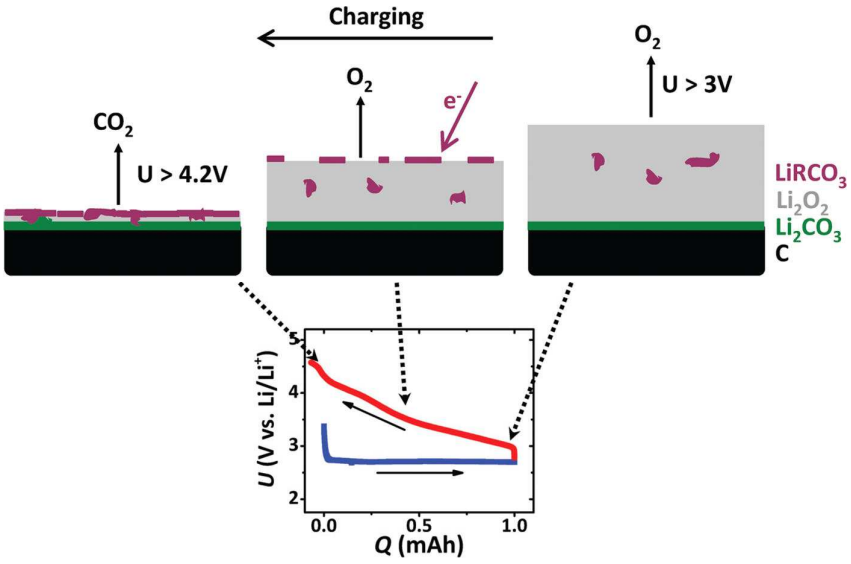

Figure 1.9 - Schematic of possible scenario during RC showing side reactions forming side products at the interfaces Li_2O_2/electrolyte and Li_2O_2/electrode interfaces where the arrow e^- indicates an unspecified/possible electrochemical process forming carbonate species.[17,47]

On the other hand, regardless of facile delithiation, side reactions also play a significant role in the rise in RC potential with McCloskey and coworkers[47] proposing that the rise in overpotential is due to accumulation of highly insulating side products at the

interfaces as illustrated in **Figure 1.9,** which inevitable leads to an increase RC overpotential.[47]

1.5 – Overview of challenges with Li-O_2 batteries

The shortcomings and challenges of Li-O_2 batteries[17,18] are highlighted and discussed below:

1. Electrolyte and electrode instability, side reactions, poor reversibility and cyclability
2. Low round-trip efficiency (Large overpotential (η >1 V), typically observed during RC)
3. Capacity limitations from charge transport restrictions in the wide bandgap Li_2O_2
4. Poor rate capability ($\leq$ 1 mA cm^{-2})
5. Contaminants from ambient air conditions (H_2O, CO_2 and N_2)
6. Typical challenges associated with metallic Li (ie. dendritic growth)

(1) *Electrolyte and electrode instability, side reactions, poor reversibility and cycleability* – The electrolyte requirements include sufficiently wide potential window (HOMO-LUMO gap), sufficient stability with reduced oxygen species, low vapor pressure, compatibility with Li metal, sufficient Li^+ conductivity and O_2 solubility.[54,55] Early work identified that carbonate-based solvents (commonly used in Li-ion batteries) are inherently decompose in the presence of superoxide (O_2^-, LiO_2), with minor amounts of Li_2O_2 actually being produced.[25,56] Reactive oxygen species (LiO_2, Li_2O_2) with solvent dependent decomposition (ie. nucleophilic substitution of carbonates and hydrogen abstraction of glymes) have been reported in literature.[56-58] Notable computational work (HOMO-LUMO gap, pK_a)[59,60] and complementary experimental methods in evaluating stability have included testing with commercially available potassium superoxide (KO_2) and characterisation with gas chromatography (GC/MS), UV-vis spectroscopy, and reversibility

of O_2/O_2^- redox couple with TBA^+ salts.[57,61,62] Accordingly, ether-based (glymes), DMSO and ionic liquids have been noted as possessing greater stability with O_2^-.[62,63] While there is the consensus of improved stability towards O_2^-, ether-based electrolytes, nevertheless ether-based electrolytes are still susceptible to decomposition via hydrogen abstraction.[48,57,64] Work examining ether-based tetraglyme from Freunberger et al, utilizing $LiPF_6$/tetraglyme showed that the after the first DC (**Figure 1.10**), x-ray diffraction identifies Li_2O_2 reflections, however, FTIR reveals side products lithium carbonate (Li_2CO_3), and lithiumer carboxylates (HCO_2Li and CH_3CO_2Li) after DC and RC. Moreover, the 5th cycle shows significant amounts of side products as detected *via* FTIR with Li_2O_2 unable to be detected with XRD. Additionally, the consensus is that there does not appear to be reports of soluble decomposition products in the electrolyte.[45,51] Along with the decomposition of the electrolyte, the use of carbon as the positive electrode has also been shown to decompose as shown by *in situ* gas analysis studies utilizing isotope labelled ^{13}C electrodes.[47] In terms of cell failure, the consensus is that electrolyte instability and the inability to decompose side

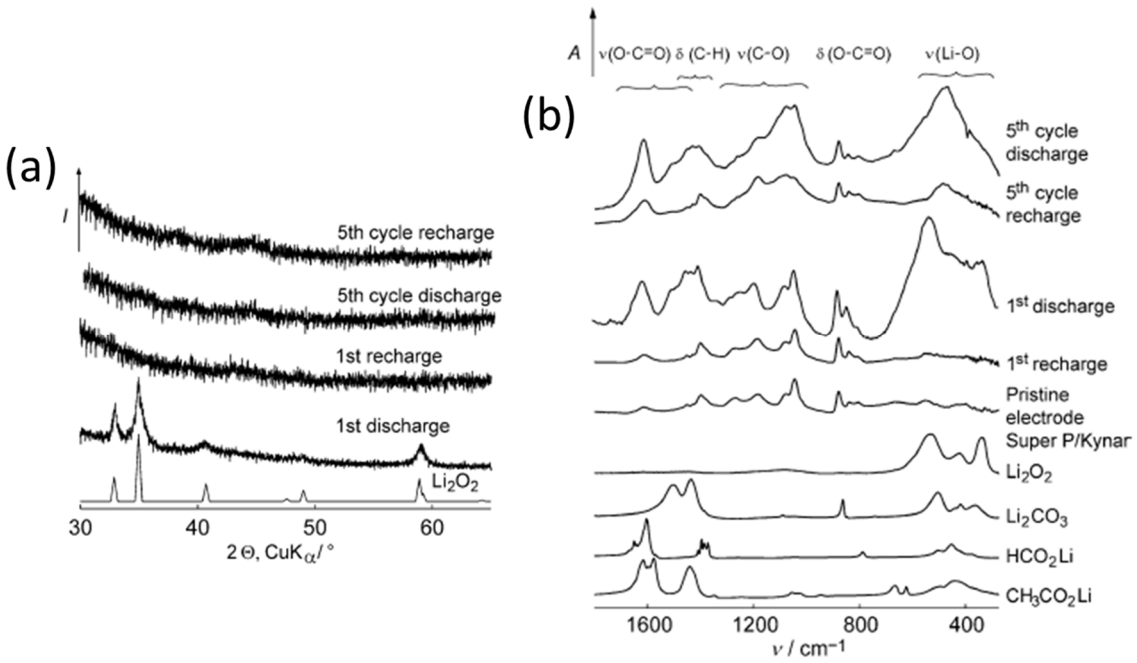

Figure 1.10 – X-ray diffraction and chemical analysis of discharged and recharged electrodes (a) XRD and (b) Fourier transform infrared (FTIR) analysis. The cells utilized 1M $LiPF_6$ in tetraglyme at the current rate 70 mA/g.[63]

products leads to the build-up of insulating side products on the electrode surfaces which induces the poor cycleability typically observed in Li-O_2 cells.[65] In closing, methods to suppress and mitigate side reactions including the development of more stable electrolytes is necessary to move the Li-O_2 battery field forward.[45,57,66]

(2) *Low round-trip efficiency* – While relatively low overpotentials are observed during DC (η <400 mV), RC is plagued with overpotentials in excess of 1 V. The reasons has been attributed the sluggish kinetics in the oxidation of the wide bandgap Li_2O_2[17], and the formation of highly insulating side products at the electrolyte/Li_2O_2 and electrode/Li_2O_2 interfaces which require high potential to decompose.[47] Attempting to mitigate this issue, many researchers have utilized nanostructured metal and metal oxides largely due to their use in aqueous oxygen evolution electrocatalysis.[17,26] However, the role of electrocatalysis in Li-O_2 batteries is controversial due to the lack of turnover of any potential active sites which precludes 'true' electrocatalysis.[26,67] Moreover, the influence towards the promotion of Li_2O_2 oxidation versus side reactions remains largely speculative (topic of Chapter 4) due to the lack of quantitative analysis in measuring reversibility utilized in the vast majority of existing reports (ie. *in situ* gas analysis, Li_2O_2 quantification). More generally, "structurally tuning Li_2O_2" by promotion of the surface-adsorption based Li_2O_2 formation pathway leading to amorphous and conformal Li_2O_2 thin films is one approach in supressing RC overpotential, albeit at the trade-off of DC capacity (discussed in Chapter 3).[37] Another approach has been the utilization of low concentrations (~10mM) of soluble redox mediators (ie. LiI, TEMPO),[68] where the redox mediator is electrochemically oxidized, which in turn through the solution phase can chemically oxidize Li_2O_2 (reducing the redox mediator back to original state) resulting in reduced RC overpotential (although their efficacy has been questioned).[69] It should be noted that due to ongoing materials challenges, the elimination of side reactions has been a challenging endeavour[51] although the recent development of

molten inorganic nitrate salts has shown some promise,[66] resulting in flat RC plateau at significantly reduced overpotential.

(3) *Lower-than-theoretical discharge capacity* – Theoretical studies have identified that in Li_2O_2 films, that charge transport (*via* electron tunneling and hole polaron hopping) can only support the maximum thickness of 5-10 nm,[70,71] which has consequences with respect to the overall DC capacity since the DC capacity will limited the volume occupied in porous electrodes. Methods to circumvent this limitation have been identified by solubilizing the LiO_2 intermediate and forming Li_2O_2 the solvation-based pathway.[34,48] Of course, the trade-off of the Li_2O_2 solvation-based pathway will result in consequences with respect to difficulty in decomposing the aggregated and crystalline Li_2O_2 during RC.[36]

(4) *Poor rate capability* – Laboratory Li-O_2 cells are often tested with low current densities in the order of $\leq$1 mA cm^{-2} and typically, the 1C rate (C-rate is the current rate where DC completes in 1 hour) is not tested or reached.[12] In a practical sense, rate capability is important in the ability to deliver sudden power when needed (ie. power tool and EV applications) and perhaps more importantly to provide reasonable RC times. The origin can be related to the poor kinetics of Li_2O_2 oxidation related to its intrinsically low ionic and electronic conductivities, and morphology.[24,38] Attempts to mitigate this issue have involved the use of soluble redox mediators which can be facilely electrochemically oxidized and in turn, chemically oxidize Li_2O_2.[72]

(5) *Contaminants from ambient air* - For practical Li-O_2 batteries, if unpurified air is utilized, there is the issue with contaminants and impurities from H_2O, CO_2 and N_2. Work from Aetukuri *et al*,[39] and Gasteiger and coworkers[73] with H_2O additives identified that the Li_2O_2 nucleation and growth process can be altered, where the addition of ppm quantities of H_2O to low DN solvents can result in the promotion of solvation-mediated Li_2O_2 growth.

Extensive H_2O contamination can also lead to the transformation of Li_2O_2 into LiOH ($Li_2O_2 + H_2O \rightarrow LiOH + H_2O_2$) and the H_2O interaction with metallic Li ($2Li + 2H_2O \rightarrow 2LiOH + H_2$). The presence of CO_2 have been shown to lead to chemically react with Li_2O_2 to form Li_2CO_3 which requires high potential to decompose.[74] The interaction of N_2 with metallic Li leads to the formation of highly insulating lithium nitride ($6Li + N_2 \rightarrow 2Li_3N$), although this can be mitigated by an isolated and protected Li electrode. In all, reversibility is compromised when H_2O or CO_2 is present in the gas supply of Li-O_2 batteries.[35,74] For practical Li-O_2 batteries, a pressurized tank containing purified O_2 or the utilization of O_2 selective membranes can be employed to mitigate the effects of atmospheric air [12], electrolyte engineering with hydrophobicity[75] have been possible avenues to approach this challenges.

(6) *Issues with metallic Li* – To maximize the specific energy and volumetric energy density of the cell, it is ideal to utilize Li metal as the negative electrode.[24] The low reduction potential of Li metal, causes issues with Li plating and stable SEI (solid-electrolyte interface) formation. Moreover, Li metal is accompanied by additional issues with Li dendrite growth leading to the unintended short circuit of the battery and safety concerns.[76] A permanent and practical solution has yet to be commercialized for lithium-based batteries let alone, Li-O_2 batteries.[17] Potential solutions have included the use of cation additives (ie. Cs^+, Rb^+) with lower reduction potentials than Li^+ or the use solid state electrolytes/artificial SEI with sufficient mechanical strength.[17,77]

1.5 – Thesis objectives

The overall message in Chapter 1 is that research in Li-O_2 batteries is still very much in its infancy with many challenges that remain to be tackled. Of critical importance before practical non-aqueous Li-O_2 batteries can be realized, the thorough understanding of the

underlying DC and RC processes in Li-O_2 cell is a prerequisite. The present thesis attempts to address this in the following ways:

In Chapter 2, the experimental methods central to this thesis is discussed including the electrochemical cells, testing conditions, and post-mortem characterisations. Our analyses methodology essentially consists of three aspects where standard electrochemical testing is complemented with morphological, chemical, and quantitative analysis. Our approach of correlating these three characterisation avenues allows for greater understanding by providing a more complete picture of the processes occurring in our Li-O_2 cells. We emphasize the quantitative *in situ* on-line electrochemical mass spectrometry (OEMS) technique to evaluate gas-phase chemistry, which was constructed and utilized within the laboratory.

In Chapter 3, we elucidate the often overlooked importance of the surface characteristics of carbon electrodes. Carbon is a highly attractive and practical material due to its advantageous properties including high surface area, porosity, conductivity, low cost, natural abundance, low toxicity, and sufficient activity for oxygen reduction in Li-O_2 cells. It is of our opinion that if Li-O_2 batteries are to be widely adopted, carbon will most likely be a necessary component for the positive electrode. Through our systematic methodology of decoupling oxygen functional groups, defective edges, and graphitization in carbon nanotubes, we demonstrate the ability to tune the Li_2O_2 structure (morphology and crystallinity) by controlling the surface properties of multi-walled carbon nanotubes. The findings have important implications of carbonaceous electrode surfaces toward DC capacity, RC overpotential, and reversibility. We show that controlling the Li_2O_2 structure with respect to the thin-film and amorphous Li_2O_2 is one possible approach in mitigating the large RC overpotential.

In Chapter 4, we address the use of the so called “solid catalysts” composed of metal and metal oxides often used to “mitigate” the large RC overpotential. However, the majority of the studies in literature are not comprehensive in correlating chemical analysis with quantitative measure of reversibility, meaning it is often unclear whether nanostructured metal and metal oxides promote reversible Li-O_2 electrochemistry or promote parasitic side reactions. Our study addresses this by combining chemical analysis with the utilization of *in situ* on-line electrochemical mass spectrometry (OEMS) studies to better understand the effects of metal and metal oxide nanoparticles (NPs) toward Li_2O_2 oxidation, electrolyte oxidation, NP size, reversibility and lastly, cycleability. The implications of our findings in clarifying the efficacy of “solid catalysts” can identify if further development into nanostructured metal/metal oxides is warranted or if research efforts are better directed elsewhere.

Lastly, in Chapter 5, we take our findings and discuss the lessons learned from these studies, and potential avenues of future research. This includes recent developments in the field which have come after the completion of the experimental work performed in this thesis.

Chapter 2

Experimental methods

Chapter 2 elaborates on the major methods used throughout this thesis. This consists cell assembly, and the characterisation methods used in Li-O_2 battery research. Our analysis methodology (**Figure 2.1**) essentially consists of three aspects where conventional electrochemical testing is complemented with morphological, chemical, and quantitative analysis. Our approach of correlating these three characterisation avenues allows for greater understanding by providing a more complete picture of the processes occurring in our Li-O_2 cells. We emphasize the quantitative *in situ* on-line electrochemical mass spectrometry (OEMS) technique to evaluate gas-phase chemistry, which was constructed and utilized during my doctoral studies.

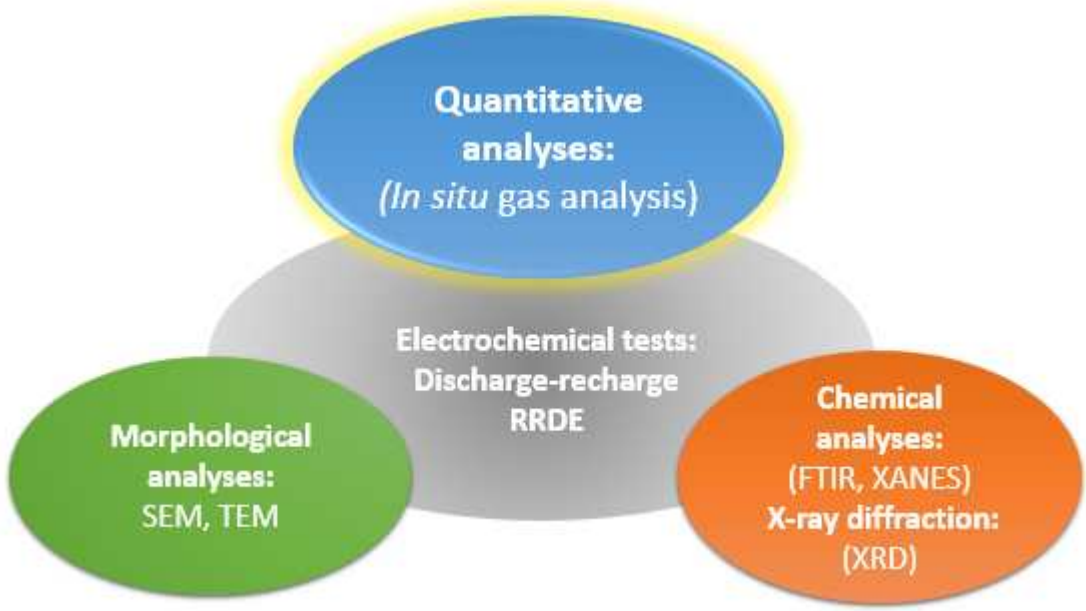

Figure 2.1 – Diagram showing the overview of our characterisation methodology in studying Li-O_2 batteries. Standard electrochemical techniques of galvanostatic discharge-recharge (DC-RC) and rotating ring disk electrode (RRDE) is complemented with different techniques separated into morphological, chemical and quantitative analyses.

2.1 - Metal-oxygen cell components and assembly

2.1.1 - Metal-oxygen cell

The metal-oxygen cell used (**Figure 2.2**) was designed and manufactured by contributions from past Byon IRU members in conjunction with Tomcell®, Japan [1,2]. These are two electrode cells utilizing Li metal as the negative and typically, binder-free carbon nanotube electrode as the positive. Although possible O_2 contact with Li metal occurs in most cell configurations found in literature, it has not been found to affect the

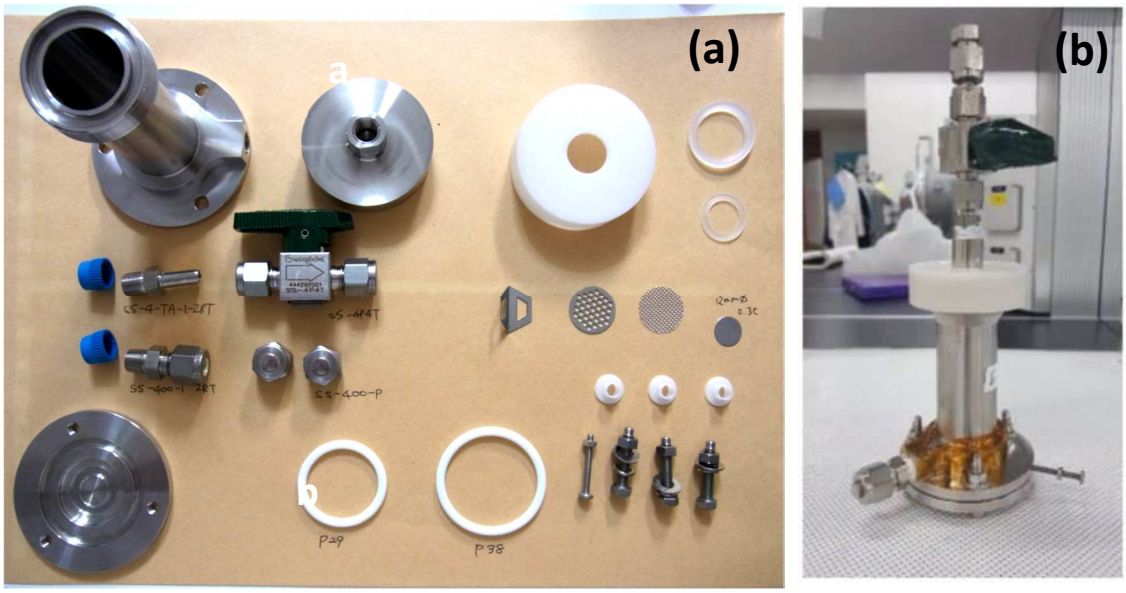

Figure 2.2 – Metal-O_2 cell (a) Top view of standard metal-oxygen cell that is completely disassembled with cell components (b) The metal cell in the fully assembled form.

electrochemistry.[3] The internal volume of the cell is approximately 40 mL which allows for sufficient oxygen to avoid O_2 starvation from extremely high depth of DC or from prolonged cycling. The cell body is composed of stainless steel with stainless steel Swagelok fittings and values to ensure complete sealing without leakage. The individual cell components are made of stainless steel or polypropylene to ensure chemical inertness with the electrolyte and operating environment of the cell. All cell components were thoroughly dried 80°C in vacuum overnight prior to cell assembly to thoroughly remove all residual water. Periodic

leak checking was conducted as a preventative measure due to the high sensitivity of the Li-O_2 battery chemistry with contaminants such as H_2O, CO_2 and N_2.

2.1.2 - Electrolyte

The electrolyte used throughout this work contains tetraethylene glycol dimethyl ether (battery grade, UBE Industries), commonly referred to as tetraglyme (**Figure 2.3**) as the solvent. Tetraglyme has reasonable stability towards superoxide[4,5] in comparison to other aprotic solvents including dimethyl sulfoxide (DMSO)[6] and alkyl/cyclic carbonates.[7]

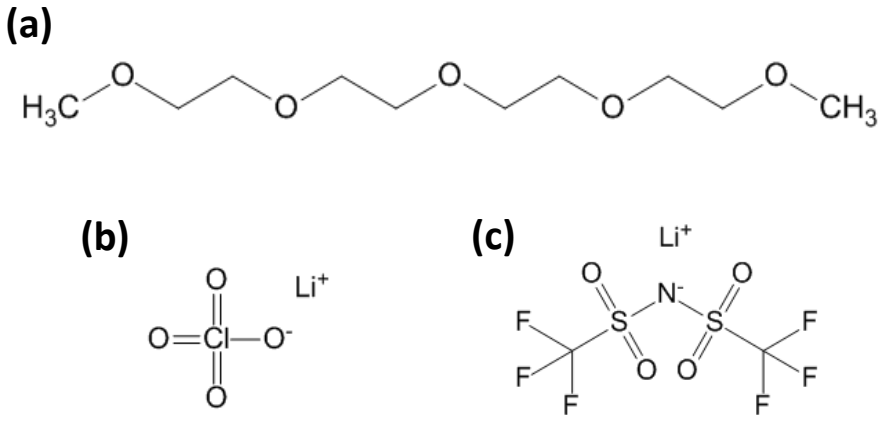

Figure 2.3 – Structural representations of solvent and Li salts used throughout this work (a) tetraethylene glycol dimethyl ether (denoted as tetraglyme) (b) lithium perchlorate ($LiClO_4$) (c) Bis(trifluoromethane)sulfonimide lithium ($LiN(SO_2CF_3)_2$) (denoted as LiTFSI)

Other versatile properties of tetraglyme includes its low vapor pressure which is ideal for gas analysis and prolonged cycling, and lastly compatibility with Li metal.[8] Before use, the tetragylme solvent was dried with molecular sieves (Nacalai, 4Å) prior to use. Once the Li salt dissolved, the typical water content was <20 ppm as measured by Karl-Fischer titration. Tetraglyme is a low polar solvent (ε=7.79) processing moderate Gutmann donor number (16.6 kcal mol^{-1}).[9] The Li salt employed in the work of this thesis was either 0.5M lithium perchlorate ($LiClO_4$) or lithium bis(trifluoromethane)sulfonimide (LiTFSI), which have moderate to low donor numbers at 8.44 and 5.4 kcal mol^{-1}, respectively (Figure 2.1).[10,11]

2.1.3 - Electrode materials

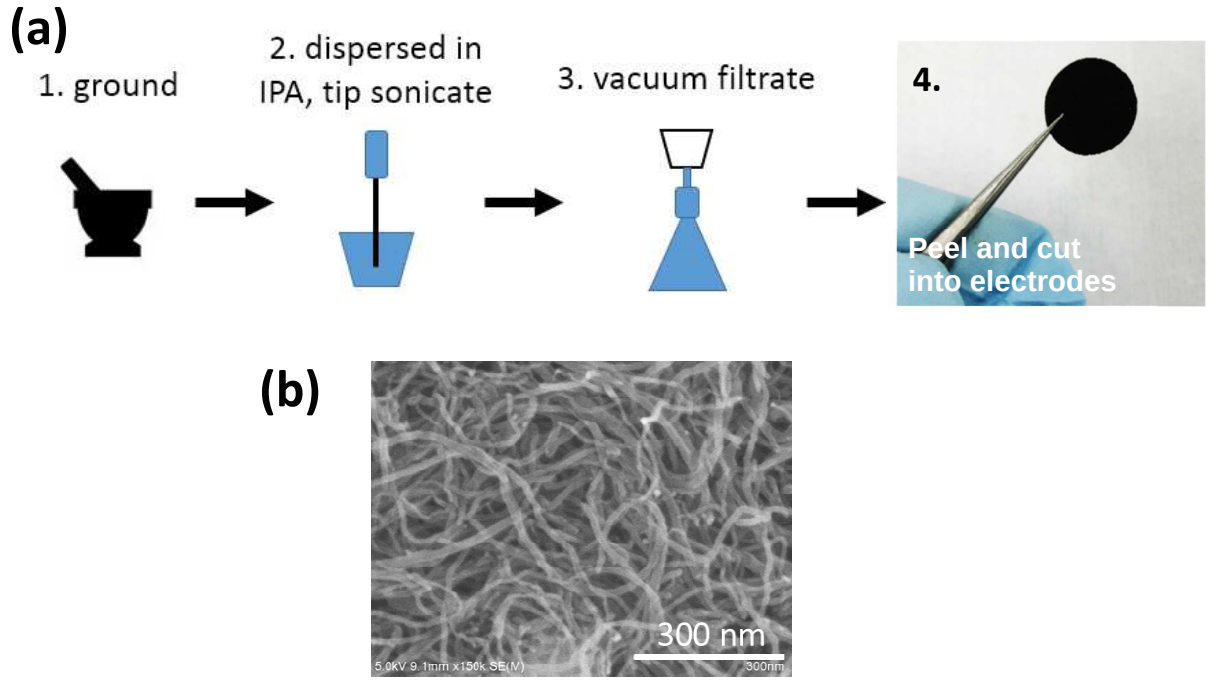

Figure 2.4 – (a) Schematic showing the main procedures for fabricated binder-free carbon nanotube films for use as the positive electrode in Li-O_2 cells. On the right most image (labelled as 4) is a digital photograph of a typical as-prepared binder-free carbon nanotube electrode. The electrode diameter is 12 mm. **(b)** SEM image of typical as-prepared carbon nanotube electrode

Byon IRU has put extensive emphasis on carbon-based electrodes and specifically, multi-walled carbon nanotubes.[12] There are several attractive aspects in utilizing binder-free carbon nanotube electrodes including: (1) typical binders conventionally employed including polyvinylidene fluoride (PVDF) have been shown to decompose during cell operation,[5,13] (2) the well-defined nanotube structure with high aspect ratio allows for detailed microscopy studies,[14] (3) the nanotube walls and surfaces can be facilely modified with the inner walls remaining intact allowing for conductivity to remain,[12] and (4) the mass of the electrodes could be easily controlled with high uniformity by adjusting the mass of carbon nanotubes from preparation.[12] Binder-free carbon nanotube films are fabricated by dispersing carbon nanotubes in isopropanol solvent and tip sonication followed by a simple vacuum filtration process through glass fibre (GF/C) (**Figure 2.4**). [2,12] After drying, individual electrode disks of 12 mm could be cut. The work presented here contained a

typical electrode mass of either ~1.2 mg or ~2.0 mg. By simply modulating the amount of carbon nanotubes in the isopropanol mixture, the mass of the electrodes can be easily adjusted.

2.1.4 - Cell assembly

The cell assembly was performed inside an Ar-filled glovebox (Kiyon, Korea) with <1 ppm of H_2O utilizing high purity Ar (99.995%, Tomoe Shokai). The cell components were fried in vacuum at 80ºC overnight before being transferred while still hot into the glovebox. Cell assembly commenced once the cell and components have cooled to ambient glovebox conditions. The order of the cell components and schematic of the cell assembly is illustrated in **Figure 2.5**. The cell consists of a negative electrode composed of Li metal film (Honjo) on a ϕ 12 mm stainless steel plate. A total of 150 μL of electrolyte was inserted via pipette in between the Li metal and Celgard separator, in between the glass fibre separator and positive electrode and finally one more drop on top of the electrode. The separators consists of Celgard 2500 and glass fibre GF/C (Whatman). On top of the electrode is stainless steel mesh followed by the stainless steel current collector. Ensuring a good connection with the top of the cell is the V-shaped spring. The purpose of the stainless steel mesh on top of the positive electrode is to prevent the electrode from adhering to the stainless steel current collector and allow for post-mortem analysis. After cell assembly the cells were rested in Ar for at least 2 h prior to being purged and filled with O_2 (99.99995%, Tomoe Shokai) at 100 sccm before sealing at a pressure of 1.5 atm (measured by pressure transducer). Before cell testing, the cell was rested in the O_2 filled state for 3 h under open circuit potential (OCP) conditions.

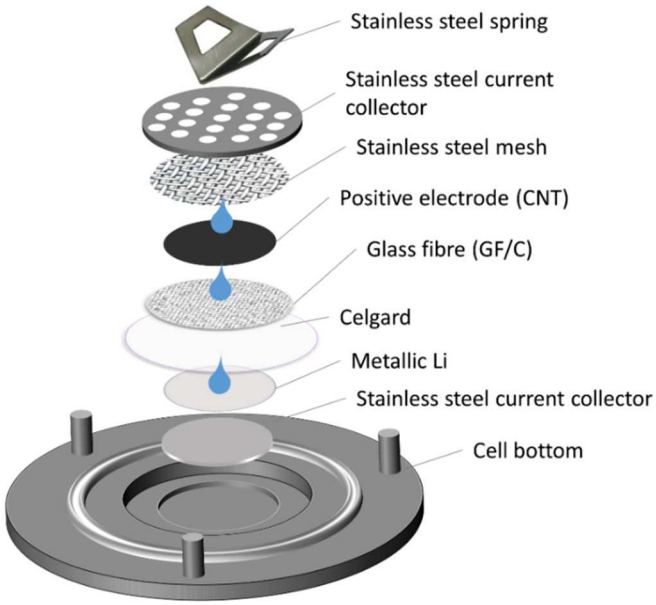

Figure 2.5 - Schematic of cell components and the order in which they are assembled in the Li-O_2 battery cell. The electrolyte is added 50 µL at a time giving a total of 150 µL of electrolyte

2.2 Characterisation methods

2.2.1 – Electrochemical characterisations

Electrochemical testing for the standard 2-electrode cells was conducted with the use of WBCS3000, WPG100e (WonATech), or VMP3 (Biologic) potentiostat/galvanostats with the individual cells inside constant temperature chambers (Yamato) set at 25ºC. Typical battery tests involves DC under galvanostatic (constant current) conditions to either a predetermined fixed capacity or to a cutoff voltage (≥2 V) followed by RC to the equivalent capacity (means 100% coulombic efficiency). The cells were typically rested 3 h under the open circuit potential (OCP) condition prior to electrochemical testing. The current densities are with respect to the mass of carbon nanotube (CNT) present in the electrode.

The bulk 3-electrode measurements were performed inside an Ar-filled glovebox utilizing a CH704E (ALS) potentiostat with Li metal used as both the counter and reference electrodes. For the voltammetry experiments, the potential is swept linearly with time with

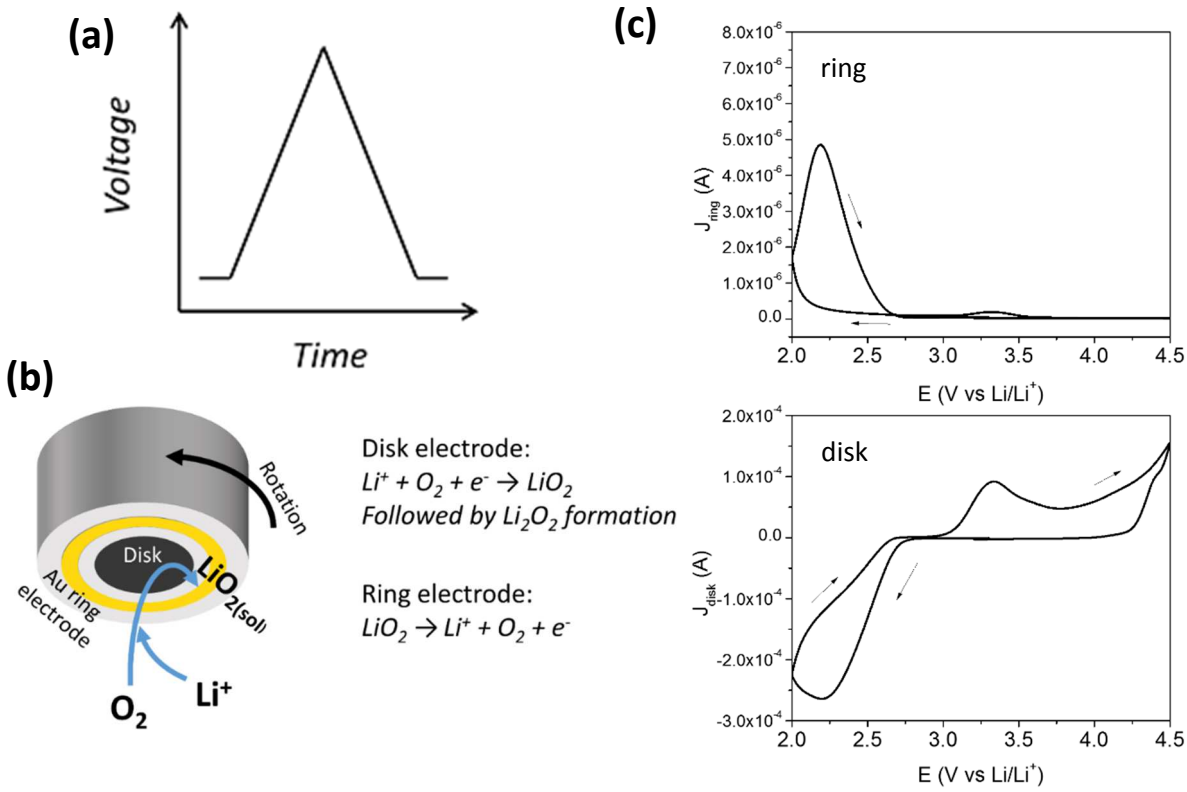

Figure 2.6 – (a) In voltammetry measurements, the voltage is scanned linearly with time with the current response recorded (b) Schematic of rotating ring disk electrode during reduction and the reactions occurring at the disk and ring respectively. The ring electrode would be held at >3 V to allow for oxidation of the LiO_2 intermediate for detected. (c) Corresponding representative Li-O_2 electrochemistry of the (top) ring response (bottom) disk response performed at 2 mV/s with 0.5M $LiClO_4$/tetraglyme scanned from potential range 2 to 4.5 V.

the current monitored (**Figure 2.6a**). The utilization of the rotating ring disk electrode (RRDE) electrode allows for the detection of soluble reaction intermediates, which are formed at the disk electrode and due to the laminar flow caused by the rotation, the intermediates reach the ring electrode (set at a fixed potential) allowing for detection as illustrated in **Figure 2.6b**. In the case of the Li-O_2 battery electrochemistry, RRDE allows the detection of the soluble LiO_2 intermediate [14-16] which first gets produced at the disk electrode and can wither proceed to Li_2O_2 formation (disproportion or electrochemical

pathway) on the disk or be transported through forced convection,to the ring where it is re-oxidized ($LiO_2(sol) \rightarrow Li^+ + O_2 + e^-$) (**Figure 2.6**).

2.2.2 – XANES (X-ray absorption near edge structure)

XANES measurements were carried out by our collaborators at the Synchrotron Radiation (SR) Center in Ritsumeikan University. Beamline-13 (BL-13) was utilized for soft x-ray absorption spectroscopy the energy range of 1000 to 5000 eV. Within Byon IRU, the primary purpose is to utilize XANES to clearly identify the presence of Li_2O_2 and side products in our DC and RC electrodes. XANES offers high sensitivity especially when analyzing electrodes of varying depths of DC and RC, where there can be relatively low concentrations of products present in the sample. Furthermore, XANES offers different detection modes allowing the discrimination between surface-sensitive and bulk-sensitive information of the sample. After electrochemical testing, the electrodes were extracted from the cells and washed with acetonitrile before being dried under vacuum at 60°C. The electrode samples were loaded into a transfer vessel inside the Ar-filled glovebox before being sent to the SR Center.

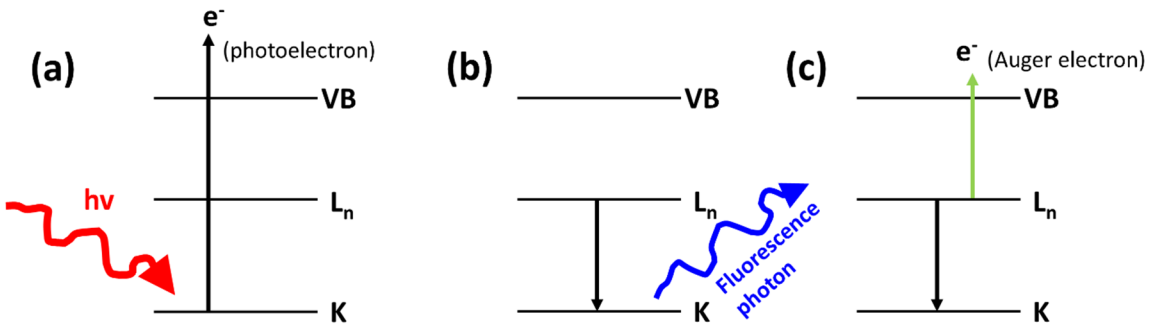

Figure 2.7 – Processes associated with XANES (X-ray absorption near edge structure) (a) X-ray radiation accompanied by photoemission and hole formation, followed by (b) Filling of hole by higher energy level electron accompanied by fluorescence emission or (c) Auger electron emission. K corresponds to the K-edge or core level orbital, and L_n denotes higher order orbitals.

Based on the photoelectron effect, monochromated x-rays targeted at the sample results in the formation of a photoelectron and hole (**Figure 2.7a**), where in XANES, the

photoelectron is ejected from the core level and is promoted into a higher unoccupied state above the Fermi level or vacuum level. XANES works on the principle of detecting the subsequent decay processes (**Figure 2.7b-c**). The filling of the core level hole by an electron of a higher level can result in an emission of another electron or Auger electron (**Figure 2.7c**). Another possibility results in the filling of the core level hole from an electron of a higher which is accompanied by florescence and release of photons (**Figure 2.7b**). The tendency of the two processes depends on the z number of the sample analyzed. By detecting and collecting all electrons emitted is referred to as total electron yield (TEY), while discriminating between photoelectrons from Auger electrons gives the partial electron yield (PEY), both of which is surface sensitive. On the other hand, florescence emission in which the partial florescence yield (PFY) is detected is bulk sensitive as photoemission is not required for the detection of florescence.

2.2.3 – XPS (X-ray photoelectron spectroscopy)

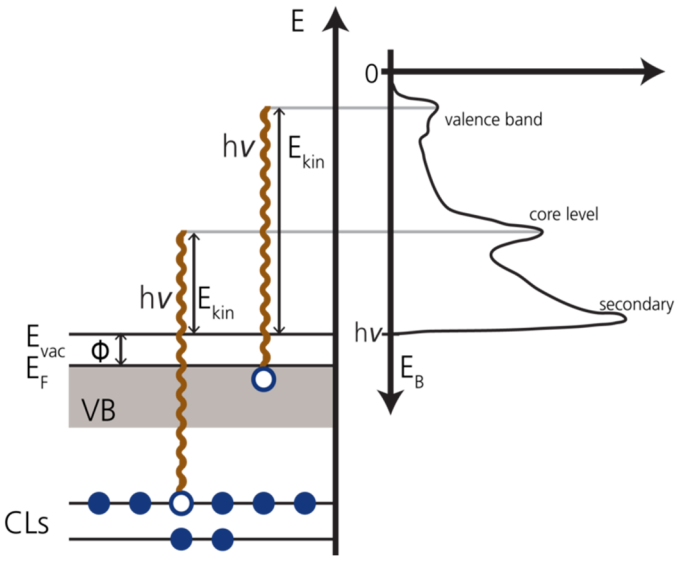

Figure 2.8 – Schematic showing the relationships between the core level (CL) photoemitted electrons, kinetic energy (K_{kin}), binding energy (E_B) x-ray energy (hv) and work function (Φ).[17]

X-ray photoelectron spectroscopy (XPS) is a surface sensitive technique, giving information of composition, chemical shifts and oxidation state of the sample. XPS involves targeting the sample with monochromated X-rays where via the photoelectron effect results

in photoemitted electrons (leaving behind holes) from the core level (CL) at a given kinetic energy. The relationship between the kinetic energy (K_{kin}) of the photoemittted electrons and the energy of the x-ray ($h\nu$) is given by $K_{kin} = h\nu - E_b - \Phi$ which are illustrated in **Figure 2.8**, where *Eb* is the binding energy and Φ is the work function. By deciphering the kinetic energy of the ejected electrons essentially allows one to characterise the electronic structure of the sample.

2.2.3 – XRD (X-ray powder diffraction)

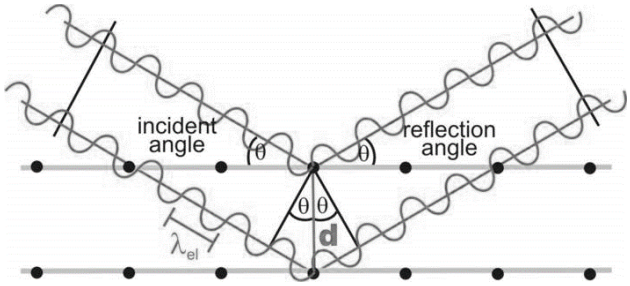

$$n\lambda = 2d \sin(\theta)$$

Figure 2.9 – Schematic of Bragg's Law

X-ray powder diffraction (XRD) utilized in this thesis are done with a Rigaku Smartlab apparatus utilizing Cu Kα with λ≈1.542 Å. For the DC or RC electrodes, the XRD samples were prepared inside the Ar filed glovebox by putting the electrode onto a glass holder and subsequently sealing with Mictron^{tm} (Toray) film preventing exposure to air. Characterization of the relative crystallinity of the Li_2O_2 DC product regarding the degree of Li_2O_2 amorphousness deposits together with crystalline Li_2O_2. Crystalline materials have periodic order within their atomic structure which can be probed with XRD. With Bragg's law (**Figure 2.9**), as theta is varied, the periodicity of the atomic structure can be probed as constructive interference resulting in detected diffraction. Consequently, resulting theta dependant reflections can be used to identify compounds. Moreover, the crystallite size is proportional to the full width at half maximum (FWHM) where FWHM increases as crystallite size decreases. It should be noted that in the Li-O_2 field, XRD is typically

supplemented with chemical analysis as side products of Li_2CO_3 and Li carboxylates are typically not detectable with XRD.

2.2.4 – FTIR (Fourier transform infrared spectroscopy)

FTIR is a form of vibrational spectroscopy whereby infrared radiation is targeted at the sample causing molecules with a dipole change to vibrate. As a result a portion of the IR radiation is absorbed and also transmitted through the sample. The resulting signal is a wave as function of time which is converted into the frequency domain via Fournier transform and serves as the molecular fingerprint of the molecule. The device used for FTIR in this thesis is a Theromofischer Scientific Nicolet iS50 with wave number range of 500 to 4000 cm^{-1}. For Li-O_2 related research, FTIR is a versatile technique to chemically identify the principle discharge product Li_2O_2 and also the presence of side products of Li_2CO_3, CH_3CO_2Li and HCO_2Li.

2.2.5 – UV-vis based peroxide titration

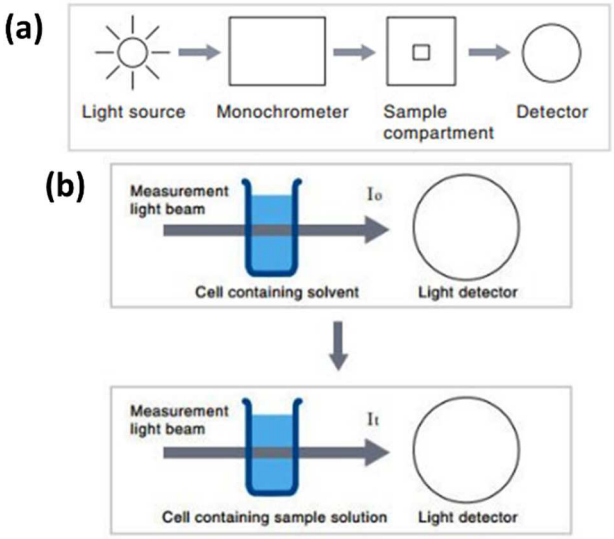

Figure 2.10 – Schematics for principles of UV-visible spectroscopy (a) block diagram of system components (b) diagram for liquid based samples which involves measuring the I_o (intensity) of the solvent first followed by the I_t of the sample and solvent.[18]

UV-vis spectrometry operates by directing a light source through a monochromator (to separate into different wavelengths) through the target sample and reference and finally reaches a detector (**Figure 2.10**). The ratio in intensity is determined by the intensity of light passing through the sample and reference given by the relation, $T = \frac{I_t}{I_o}$ with T referred to as transmittance. Typically in solution samples, the reference being the solvent itself is first measured to give I_o followed by the sample and solvent together giving I_t. To convert to absorbance the relation, Absorbance = $\log_{10}\left(\frac{1}{T}\right)$ is used.

In our case, to quantify the amount of Li_2O_2 in the discharged electrodes a UV-based peroxide titration was performed based on previous reports by utilizing $Ti(IV)OSO_4$.[19,20] In the presence of water, alkaline (MeO_2) peroxides react as shown below, where $H_2Ti(VI)O_2$ absorbs strongly at 408 nm.[20] On this basis, this method can be extended to Li-O_2, Na-O_2 and other alkali metal-O_2 batteries.

$Me_2O_2 + H_2O \rightarrow 2MeOH + H_2O_2$

$2MeO_2 + 2H_2O \rightarrow 2MeOH + H_2O_2 + O_2$

In the presence of $Ti(IV)OSO_4$:

$Ti(IV)OSO_4 + H_2O_2 + 2H_2O \rightarrow 4H^+ + H_2Ti(VI)O_4 + OSO_4^{4-}$

The UV-vis spectra obtained during calibration and the typical calibration curve utilizing commercial Li_2O_2 (>99%, Kojundo Chemical Lab. Co.) is shown in **Figure 2.11**. Typically following DC, the cells were purged with Ar and transferred into the glovebox for disassembly within 30 minutes of the cell test finishing. Inside the glovebox the extracted electrode and glassfiber separator were submerged in 10 mL of $Ti(IV)OSO_4$ solution (1.9-2.1% for the determination of H_2O_2, Sigma Aldrich) with the vial shaken for ~1 min. The UV-vis measurements were subsequently done within 30 minutes of soaking.

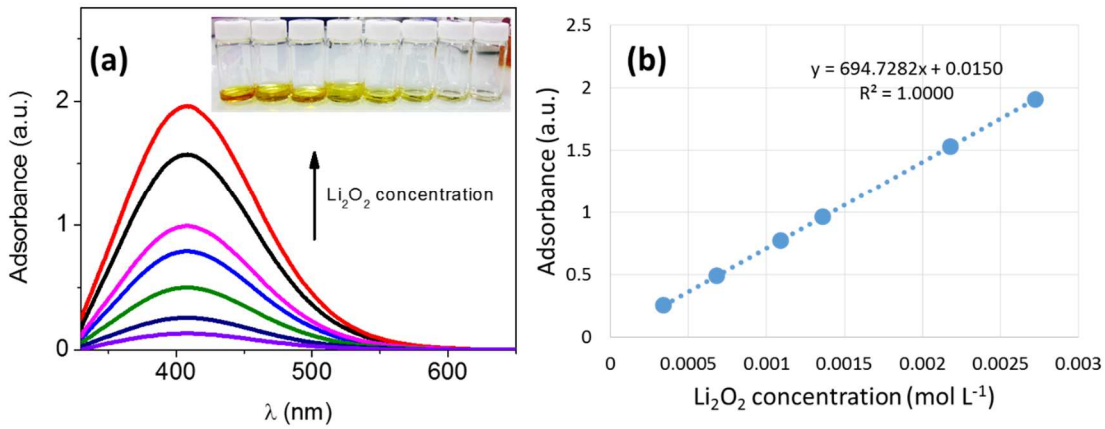

Figure 2.11 – Peroxide titration used to quantify Li_2O_2 yield (a) UV-vis absorbance as a function of wavelength with increasing Li_2O_2 concentration (inset) digital photograph of the $TiOSO_4$ and various Li_2O_2 concentrations in vials used for calibration (b) calibration curve with Lambert-Beer type relationship giving Li_2O_2 concentration versus absorbance, where the absorbance is the value at λ=408 nm.

2.3 - *In situ* electrochemical mass spectrometry

In situ electrochemical mass spectrometry, in general, is a versatile technique that can be applied to many different applied to different electrochemical systems involving gas phase electrochemistry[21,22]. Many different techniques that can be exploited including (1) quantitative nature of gas phase reactants and products allowing the clarification of reaction mechanisms and (2) the ability to detect isotopes, which can be further exploited in detailed mechanistic studies [23].

In situ electrochemical mass spectrometry within the Li-O_2 battery field has been extensively utilized and emphasized by McCloskey and coworkers at IBM Research with an apparatus that they referred to as *in situ* differential electrochemical mass spectrometry (DEMS) [24-27]. Other prominent groups including the Gasteiger,[28,29] Nazar groups,[30,31] and also Liox Power Inc.,[7] have utilized *in situ* electrochemical mass spectrometry measurements to complement their Li-O_2 research. A significant majority of reports have relied primarily on *ex situ* spectroscopic techniques where parasitic side products would be detected [27]. That is, O_2 consumption and subsequent O_2 evolution were not

quantified meaning that reversibility could not be sufficiently evaluated [25]. *In situ* electrochemical mass spectrometry technique introduced the new perspective of quantitative measures of reversibility and making this one of the most useful analytical techniques in the field [27]. Figures of merit and benchmarks include (1) number of electrons per O_2 molecule (e^-/O_2) and (2) ratio of O_2 evolved to O_2 consumed (O_2 evolved/consumed or OER/ORR).[24] In the ideal Li-O_2 electrochemistry the discharge and recharge would equate to 2 e^-/O_2 processes indicating exclusive Li_2O_2 formation and decomposition. Additionally, the ratio of the overall O_2 consumption and O_2 evolution during DC and RC (OER/ORR ratio), respectively, should equal to 1 for the ideal Li-O_2 electrochemistry.

Herein, an overview of the constructed on-line electrochemical mass spectrometry (OEMS) system at Byon IRU is discussed. In this thesis, we primarily utilize *in situ* mass spectrometry to characterize reversibility and to observe the gas evolution trends of different electrode materials. Additional discussions regarding the construction and testing processes along are located in **Appendix A** of this thesis.

The work within the group that have utilized the OEMS technique include:

1. Wong, R. A.; Dutta, A.; Yang, C.; Yamanaka, K.; Ohta, T.; Nakao, A.; Waki, K.; Byon, H. R. Structurally tuning Li_2O_2 by controlling the surface properties of carbon electrodes: Implications for Li-O_2 batteries. *Chem. Mater.* **2016** *28*, 8006.

2. Yang, C.; Wong, R. A.; Hong, M.; Yamanaka, K.; Ohta, T.; Byon, H. R. Unexpected Li_2O_2 Film Growth on Carbon Nanotube Electrodes with CeO_2 Nanoparticles in Li–O_2 Batteries**.** *Nano Lett.* **2016**, *16*, 2969.

3. Thomas, M. L.; Yamanaka, K.; Ohta, T.; Byon, H. R. Perfluorinataed moiety-grafted carbon nanotube electrode for the non-aqueous lithium-oxygen battery. *Chem. Commun.* **2015**, *51*, 3977.

4. Bonnet-Mercier, N.; Wong, R. A.; Thomas, M. L.; Dutta, A.; Yamanaka, K.; Yogi, C.; Ohta, T.; Byon, H. R. A structured three-dimensional polymer electrolyte with enlarged active reaction zone for Li-O_2 batteries. *Sci. Rep.* **2014**, *4*, 7127.

2.3.1 - Residual gas analyzers (RGA) and mass spectrometry

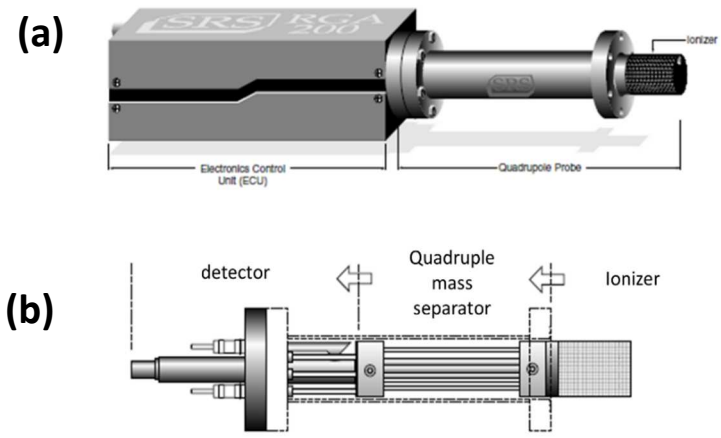

Figure 2.12 – Residual gas analyzer (RGA) manufactured by SRS (a) The unit consists of the electronics control unit and quadruple probe (b) The quadruple probe consists of the ionizer, quadruple mass separator and Faraday cup detector. [32]

Residual gas analyzer (RGA) allows for identification and potential quantification of gas mixtures. The RGA as a unit used at Byon IRU is manufactured from Stanford Research Systems (SRS, USA). The layout is illustrated in **Figure 2.12a** containing the electronics control unit and the quadruple probe. The quadruple probe consists of the ionizer, ion filter and ion detector components **Figure 2.12b**. Briefly stated, the entire process involves the (1) ionization of the sample molecules followed by (2) separation of the resulting ions by mass-to-charge ratio (m/z) and (3) the detection the separated ions.

The ionizer provides the electrons for ionization of the gas molecules by means of a heated filament consisting of a pair of thoria coated iridium (ThO_2/Ir) wires. This process of ionization requires low pressure typically at high to ultra-high vacuum conditions. Following ionization the ions are separated by means of the quadruple mass filter (**Figure 2.13**). The mass filter consists of four rods functioning as electrodes where the incoming ions are separated due to the forces caused by the potential (both DC (direct current) and RF (radio frequency) voltage) applied by the rods. The ions are consequently separated by their m/z ratio and by controlling the DC and RF potential the trajectory of the ions of interest can be

selectively filtered. Subsequently, the ions arrive at the detector which measures the ion current by means of a Faraday cup. The incoming ions strike the metal wall of the Faraday cup resulting in gain in charge and electron transfer where the current is proportional to the ion current.

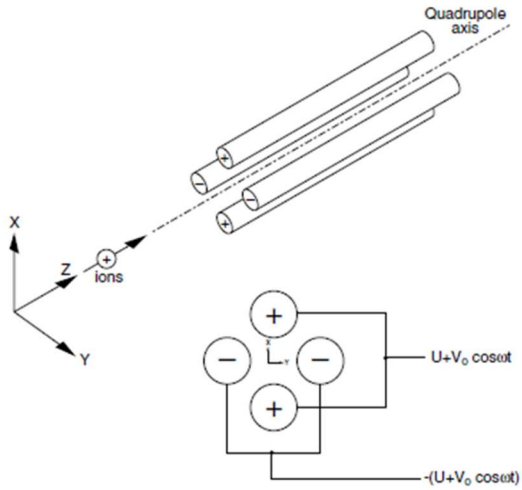

Figure 2.13 – Quadruple mass filter for separating incoming ions by mass-to-charge ratio[32]

2.3.2 – Construction of *in situ* OEMS (on-line electrochemical mass spectrometry)

This section convers the main aspects of the constructed an *in situ* on-line electrochemical mass spectrometry (OEMS), with additional discussion found in **Appendix A**. We note that the our setup uses periodic sample injection where the integral faradaic charge is proportional to the signal intensity and because of this, we use the broader term "on-line" instead of "differential", which commonly implies instantaneous sampling where the signal intensity is proportional to the instantaneous faradaic current. Based on the detailed descriptions and notable results demonstrated by McCloskey *et al*,[24] we decided to construct a similar system. The major components of the system can be separated into hardware and software components. The various components are broken down and explained the sections below: (1) Li-O_2 cell and GC switching valve for sample injection, (2) vacuum

components and (3) LabVIEW virtual instrument (VI), and electronics, which automates the data acquisition and valve manipulation.

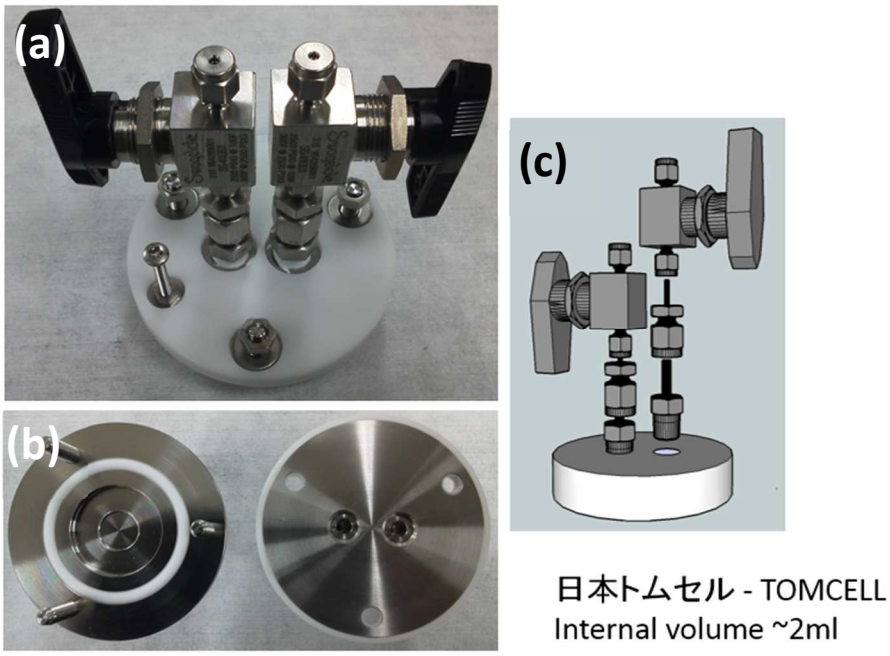

Figure 2.14 – *in situ* on-line electrochemical mass spectrometry (OEMS) cell utilized for the gas analysis measurements (a) Cell in its assembled form (b) (left) top view of the cell base (right) view of the cell top which fits onto the cell base (c) drawing showing how the Swagelok components fit to the cell top.

(1) *Li-O_2 OEMS cell and GC switching valve* – The OEMS cell (**Figure 2.14**) was designed with the assistance of Tomcell® and is similar to standard cell except with drastically decreased cell headspace of ~2 mL of volume in order to increase the ratio of gaseous product to the Ar carrier gas and allow for highly sensitive measurements from the mass spectrometer. The sample injection is made possible with gas chromatography (GC) 2-way, 6-port valve (EHLC6WM, VICI Valco instruments), where the two positions are labeled “position 1 and position 2” in **Figure 2.15a**. Both of these values are 3 way Swagelok valves. Valve “a” allows us to switch between O_2 and Ar, for discharge and recharge, respectively, while valve “b” which is typically in the closed during OEMS operation and furthermore, can also allow the purging/venting of the cell without exposing the cell to vacuum. The cell is connected with stainless steel tubing (1/16”) and polyether ether ketone

(PEEK) tubing to ports 3 and 4 of the switching valve (to ensure electrical isolation of the cell), where there is a high precision pressure transducer (MMA030V5P3A6T3A5CE, Omega Engineering) present between the cell inlet and port 3.

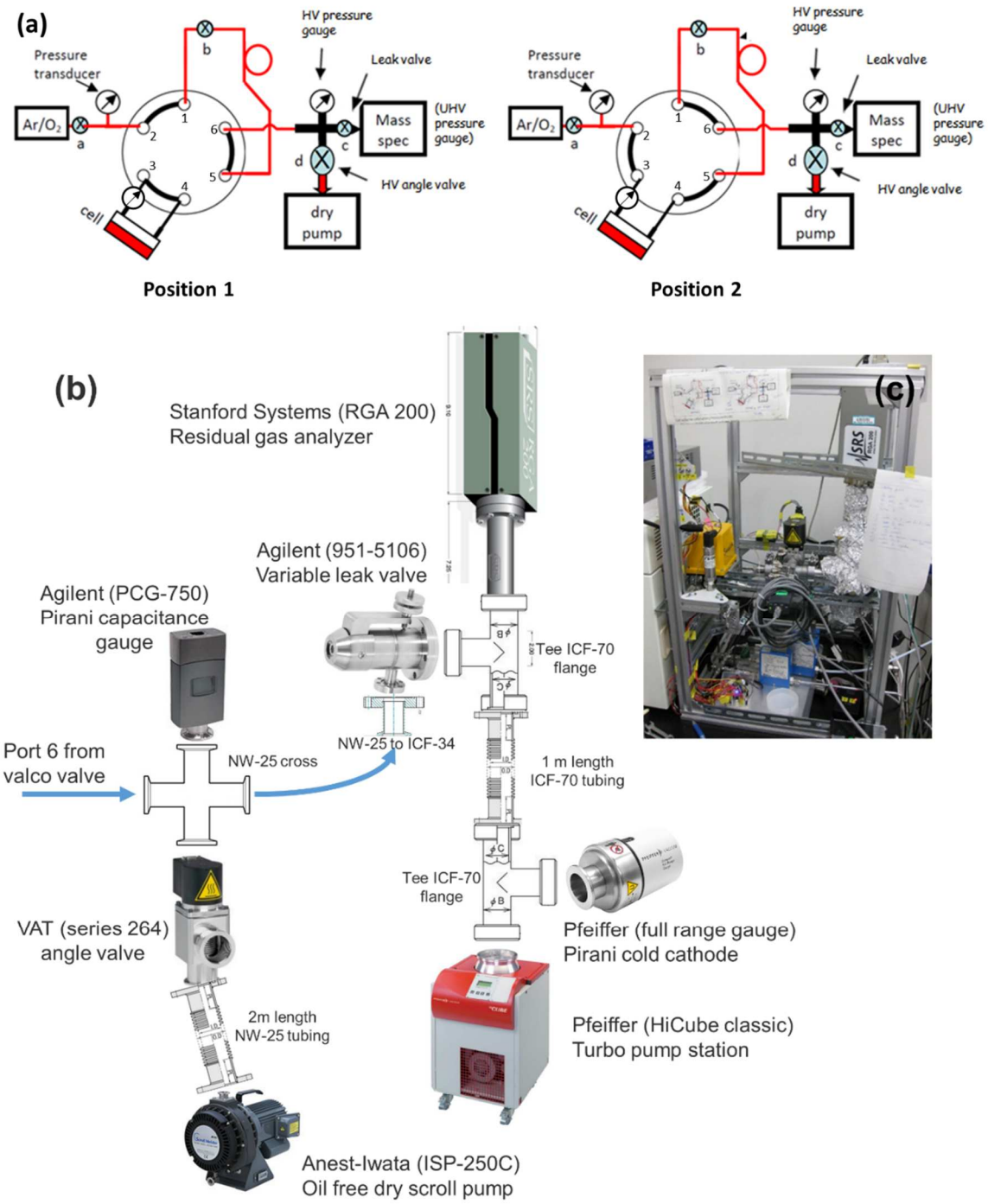

Figure 2.15 – OEMS system overview (a) Schematic diagram of the two positions of the 6-port gas injecting switching valve with port numbers labeled 1 to 6 (b) Schematic diagram of the vacuum components of the system and (c) digital photograph showing partial view of the OEMS system.

(2) *Vacuum components* - The vacuum components and the way they are connected is summarized in **Figure 2.15b**. The setup features differential pumping with high vacuum (HV) connected via flexible tubing of 2 and 1 m, respectively for the ~1×10^{-3} mbar, Scroll Meister ISP-250C, Anest Iwata and near ultra-high vacuum (~3×10^{-8} mbar, TurboCube TSU-61, Pfeiffer) stages (after baking overnight at 150^{o}C). The vacuum gauges (Agilent, PCG-750 and Pfeiffer PKR 251) and computer controlled high vacuum angle valve (VAT series 264, denoted as valve "d"). Connecting the high vacuum is a variable leak valve (Agilent, 951-5106, denoted as valve "c"), where the near ultra-high vacuum mass spectrometer (Stanford systems, RGA-200) chamber is situated.

(3) *LabVIEW interface* - The OEMS system was automated using a LabVIEW (National instruments) virtual instrument (VI) interface, allowing for automated data acquisition from the mass spectrometer, pressure sensors, and for the automated control of opening and closing the HV angle valve. Utilizing LabVIEW VI framework provided by the residual gas analyzer (MS) manufacturer, Stanford Research Systems could be integrated with the rest of the custom VI. Moreover, the VI design is quite modular utilizing the so-called state machine architecture, which al lows for the different states (representing the different steps in operation (See **Appendix A** for additional discussion). The modular with a state machine architecture also allows for ease in modification and debugging purposes. The pressure transducer is interpreted by a 15-bit (scaled 0 to 4.096 V) analog to digital converter (ADC) (Adafruit industries) ensuring sufficient precision for pressure data acquisition. The quantized resolution of the pressure data acquisition equates to 0.0008 psi.

Chapter 3

Elucidating the role of the surface properties of carbon electrodes in structurally tuning $L_{i2}O_2$ for Li-O_2 batteries

3.1 - Introduction

Possessing one of the highest theoretical specific energies amongst all rechargeable battery chemistries (~3.5 kWh/kg), rechargeable Li-O_2 batteries have the potential to promote the electrification of transport and the ability to effectively harness energy from sustainable, but intermittent sources such as solar and wind [1-4]. The ideal electrochemistry of gaseous oxygen and lithium ions in an aprotic electrolyte yields the reversible reaction, $2Li^+ + O_2 + 2e^- \leftrightarrow Li_2O_2$ (E^o = 2.96 V vs Li/Li^+), where the discharge product is solid-phase Li_2O_2 [2,5]. Despite the promise of Li-O_2 batteries, development is still in its infancy with deficiencies in the understanding of the Li_2O_2 formation and decomposition processes occurring during discharge (DC) and recharge (RC), respectively.[2,4] This is further complicated by well documented challenges associated with electrode and electrolyte instability,[6-11] poor reversibility and cycleability,[1,3,12,13] lower-than-theoretical capacity,[14,15] and low round-trip efficiency,[4,16] which should be resolved to realize practical and high performance Li-O_2 batteries.

It should be emphasized that in order to achieve the desired specific energy densities required for practical Li-O_2 batteries, it is crucial to employ lightweight materials for the positive electrode. To this regard, few materials are competitive with carbon due to its

numerous advantages including weight, cost, abundance, porosity and conductivity [17]. Moreover, carbon itself is very active for the formation of Li_2O_2 (oxygen reduction reaction (ORR) during DC) in Li–O_2 cells [5,18,19]. On the other hand, the choice of carbon has been questioned as evidenced by several studies showing formation of lithium carbonates (Li_2CO_3 and lithium alkyl carbonates) and lithium carboxylates ($LiCO_2R$, R is hydrogen or alkyl), owing to instabilities from LiO_2 and Li_2O_2 species, which is exacerbated at high potentials [6,20]. These findings have prompted researchers to pursue alternative materials to carbon. Notable attempts using nanoporous Au and TiC studied by Bruce and coworkers, showed significant improvements in reversibility and cycleability [11,21]. Conversely, additional studies by McCloskey *et al.* indicated that nanoporous Au and TiC showed similar to lower O_2 evolved/consumed ratios compared to carbon through quantitative *in situ* gas analysis [2,3,7]. These findings show that any departure from carbon-based electrodes remains challenging, notwithstanding the additional practical issues, including increased cost and weight, which would negatively impact the specific energy. Provided the suppression and mitigation of the challenges associated with stability, carbon remains a highly attractive and practical electrode material. The aforementioned reasons and the continued wide-use of carbon has promoted us to investigate the role of the surface properties of carbon towards the electrochemical behavior of Li-O_2 cells. Existing studies on carbon materials in Li–O_2 batteries have focused on comparing the effects of physical parameters including surface area and pore size effects [22,23] and have not been systematic in isolating the individual effects of surface functional groups from the effects of increased edge-plane exposure,[20,24] which we will show that this leads to substantially different behaviors. In all, a comprehensive effort to correlate the surface properties of carbon together with Li_2O_2 structure and Li–O_2 cell performance has not been carried out.

Herein, we highlight the importance of the surface chemistry of carbon, which notably affects the structure of Li_2O_2 and consequently, the electrochemical behavior of Li-O_2 cells. The use of carbon nanotubes provides a versatile platform due to the ease of surface modification from its well-defined structure, high electrical conductivity via the backbone of the inner walls and ability to fabricate binder-free electrodes [25]. The comparison between different commercial carbons (e.g. activated carbon, Super P, Ketjen black, etc) is often difficult due to the variations with respect to synthesis procedures, surface area, surface functional groups, surface morphology, and the degree of graphitization, all of which cannot be systematically controlled. By utilizing carbon nanotubes, the surface modifications could be controlled, which included the separation of oxygen-functional groups from undecorated edge plane exposure, and increased graphitization. We observe a correlation between the degree of disorder of the nanotube surfaces and DC capacity in $LiClO_4$/tetraglyme. Highly disordered surfaces and the inclusion of oxygen-functional groups lead to lower capacities and this is attributed to the provision of many nucleation sites possessing strong adsorption affinity to Li_2O_2 intermediates. The consequences of this predominant surface-based nucleation and growth causes the formation of amorphous Li_2O_2 film. Notably, the subsequent RC permits the lowest potential for decomposition of amorphous Li_2O_2. Further modulation of the degree of disorder and oxygen functional groups allows us to tune the resulting Li_2O_2 structure and furthermore, to delineate the origin of the wide range of Li_2O_2 oxidation potentials. This is the first report to suppress the RC overpotential of Li-O_2 cells by controlling the surface of the carbon electrode without the use of heavy and expensive promoter in either nanoparticle form or soluble redox mediator [16,26].

3.2 – Experimental

Pristine multi-walled carbon nanotubes (denoted as MWNT) were purchased from Sigma Aldrich have an outer diameter (ϕ) of ~10-20 nm and length of 5 μm. MWNTs functionalized

with oxygen-containing groups (denoted as Ox-MWNT) and defective edges were obtained through a chemical oxidation procedure based on previous reports [27]. Briefly, 500 mg of MWNTs were refluxed for 2 h at 70 ^{o}C in 75 mL of concentrated sulphuric acid and 25 mL of concentrated nitric acid. After cooling at room temperature for 50 min, the mixture was diluted with 400 mL of 5% hydrochloric acid solution. The resulting mixture was filtered under vacuum through PTFE membrane (pore size 0.45 μm, Millipore) followed by the further filtration of 2 L of deionized (DI) water (~18 MΩ). The Ox-MWNTs were then collected and dried in vacuum at 60 ^{o}C overnight. For tuning the surface property in Ox-MWNT (removal of oxygen-functional groups), the Ox-MWNTs were annealed in flowing Ar for 1 h at 500 ^{o}C (denoted as Ox-MWNT-500) or 900 ^{o}C (denoted as Ox-MWNT-900). Prior to the annealing process, the Ox-MWNT powders were vacuumed filtered through a polycarbonate track etched membrane (pore size 0.4 μm, Whatman) to make self-standing films after dispersing in isopropanol (Wako) by tip-sonication. This process allowed self-standing films to conserve its shape without cracking, thus the resulting surface-modified films could be directly used for electrode (see below). MWNTs with a higher degree of uniformity and increased degree of graphitization (denoted as G-MWNT) were prepared by annealing of as-received MWNT powders at 2800 ^{o}C for 10 min under Ar atmosphere in a horizontal graphite furnace (Kurata Giken, Japan).

Electrodes were fabricated with MWNT and Ox-MWNT by the grounding the as-prepared powders followed by mixing with 4 mL of isopropanol by tip-sonicating for 10 min. The sonicated mixture was vacuumed filtered through glass fiber (GF/C, Whatman) followed by drying at room temperature for several hours. The MWNT electrodes were free-standing and could be peeled off from the glass fiber and Ox-MWNT electrodes were used as-is without removing the glass fiber that was used as the separator. To prepare the G-MWNT electrodes, G-MWNT powder was dispersed in 8 mL of 1:1 volume ratio of N-methyl-2-pyrrolidone

(NMP, Wako) to isopropanol and tip-sonicated for 25 min. The resulting mixture was vacuum filtered through GF/C glass fiber, thoroughly dried at room temperature before cut into individual disks. Prior to cell assembly, all of the prepared electrodes were dried in vacuum at 120 ^{o}C (Büchi Glass oven, B-585) overnight before being transferred while still warm into the Ar filled glovebox without exposure to air. The mass of binder-free electrodes (ϕ 12 mm) was ~1.2 mg, with the exception of the electrodes used for the quantitative *in situ* gas analysis and peroxide titration measurements in **Figure 3.5** and **Table 3.2** which were ~2.0 mg. The discharge capacity and galvanostatic profile trends (to 2 V) is consistent with the electrode mass at 1.2 mg or 2.0 mg. Preloaded Li_2O_2 electrodes were prepared inside the Ar-filled glovebox (Korea, Kiyon) with <1 ppm of H_2O by grinding/mechanically mixing commercial Li_2O_2 (>99%, Kojundo Chemical Lab. Co.) with pristine MWNT or Ox-MWNT with a pestle and mortar. Subsequently the mixture submerged in super dehydrated isopropanol (Wako) and bath sonicated without exposure to air, which was then filtered through glass fiber GF/C before left to dry inside the glovebox. After cutting into individual electrodes, the electrodes were annealed at 60 ^{o}C in vacuum without exposure to air. The preloaded Li_2CO_3 (99%, Nacalai Tesque Inc.), $Li_2O_2/Li_2{}^{13}CO_3$ (99%, Sigma Aldrich) or Li_2O_2/CH_3CO_2Li (>98%, Wako) were made in a similar fashion. For the mixture compounds, the mass ratio of Li_2O_2 to $Li_2{}^{13}CO_3$ (or CH_3CO_2Li) was 4:1.

Electrochemical characterizations

Electrochemical tests for two-electrode configuration of Li–O_2 cells were performed with WBCS3000, WPG100e (WonATech), or VMP3 (Biologic) inside constant temperature chambers set at 25 ^{o}C. The on-line electrochemical mass spectrometry (OEMS) measurements were performed in the same fashion as described in detail in chapter 2. Three-electrode measurements were conducted inside an Ar-filled glovebox with A CH704E (ALS). The rotating ring disk electrode (RRDE) is composed of glassy carbon (GC) disk (ϕ 4 mm)

and gold (Au) ring (ϕ 5 mm inner and ϕ 7 mm outer, BAS). To prepare the inks, 5 mg of each materials were dispersed in 1 mL of isopropanol and 10 μL of LITHion solution (Ion Power, Inc.) with the exception of Ox-MWNT-900, which was dispersed in 1 mL of NMP and 10 μL of LITHion solution. The mixtures were gently sonicated inside a sealed vial to prevent vaporization of the solvent. A 6 μL aliquot of ink was dropped onto the GC disk and dried in ambient conditions. Prior to measurement, the RRDE was dried in a vacuum oven at 80 ^{o}C for ~4 h. Li metal was used as the reference and counter electrodes. The three electrode measurements were performed in 0.5 M $LiClO_4$ in tetraglyme with being swept from 3.3 to 2 V then reversed back to 3.3 V at the scan rate of 2 mV s^{-1}. The ring potential was held at 3.3 V_{ring} with the rotation rate set at 900 rpm.

Further characterization methods

For post DC or RC analysis, following electrochemical testing, the cell was purged with Ar before disassembly inside the Ar glovebox. The (surface-modified) carbon nanotube electrodes were extracted and soaked in 2 mL of acetonitrile (<5 ppm H_2O, 99%, Wako) for 25 min then washed with an additional 2 mL of acetonitrile before drying overnight in vacuum at 60 ^{o}C. Transmission electron microscopy (TEM) of the as-prepared materials was conducted using a JEOL JEM-2100F with an acceleration voltage of 200 kV. TEM of the DC electrodes were performed with a JEOL JEM-1230 at acceleration voltage of 80 kV. Scanning electron microscopy (SEM) was conducted using a Hitachi S-4800T with an acceleration voltage of 5-10 kV. Raman spectroscopy was carried out using He-Ne laser excitation (632.8 nm). N_2 adsorption-desorption isotherms were obtained using a BELSORP-mini II (BEL) with pore size distribution estimated by Barrett-Joyner-Halenda (BJH) method. X-ray diffraction (XRD) analysis was obtained using SmartLab, Rigaku with Cu Kα with $\lambda \approx$ 1.542 Å. The XRD samples were put onto a glass holder and sealed with MICTRON^{TM} (Toray) film inside the glovebox to ensure no exposure of the sample to air. Fourier transform

infrared (FTIR) spectroscopy was conducted using Thermo Fisher Scientific Nicolet iS50, with wavenumber range of 500 to 4000 cm^{-1} without exposure to air using an Ar-filled glovebox accessory. The sample pellets were prepared by mechanically grinding electrodes with CsI powder (>99.99%, Kanto Chemical Co.) in the glovebox. The reference powders included Li_2O_2 (>99%), LiOH (>98%, Merck Chemicals), Li_2CO_3 (99%), $HCO_2Li{\cdot}H_2O$ (98%, Sigma Aldrich), CH_3CO_2Li (>98%) and $LiClO_4$ (Battery grade, Aldrich), which were dried in vacuum at 60ºC prior to measurement. For the titration to determine the Li_2O_2 yield, the DC electrode along with separator was submerged in 10 mL of $TiOSO_4$ inside a vial and vigorously shaken for 1 min [28,29]. The UV-Vis spectroscopy measurement was conducted with a Shimadzu UV-3600 after 30 min of soaking. Quantification could be achieved by correlating the measured absorbance with a calibration curve performed with commercial Li_2O_2 (>99% purity). X-ray absorption near-edge structure (XANES) spectroscopy measurements for O K-edges in bulk-sensitive partial fluorescence yield (PFY) and surface-sensitive total electron yield (TEY) modes were performed at BL11 (soft X-ray beamline) at the Synchrotron Radiation (SR) Center at Ritsumeikan University. The XPS measurements in **Figure 3.1** (PHI ESCA 5400MC) were conducted with monochromatized Al-Kα (1486.6 eV) X-ray source. The pass energy was 71.55 eV (wide scan) and 35.75 eV (individual narrow scan). The samples for XANES and XPS were dried in vacuum at 80 ºC before inserting into a transfer vessel inside a glove box, which permitted transfer into the XANES and XPS chambers without exposure to air. The XPS data in **Figure 3.9** (VG ESCALAB 250, Thermo Fisher Scientific) with Al-Kα (1486.6 eV) X-ray source and pass energy of 50.0 eV (wide scan) and 20 eV (individual narrow scan). The RC electrodes were extracted in the same manner as described above for post DC-RC analysis. The C1s peak referenced to 284.5 eV for sp^2 hybridized carbon which was fitted to G-MWNT and sp^3 hybridized carbon centered at 285.2 eV. Additional assignments were C-O at 286.0 ± 0.1 eV, C=O at 286.9 ± 0.2 eV, and

COO- at 288.9 ± 0.2 eV.[17,30,31] The relative compositions are ascertained from the individual elemental peak areas and using the appropriate atomic sensitivity factors. Temperature programmed desorption (TPD, ESCO, EMD-WA1000S) was performed with a quadrupole mass spectrometer (QMG 422). The measurement as-prepared Ox-MWNT electrode sample was conducted under ultra-high vacuum conditions (base pressure 2.0 $\times 10^{-7}$ Pa) with a ramp rate 30 ^{o}C min^{-1} to the cut off temperature of 1000^{o}C.

3.3 – Results and discussion

3.3.1 - Surface characteristics of modified carbon nanotubes

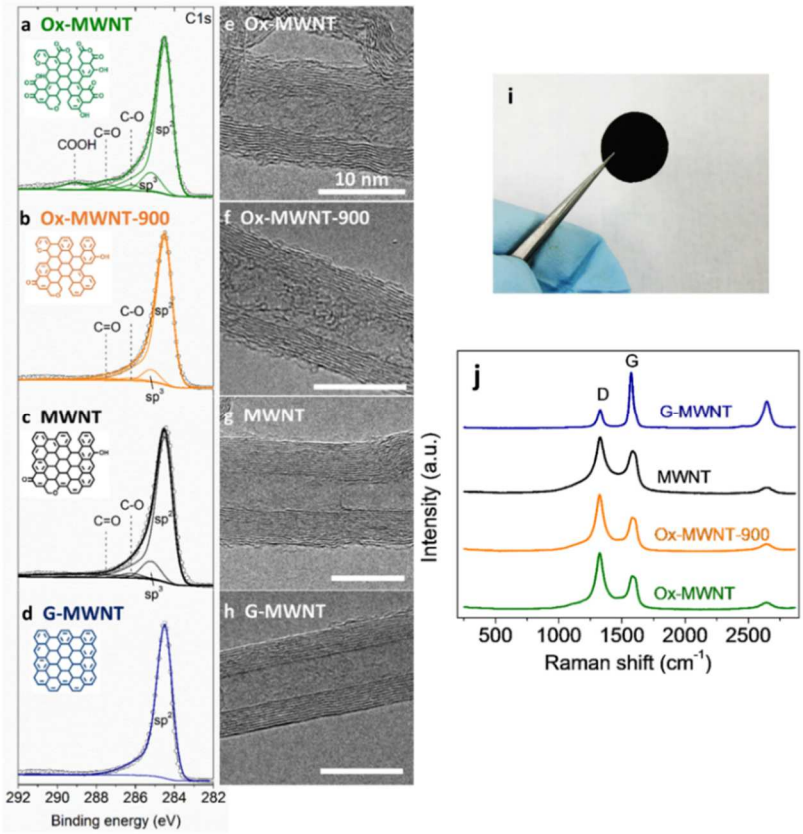

Figure 3.1 - Characterizations of surface-modified carbon nanotubes using XPS (left panel) and TEM (right panel) (a-d) XPS C 1s spectra for (a) oxygen-functionalized MWNT (Ox-MWNT), (b) defective carbon nanotubes after removal of oxygen functional groups from Ox-MWNT (Ox-MWNT-900), (c) pristine MWNT (MWNT) and (d) MWNT with high degree of graphitization (G-MWNT). The insets show schematic representations of the carbon surfaces. (e-h) Corresponding TEM images of (e) Ox-MWNT, (f) Ox-MWNT-900, (g) MWNT and (h) G-MWNT. All scale bars represent 10 nm (i) digital photograph of typical as-prepared electrode (j) Raman spectroscopy of the as-prepared electrodes with I_D/I_G ratio shown in Table 3.1.

We have studied four materials derived from pristine multi-walled carbon nanotubes (diameter 10~20 nm, length ~5 μm) with different surface characteristics including (1) the pristine carbon nanotubes themselves, (2) introduction of oxygen functional groups, (3) the introduction of defective edge planes and (4) high uniformity through graphitization (see Supporting Information (SI) for detailed methods). The pristine carbon nanotubes were used as-received (denoted hereon as MWNT). Oxygen containing functional groups were introduced onto the outer surfaces of MWNTs (denoted hereon as Ox-MWNT) by chemical oxidation in concentrated acid solution at 70 ^{o}C.[27] The removal and thermal decomposition of oxygen functional groups to achieve defective edges was conducted by annealing Ox-MWNT under Ar atmosphere at 900 ^{o}C (denoted hereon as Ox-MWNT-900).[32] To remove defects and create highly ordered graphitic surfaces, rearrangement of carbon nanotube structure is required under very high temperatures.[33] This could be achieved by annealing of pristine MWNTs at 2800 ^{o}C in Ar (denoted hereon as G-MWNT).

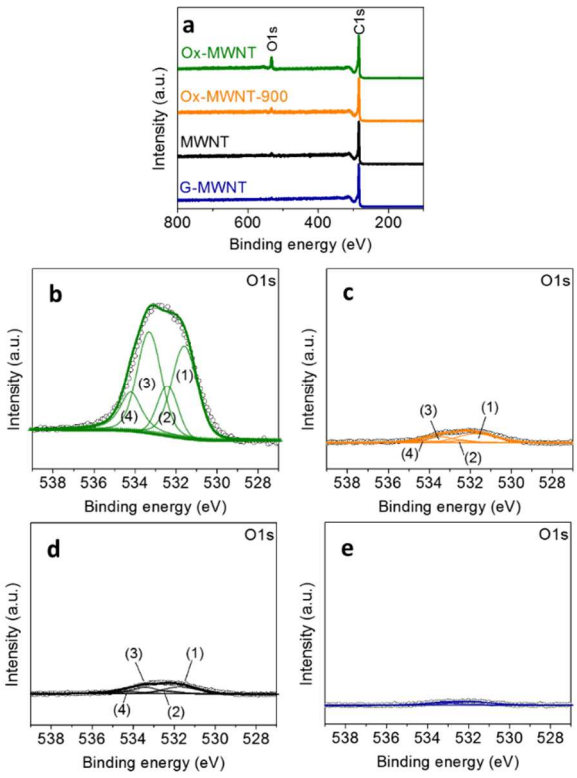

Figure 3.2 - XPS of as-prepared electrodes. (a) Wide scan (b-e) O 1s binding energy region for (b) Ox-MWNT, (c) Ox-MWNT-900, (c) MWNT and (d) G-MWNT respectively. The intensities are normalized to the C1s sp^2 peak (at 284.5 eV). The deconvoluted peaks are assigned to: (1) carbonyl group at 531.6 eV, (2) ether group at 532.3 eV, (3) anhydride group at 533.3 eV and (4) carboxyl group at 534.2 eV.[31,34]

Table 3.1 - Summary of structural characteristics of surface-modified carbon nanotubes

	Ox-MWNT	**Ox-MWNT-900**	**MWNT**	**G-MWNT**
XPS (atomic ratio of O/C)	0.095	0.013	0.010	0.004
Raman (I_D/I_G)	1.67	1.64	1.23	0.31
BET S_A (m^2 g^{-1})	231	295	244	216

Atomic ratio of oxygen relative to carbon (O/C) from XPS, peak intensity of D to G bands (I_D/I_G) from Raman, and BET surface area from N_2 adsorption-desorption isotherm. The individual plots are presented in Figure A1-A4.

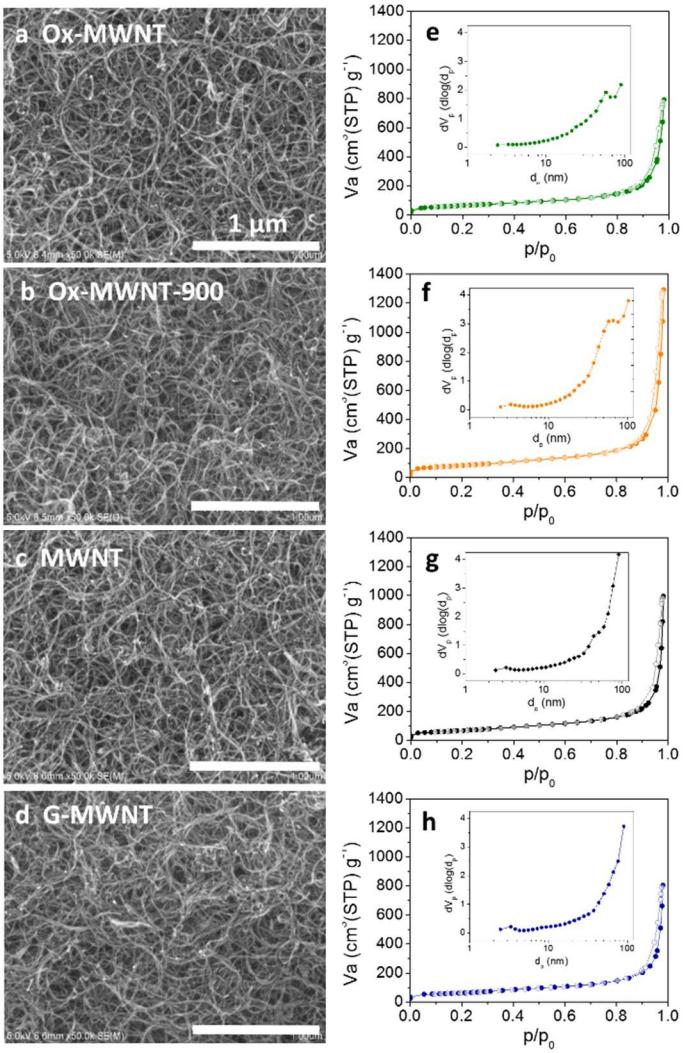

Figure 3.3 - Digital and SEM images of as-prepared electrodes and N_2 adsorption-desorption isotherms. (a) Digital photograph of binder-free MWNT electrode. (b-e) SEM images of (b) Ox-MWNT, (c) Ox-MWNT-900, (d) MWNT and (e) G-MWNT electrodes. All scale bars indicate 1 μm. (f-i) Corresponding N_2 adsorption-desorption isotherms with pore size distributions (inset).

The surface properties were analyzed with respect to specific oxygen functionalities and degree of disorder of the carbon structure. The X-ray photoelectron spectroscopy (XPS) wide scan survey indicates the atomic ratio O/C of 0.095 present in Ox-MWNT, which is a 9.5-fold increase from pristine MWNT (**Table 3.1** and **Figure 3.2**). The oxygen-containing functional groups in Ox-MWNT are composed of C–O (e.g. phenol, ether and epoxy, at 286.0 ± 0.1 eV), C=O (e.g. carbonyl and quinone, 286.9 ± 0.2 eV) and –COO– (e.g. carboxylic acid, carboxyl, carboxyl anhydride, ester and lactone, 288.9 ± 0.2 eV) from the XPS C 1s spectrum (**Figure 1a**), which also corresponds to the peaks assigned in O 1s spectrum (**Figure 3.2b**) [6,17,31]. These oxygen moieties are mostly removed after annealing at 900 ^{o}C in Ar as shown by the small oxygen-moiety peaks in Ox-MWNT-900 from XPS **(Figure 3.1b** and **Figure 3.2c**) with ~7-fold decrease in atomic ratio of O/C compared with Ox-MWNT [17]. Nevertheless, the degree of disorder of the nanotube surfaces is comparable for both Ox-MWNT and Ox-MWNT-900: The transmission electron microscopy (TEM) images show notably roughened outer nanotube walls (**Figure 3.1e** and **3.1f**). In addition, Raman spectroscopy reveals the similar D-band (I_D, representative of disorder) to G-band (I_G, graphite)[35] intensity ratios at 1.6~1.7 (**Table 3.1** and **Figure 3.1j**). These results demonstrate that the Ox-MWNT-900 contains the prevalence of disordered edges which remain after the elimination of oxygen functional groups following annealing at 900 ^{o}C. In addition, the preparation of these samples allows us to decouple the role of oxygen functional groups (Ox-MWNT) from defective edges (Ox-MWNT-900) [32]. Pristine MWNT contains comparable O/C to Ox-MWNT-900, but lower I_D/I_G ratio at 1.23 (**Table 3.1, Figure 3.1c** and **3.1g**). After graphitization at 2800 ^{o}C, G-MWNT contains extensive sp^2 carbon (**Figure 3.1d**) shown by the seamless and uniform outer walls (**Figure 3.1h**) as demonstrated by markedly low I_D/I_G ratio at 0.31 with negligible O/C ratio (**Table 3.1**). The binder-free films of each sample prepared by vacuum filtration process (**Figure 3.1i**) show comparable BET (Brunauer-Emmett-Teller) surface

areas between 200~300 m^2 g^{-1} with nonporous nature, measured by the N_2 adsorption-desorption isotherms (**Table 3.**1 and **Figure 3.3**). The similar pore-size distributions increasing at 100 nm are the contribution from the inter-nanotube gaps and spaces of the criss-crossing network,[32,36] visually shown by scanning electron microscopy (SEM, **Figure 3.3**).

3.3.2 - Discharge (DC) and recharge (RC) characteristics in Li-O_2 cells

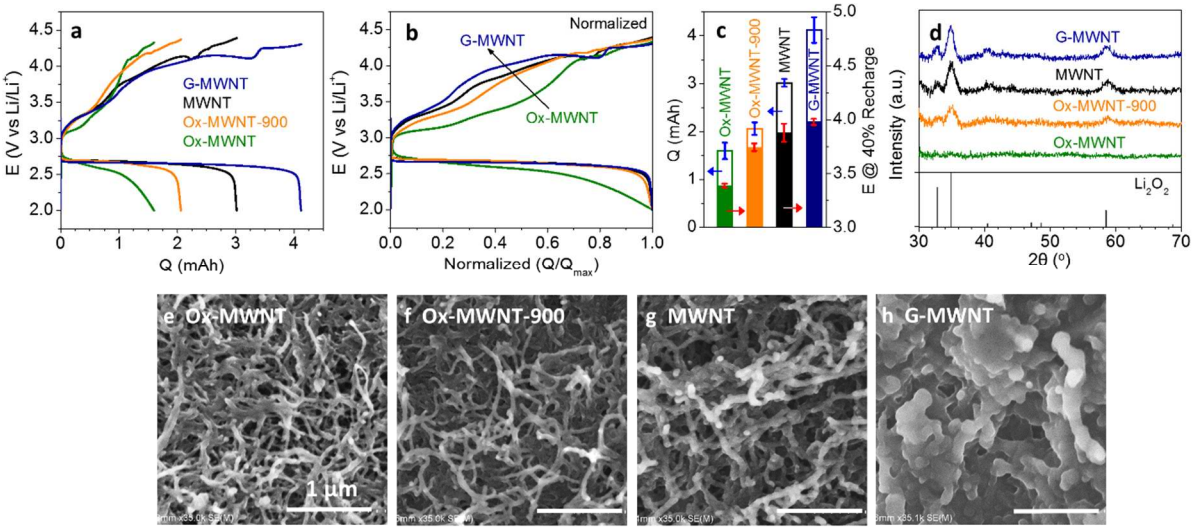

Figure 3.4 - Galvanostatic (full) discharge (DC) and recharge (RC) profiles of the first cycle performed with 0.5 M $LiClO_4$/tetraglyme at 50 mA g^{-1} and DC electrode analyses (a) DC-RC of Ox-MWNT (green), Ox-MWNT-900 (orange), MWNT (black) and G-MWNT (navy blue). (b) Normalized capacity curves of (a). (c) Bar graphs to compare DC capacity differences (left) and RC potential at 40% process (right). (d–h) Corresponding (d) XRD results (Li_2O_2 reference JCPDS 09-0355) and (e–h) SEM images (scale bars: 1 μm).

Binder-free carbon nanotube films (individual mass of 1.2 mg) with the different surface characteristics were utilized as the positive electrode in the Li–O_2 cells with 0.5 M $LiClO_4$/tetraglyme (<20 ppm H_2O from Karl Fisher measurement). The use of tetraglyme gives thorough electrode wetting for all carbon nanotube films (brief discussion in **Appendix B**). Galvanostatic DC-RC profiles of the first cycle at the current density of 50 mA g^{-1} in **Figure 3.4a–b** show that the surface properties of carbon nanotube electrodes significantly influence the electrochemical characteristics and can be summarized by two key observations

(**Figure 3.4c**): (1) the capacities following DC (to 2 V) are larger with the more ordered carbon (i.e. increasing from Ox-MWNT, Ox-MWNT-900, (pristine) MWNT to G-MWNT, respectively), and (2) the RC potentials (up to ~40% of RC) is lower for the disordered carbon (from Ox-MWNT increasing to G-MWNT, respectively). The trend in RC potential is consistent regardless whether the DC cut-off potential is 2.0 V (normalized profiles in **Figure 3.4b**) or at the fixed capacity of 1.2 mAh (**Figure 3.5**). This implies that the DC and subsequent RC behavior originates from the carbon surface properties and is independent of the amount of Li_2O_2 or capacity.

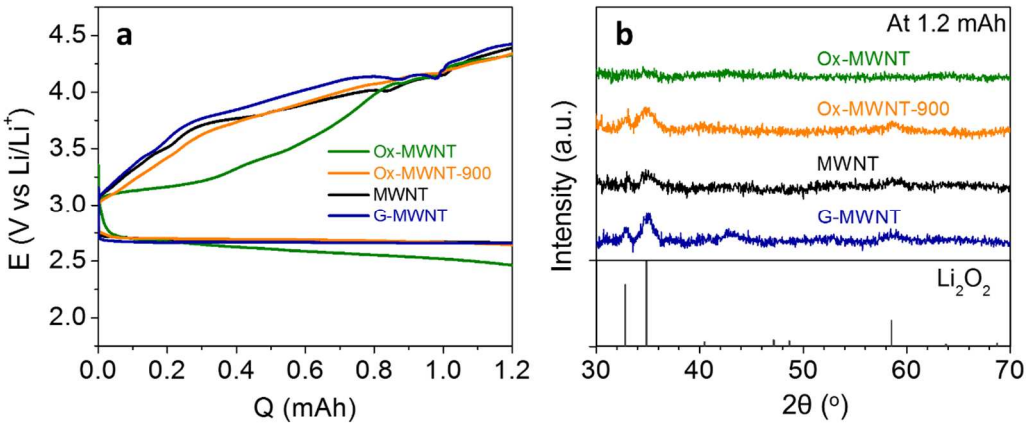

Figure 3.5 - Galvanostatic Li–O_2 cell tests at fixed capacity of 1.2 mAh and XRD result after discharge (DC). (a) Discharge-recharge (DC-RC) profiles performed with 0.5 M $LiClO_4$/tetraglyme at current density of 50 mA g^{-1}. (b) XRD pattern of DC electrodes to 1.2 mAh and reference of Li_2O_2 (bottom).

3.3.3 - Difference in DC capacities according to Li_2O_2 formation pathway

The DC capacities reveal the close correlation between the carbon surface characteristics and the pathway for Li_2O_2 formation. It has been established that the Li_2O_2 nucleation and growth processes is determined from the prevalent solvation and surface binding affinities of Li_2O_2 intermediates [37]. After ORR *via* the first e^-/Li^+ transfer on carbon surface (O_2* + e^- + Li^+ → LiO_2, the asterisk * denotes surface adsorbed species), the LiO_2 intermediate can be mobile in the electrolyte (indicated as LiO_2(sol)) and forms Li_2O_2

by disproportionation ($2LiO_2(sol) \rightarrow Li_2O_2(s) + O_2$), provided that the solvation affinity is predominant over the surface-binding affinity to the carbon surface. The resulting solvation-based nucleation and growth allows for larger and aggregated Li_2O_2 particles with apparent polycrystalline features [38,39]. This type of Li_2O_2 has been widely reported in various carbonaceous electrodes, in particular at low specific current rates [4,16,38]. We also observed Li_2O_2 particles (**Figure 3.4h** and **3.6c**) with Li_2O_2 crystal structure reflections (**Figure 3.2d**) in G-MWNT. In addition, G-MWNT has the largest DC capacity (~4.2 mAh with an average thickness of product of ~140 nm on the topmost electrode surface, **Figure B5**), implying the occurrence of solvation-based Li_2O_2 growth, allowing for the circumvention of charge transport limitations in the wide-bandgap Li_2O_2 [4]. A previous computational report indicated the high mobility of O_2 and LiO_2 from the difficulty in its adsorption on the perfect graphite (0001) plane[40] which is consistent with the poor Li_2O_2 wetting and aggregated Li_2O_2 growth with the G-MWNT surface.

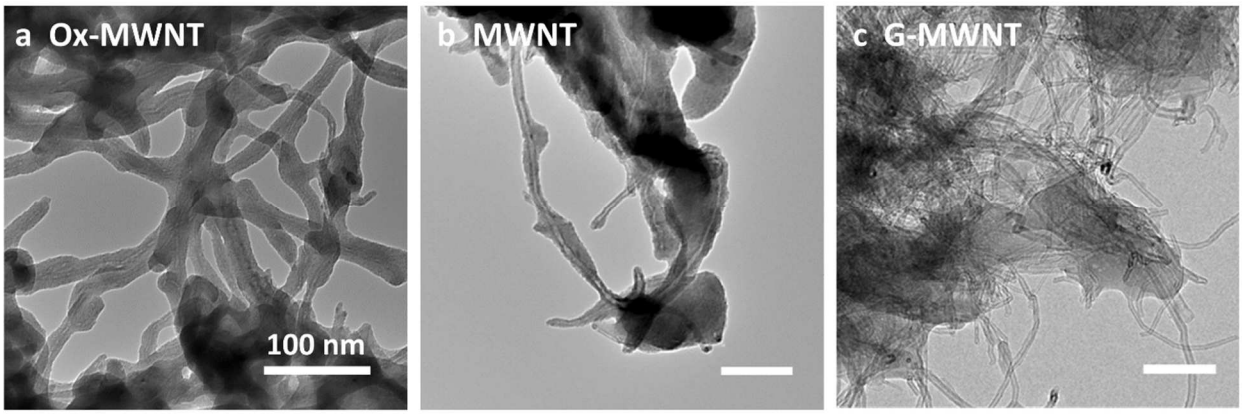

Figure 3.6 - TEM characterisations of DC product morphology at 1 mAh (a) Ox-MWNT (b) MWNT and (c) G-MWNT following DC to 1 mAh at current rate of 50 mA g^{-1}. The scale bars indicate 100 nm.

In comparison, pristine MWNT and Ox-MWNT-900 electrodes show relatively smaller capacities (~3 and 2 mAh with ~90 and 60 nm of product thickness, respectively, **Figure 3.7**) with the formation of more film-like Li_2O_2 (**Figure 3.4f-g** and **Figure 3.6b**). XRD patterns show a wider full width at half maximum (FWHM) of the Li_2O_2 101 reflection

(2θ = 35.1°) compared to G-MWNT **(Figure 3.4d** and **Figure 3.5b**, at fixed capacity of 1.2 mAh), indicating decrease crystal size presumably due to the presence of more defects. The less crystalline and film-like shaped Li_2O_2 suggests more favorable O_2 and LiO_2 binding with the carbon surface over solvation (donor numbers of tetraglyme and the anion ClO_4^- are moderate at 16.6 and 8.44 kcal mol^{-1}, respectively) [41,42]. Compared to G-MWNT, higher surface-binding affinity of O_2 and LiO_2 at the defective edges leads to more favorable nucleation of Li_2O_2 [40]. Our previous *in situ* electrochemical atomic force microscopy (EC-AFM) studies identified that Li_2O_2 nucleation occurs on the step edges of highly oriented pyrolytic graphite (HOPG) at low overpotentials, whereas the basal plane remains bare even at high overpotentials during the ORR process [43]. Therefore, more defective sites in Ox-MWNT-900 and MWNT can lead to more surface-based nucleation and subsequent growth of Li_2O_2, which promotes electrode passivation and reduces capacities.

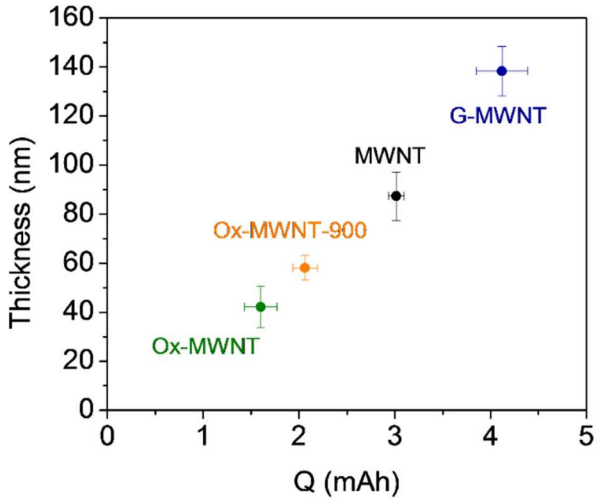

Figure 3.7 - Correlation of DC product thickness with capacity at cut-off voltage of 2 V. The thicknesses of DC products were measured from SEM analyses where MWNTs diameter of 10~20 nm were included. The capacities were obtained from three or more independent Li-O_2 cells.

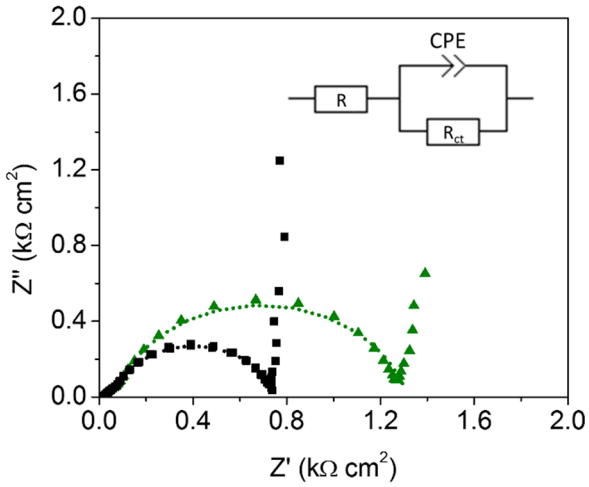

Figure 3.8 - Nyquist plots of Li–O_2 cells with (a) Ox-MWNT (green) and (b) MWNT (black) electrode from electrochemical impedance spectroscopy (EIS) at a frequency region of 10^{-1} to 10^6 Hz at an alternating current (AC) potential of 10 mV. The inset indicates the corresponding equivalent circuit used for fitting. The ohmic resistance of the cells as indicated by the intersection at high frequency[25,44] are comparable at 18 and 19 Ω cm^2 for Ox-MWNT and MWNT, respectively. Additionally, the EIS fitting indicates the charge-transfer resistances (R_{ct})[45] are 1.25 and 0.69 kΩ cm^2 for Ox-MWNT and MWNT, respectively.

In contrast, the presence of oxygen functional groups on Ox-MWNT shows the overwhelming preference for surface-adsorption-based nucleation and growth. Ox-MWNT containing cells deliver the lowest capacity (~1.5 mAh with ~40 nm of product thickness, **Figure 3.7**) although the measure of disorder (I_D/I_G, 1.6~1.7) is similar to Ox-MWNT-900. More notably, the continuity of the gentle potential decrease is shown in the DC profile unlike the flat plateaus present in other electrodes (**Figure 3.4b** and **Figure 3.5a**). The higher charge-transfer resistance (R_{ct}) of Ox-MWNT (1.25 kΩ cm^2) than the other electrodes (R_{ct} of MWNT: 0.69 kΩ cm^2, electrochemical impedance spectroscopy (EIS) in **Figure 3.8**) is not the central reason for the potential decrease, where Ox-MWNT presents the lowest overpotential at the initial stages of DC (**Figure 3.10**). Instead, this is inferred from the prompt passivation of the electrode surfaces with oxygen functional groups as starting points for surface adsorption, nucleation and growth of Li_2O_2 (LiO_2* + Li^+ + e^- → Li_2O_2 *via* the second e^-/Li^+ transfer), which leads to the stifling effect of charge transport limitations (**Figure 3.2e**). The TEM image of Ox-MWNT following 1 mAh of DC (**Figure 3.3a**)

indicates demonstrates conformal Li_2O_2 films without any pinhole of exposed bare electrode surface, which is in contrast to the inhomogeneous films on MWNT and sparse products on G-MWNT (**Figure 3b–c**). The high coverage of the electrode with Li_2O_2 film dramatically impedes charge transfer, causing the DC process to swiftly terminate. The conformal film is comprised of an amorphous structure as evidenced by no clear Li_2O_2 reflections from the XRD pattern (**Figure 3.4d** and **Figure 3.5b**). The additional chemical analysis with the O K-edge X-ray absorption near-edge structure (XANES) of Ox-MWNT after DC (**Figure 3.20**) shows the apparent σ*(O–O) feature, addressing the major product as Li_2O_2. A previous computational study has suggested that the oxygen functional groups (e.g. carbonyl and anhydride) have catalytic activity for ORR with the first e^-/Li^+ transfer,[40] which is demonstrated from the low overpotential at the initial stage of DC (**Figure 3.11**). The oxygen functional groups also stabilize LiO_2 by forming a chelating structure (e.g. $O_2Li\cdots O{=}C$ on carbonyl group) that expands and covers on the electrode during DC, while this requires high overpotential for the subsequent e^-/Li^+ transfer [40]. This prediction can support the greater uniformity in Li_2O_2 wetting with the Ox-MWNT electrode and the formation of amorphous Li_2O_2 (denoted hereon as *a*-Li_2O_2), where many adsorbed LiO_2 species may be irregularly

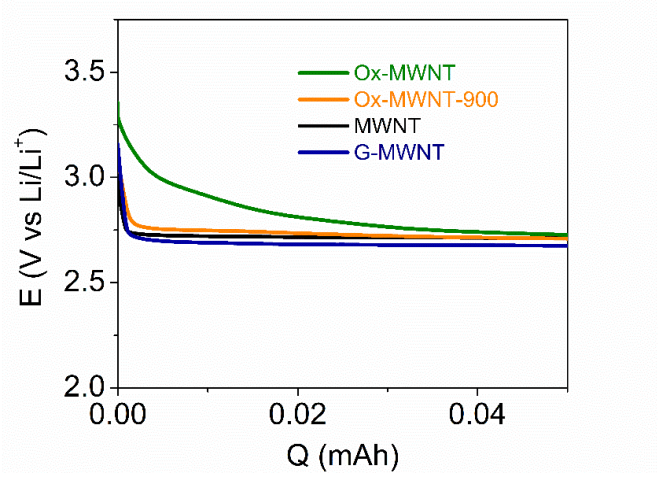

Figure 3.10 - Closer view of DC potential profile at initial DC region (captured from Figure 2a). The Ox-MWNT show notably lower overpotential at initial DC compared to other electrodes. The overpotential is higher with the more ordered carbon electrodes.

arranged prior to the second reduction. Further demonstration of the kinetics of ORR can be evaluated from the three-electrode cells. Figure 4a shows the cathodic linear sweep voltammograms (LSVs) performed at sweep rate of 2 mV s^{-1} and rotation of 900 rpm. The Ox-MWNT shows the fast ORR kinetics (~2.75 V at the current density of –0.1 mA cm^{-2}) compared to Ox-MWNT-900 and MWNT (~2.70 V at –0.1 mA cm^{-2}, **Figure 3.11**), while G-MWNT shows sluggish ORR (~2.58 V) due to lack of favorable O_2 adsorption sites. All these initial ORR behaviors are in good agreement with the initial overpotential trend from the DC profiles (**Figure 3.10**). In addition, the Li_2O_2 nucleation and growth process can be inferred as the potential is swept to 2.0 V, (**Figure 3.9a**). Ox-MWNT shows the gradual and small increase in cathodic current related to the rapid surface passivation which hinders the ORR process (**Figure 3.9b**). On the other hand, G-MWNT, with preference for the solvation-based process has less passivated electrode surfaces and shows a pronounced increase in cathodic current (**Figure 3.9c**). In addition, with the Au ring held at 3.3 V_{ring} the rotating ring disk electrode (RRDE) detects LiO_2(sol) species in the electrolyte ($LiO_2(sol) \rightarrow Li^+ + O_2 + e^-$, **Figure 3.9a** and **Figure 3.11**, top panels). The ring current reaches 3 μA cm^{-2}_{ring} at ~2.58 V for G-MWNT which is identical to the initial disk ORR potential (at –0.1 mA cm^{-2}), while ~2.55 V for Ox-MWNT which is 200 mV delayed from ORR on the disk (~2.75 V). This result confirms the weak LiO_2 adsorption to the G-MWNT surface, leading to a significant degree of solvated LiO_2 species. On the contrary, for Ox-MWNT, LiO_2(sol) is notably suppressed due to predominant surface-based growth.

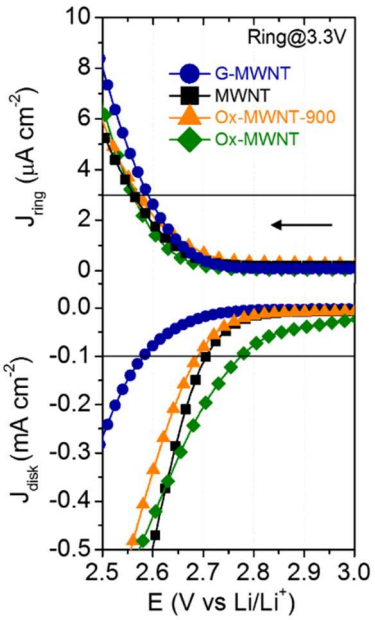

Figure 3.11 - Closer view of cathodic LSV with ring current response (a potential of 3.3 V_{ring}) at initial ORR (captured from Figure 4). Ring (top) and disk (bottom) current densities normalized to geometric area of the ring and disk respectively. The horizontal guidelines indicate 3 μA cm^{-2} for ring and –0.1 mA cm^{-2} for disk current densities for comparison of potentials.

3.3.4 - Difference in RC potentials from Li_2O_2 structure

Turning our attention to RC, where it appears that *a*-Li_2O_2 on Ox-MWNT can facilely decompose (overall: $Li_2O_2 \rightarrow O_2(g) + 2e^- + 2Li^+$). *In situ* on-line electrochemical mass spectrometry (OEMS, **Figure 3.12a** and **3.12b**), reveals the lowest RC potential for Ox-MWNT (3.0~3.5 V at the first half (50%) of RC) coinciding with greater amounts of O_2 evolution (O_2 amount is 15% greater) for the first 50% of RC amongst all carbon nanotube electrodes. In comparison, the Ox-MWNT-900, MWNT and G-MWNT show broadly comparable O_2 evolution and RC potential profiles but with the trend of higher potentials for the more ordered carbon electrodes. We note that the investigation of the initial RC behavior prior to 3.5 V is crucial to understand the true decomposition behavior of Li_2O_2 because less side reactions take place in this potential range. The RC at higher potentials will be discussed along with the inclusion of parasitic side reactions in the subsequent section.

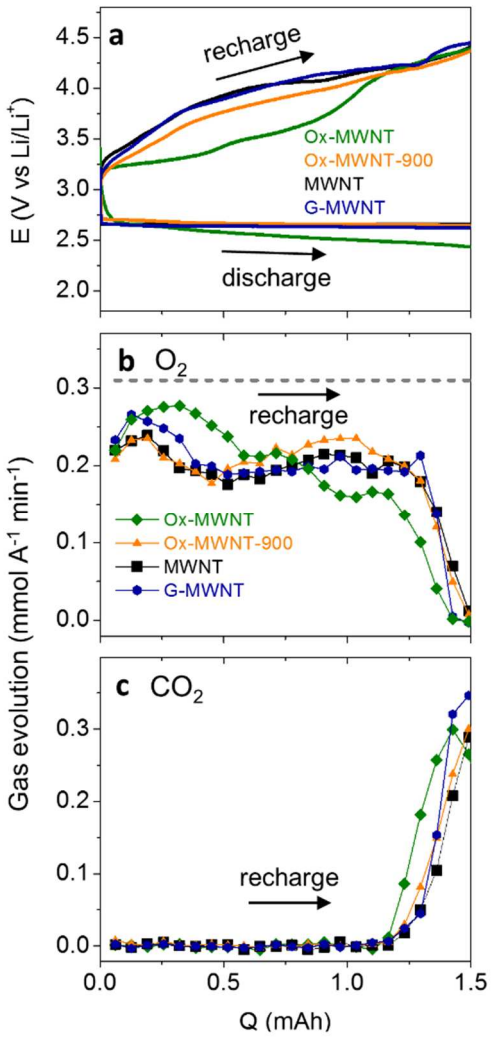

Figure 3.12 - *In situ* on-line electrochemical mass spectrometry (OEMS) analysis of RC at fixed capacity of 1.5 mAh with 0.5 M $LiClO_4$/tetraglyme, and current density of 50 mA g^{-1}. (a) DC-RC profiles (b-c) Corresponding (b) O_2 and (c) CO_2 evolution rates during RC. The dashed line in (b) indicates the 2 e^-/O_2 evolution rate.

The difference in Li_2O_2 decomposition potentials is ascribed to the Li_2O_2 structure and with negligible contribution from the carbon surface property itself. To confirm this hypothesis, polycrystalline Li_2O_2 particles (particle size <1 μm, >99% purity, **Figure 3.13a-c**) were preloaded on Ox-MWNT and MWNT. The resulting potential profiles and *in situ* OEMS (**Figure 3.12a–b**) reveal similar potential plateaus at ~3.7 V and O_2 evolution rates (overall ~2.6 e^-/O_2, **Figure 3.14**), which indicates the critical effect of Li_2O_2 structure to determine decomposition efficiency, instead of carbon surface property itself. This conclusion

is also consistent with the observation of lower decomposition potential of *a*-Li_2O_2 for first 50% of RC (**Figure 3.1a**) compared to the preloaded case with Ox-MWNT containing polycrystalline Li_2O_2 particles (**Figure 3.13d**).

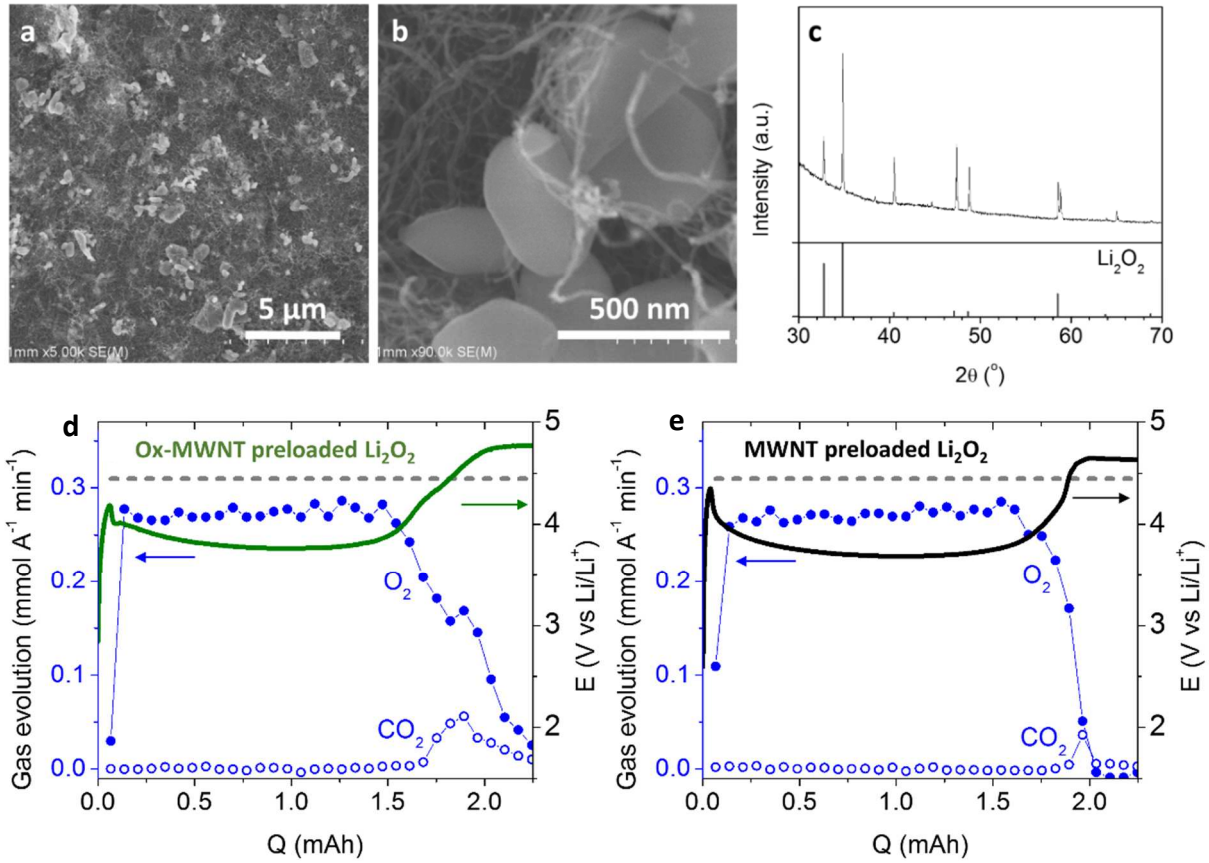

Figure 3.13 - Oxidation behavior of preloaded Li_2O_2 electrodes and gas analysis (a-b) SEM images of preloaded electrodes with different magnifications. The Li_2O_2 particle size is < 1 µm (c) XRD pattern of Li_2O_2 crystal in the preloaded electrode (top) and Li_2O_2 reference (JCPDS 09-0355). (d) Charge profiles of Ox-MWNT and () MWNT with preloaded Li_2O_2 particles and corresponding *in situ* gas analysis performed with 0.5 M $LiClO_4$/tetraglyme at 0.1 mA cm^{-2}. The dashed lines correspond to the 2 e^-/O_2 evolution rate.

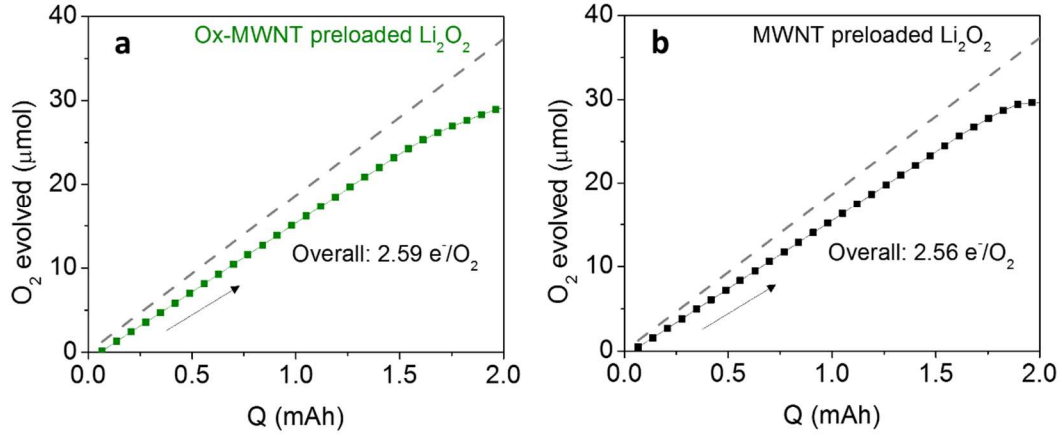

Figure 3.14 - Integral O_2 evolution plots of preloaded Li_2O_2 electrodes. (a) Ox-MWNT and (b) MWNT preloaded Li_2O_2 electrodes, giving overall values of 2.59 and 2.56 e^-/O_2, respectively. The dashed line indicates the ideal 2 e^-/O_2. The overall e^-/O_2 is determined by the integral O_2 evolved from 0 to 2 mAh, where the ideal case would equate to 37.3 μmol of O_2.

To further demonstrate the critical role of Li_2O_2 structure, we modulated the Li_2O_2 structure by tuning the concentration of oxygen functional groups in Ox-MWNT with heat treatments. To further correlate and understand the effect of O-functional groups for Ox-MWNT, temperature programmed desorption (TPD) measurements were conducted (**Figure 3.15a**). TPD provides information revealing the identity of surface functional groups based on their respective decomposition temperature ranges and the type of gas desorbed (CO, CO_2).[17,32,46] Typically in carbon materials, phenol, carbonyls, quinones and pyrone groups desorb as CO, while lactones and carboxyl groups desorb as CO_2 upon annealing. Carboxylic anhydrides are unique as they result in the release of both CO and CO_2.[17,46] TPD profile of the as-prepared Ox-MWNT (**Figure 3.15a**) shows significant CO_2 desorption up to 500 ^oC (~75.4% of total CO_2 desorbed by 1000 ^oC) coinciding with the elimination of carboxyl groups [17,32,46]. Accordingly, Ox-MWNT following annealing at 500 ^oC (denoted hereon as Ox-MWNT-500) exhibits a reduced atomic ratio O/C of 0.038 (**Figure 3.16a**) with featureless –COO– peak in the XPS C 1s and O 1s spectra (**Figure 3.15b** and **Figure 3.16b**).

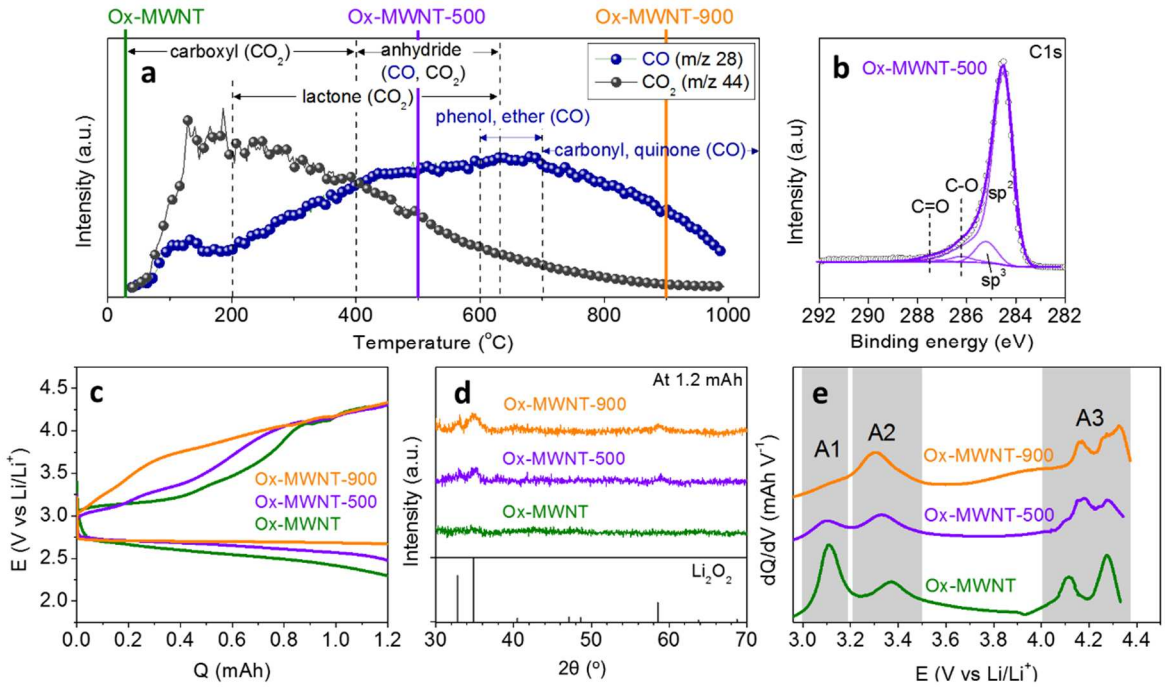

Figure 3.15- Influence of tuning oxygen functional groups in Ox-MWNT (a) Temperature programmed desorption (TPD) of Ox-MWNT with CO (m/z=28) and CO_2 (m/z=44) desorption and their assignment to oxygen functional groups.[17, 28, 32, 40] (b) XPS C 1s spectra of Ox-MWNT-500 (annealing at 500 °C) (c) DC-RC curves of Ox-MWNT, Ox-MWNT-500 and Ox-MWNT-900 at fixed capacity of 1.2 mAh in 0.5 M $LiClO_4$/tetraglyme with current density of 50 mA g^{-1}. (d) Corresponding XRD of electrodes following DC. (e) Differential capacity plots analyzed from galvanostatic RC (after DC to 2 V).

In Li–O_2 cells, Ox-MWNT-500 shows a more gradual decrease in DC potential than Ox-MWNT but is more prominent in comparison to Ox-MWNT-900 (**Figure 3.15c** and **Figure 3.16c–d**). Moreover, the subsequent RC profile also exhibits transitional behavior in between Ox-MWNT and Ox-MWNT-900, which is correlated with the degree of amorphousness of the Li_2O_2 (XRD, **Figure 3.15d**). The trend is illustrated in the differential capacity plots (Figure 7e) where lower oxidation potential is present for more amorphous Li_2O_2: The presence of *a*-Li_2O_2 shows the pronounced oxidation feature at ~3.1 V (labeled as A1 region) whereas more crystalline Li_2O_2 (denoted as *c*-Li_2O_2) requires higher potential of 3.3~3.4 V (labeled as A2 region). These both correspond to Li_2O_2 oxidation and leads to O_2

evolution (**Figure 3.17**), allowing us to delineate the decomposition of Li_2O_2 to different potentials according to Li_2O_2 structure. The facile decomposition of *a*-Li_2O_2 is presumably attributed to its significantly higher electronic and ionic conductivities (5.02×10^{-9} and 7.10×10^{-8} S c m^{-1}, respectively), providing a more conductive network than *c*-Li_2O_2 (~10^{-20} S cm^{-1} for both electronic and ionic conductivities).[47,48] The *a*-Li_2O_2 has abundant defects arising from Li vacancies that may initiate charge transport *via* polaron hopping [48-50]. In addition, these defects can promote topotactic delithiation at the initial stage of oxidation.

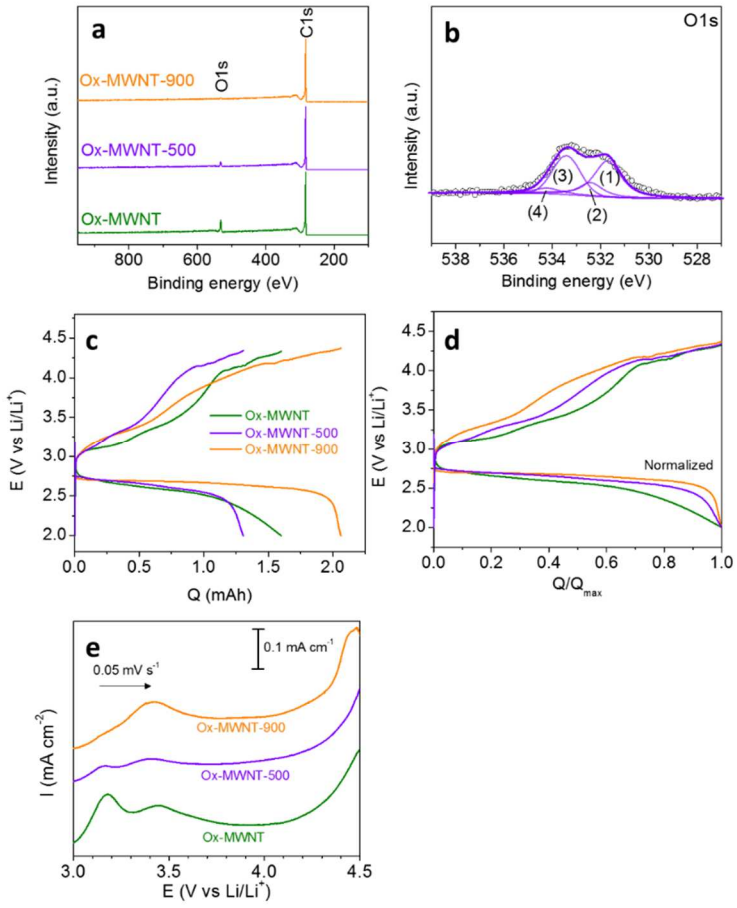

Figure 3.16 - Additional characterizations with Ox-MWNT-500 compared with Ox-MWNT and Ox-MWNT-900. (a-b) XPS of (a) wide scan for all three electrodes and (b) O 1s binding energy region of Ox-MWNT-500. The peak assignments in (b) are identical as those found in Figure S1. (c) DC-RC profiles comparing Ox-MWNT, Ox-MWNT-500 and Ox-MWNT-900 performed with 0.5 M $LiClO_4$ in tetraglyme at 50 mA g^{-1} to a cutoff potential of 2 V. (d) Normalized capacity from (c). (e) Anodic LSV at sweeping rate 0.05 mV s^{-1} after cathodic potential sweeping from 3 to 2 V

The delithiation of Li_2O_2 can produce LiO_2(sol) by the withdrawal of Li^+ ions ($Li_2O_2 \rightarrow x(Li^+ + e^-) + xLiO_2(sol) + (1–x)Li_2O_2$), which can then disproportionate ($2LiO_2(sol) \rightarrow Li_2O_2 + O_2$) [49,51]. It can be expected that facile delithiation occurs with *a*-Li_2O_2 possessing a lower barrier for charge transport. This is supported by the detection of LiO_2(sol) during oxidation from RRDE measurements. With the ring current set at the identical condition as **Figure 3.9** (at 3.3 V_{ring} and rotation of 900 rpm), the anodic LSV following reduction (**Figure 3.18**) shows the presence of ring current at low potentials for Li_2O_2 oxidation, which disappears at higher potentials for all samples (containing different Li_2O_2 structures), indicating the allowance of delithiation only at the initial stage of oxidation. Moreover, the peak potential of ring is closely correlated with the oxidation potential of Li_2O_2 on disk: Ox-MWNT shows the lowest potential of ~3.27 V whereas the ring response for G-MWNT is 100 mV higher (~3.37 V). These RRDE results support the facile initial decomposition of *a*-Li_2O_2 driven by preferential delithiation

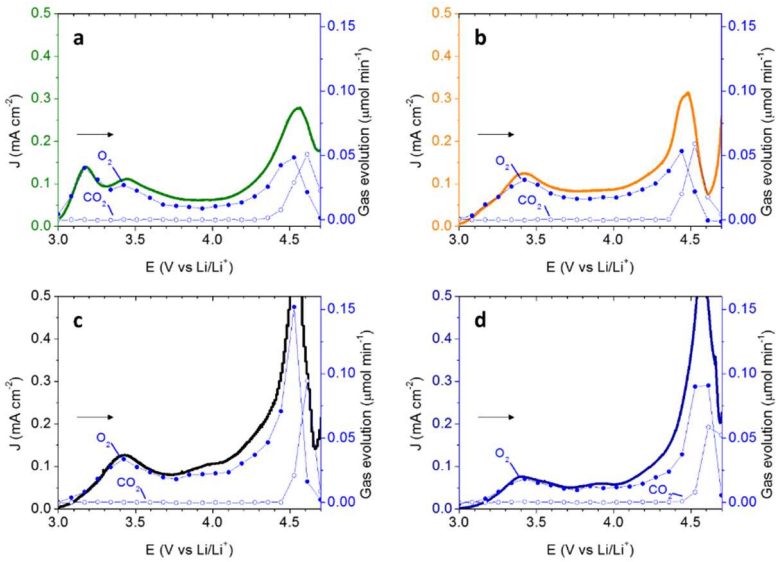

Figure 3.17 - Anodic LSV coupled with *in situ* OEMS for (a) Ox-MWNT, (b) Ox-MWNT-900, (c) MWNT and (d) G-MWNT using 0.5M $LiClO_4$/tetraglyme at a sweeping rate of 0.05 mV s^{-1}. All of the anodic LSVs were carried out after a cathodic sweep from 3 to 2 V.

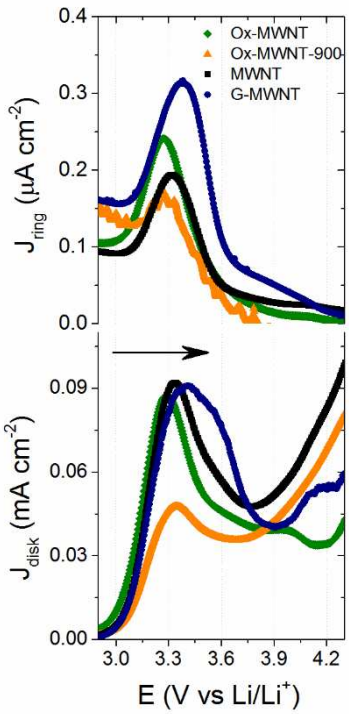

Figure 3.18 - Anodic (oxidative) LSV with RRDE (bottom) disk and (top) ring current response (ring at potential of 3.3 V_{ring}) at a scan rate of 2 mV s^{-1} and rotation rate of 900 rpm in 0.5 M $LiClO_4$/tetraglyme. The scan was performed after the reduction sweep of 3 to 2 V.

3.3.5 - Side reactions over 3.5 V for RC

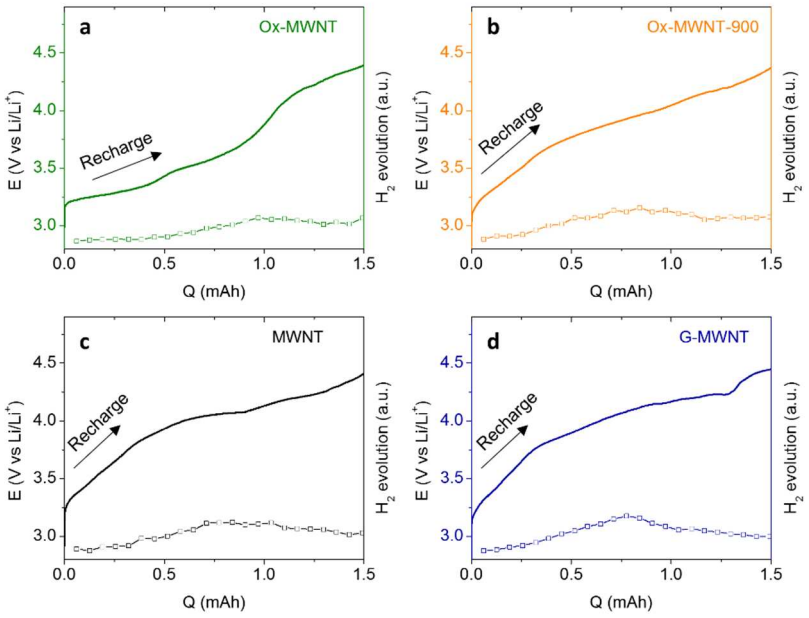

Figure 3.19 - *In situ* H_2 evolution profiles for (a) Ox-MWNT, (b) Ox-MWNT-900, (c) MWNT and (d) G-MWNT, respectively, with comparable electrode mass of 2 mg in 0.5 M $LiClO_4$/tetraglyme at current density of 50 mA g^{-1}. These measurements were performed in conjunction with the data in Figure 5.

At over 3.5 V, Li_2O_2 decomposition is significantly influenced by parasitic side reactions. The O_2 evolution rate is reduced for all electrodes (**Figure 3.15**), with the overall average of 3.25~3.45 e^-/O_2 (**Table 3.2**). This is notably higher than the first 50% of RC (2.3~2.8 e^-/O_2), reflecting the greater contribution of side reactions at higher potentials. The total O_2 evolved are comparable for all carbon nanotube electrodes at ~60% (relative to O_2 consumed, **Table 3.2**). These values are lower than the total Li_2O_2 yields (72~83%, **Table 3.2**) measured from titration of the electrode together with separator after DC,[38], [28] where

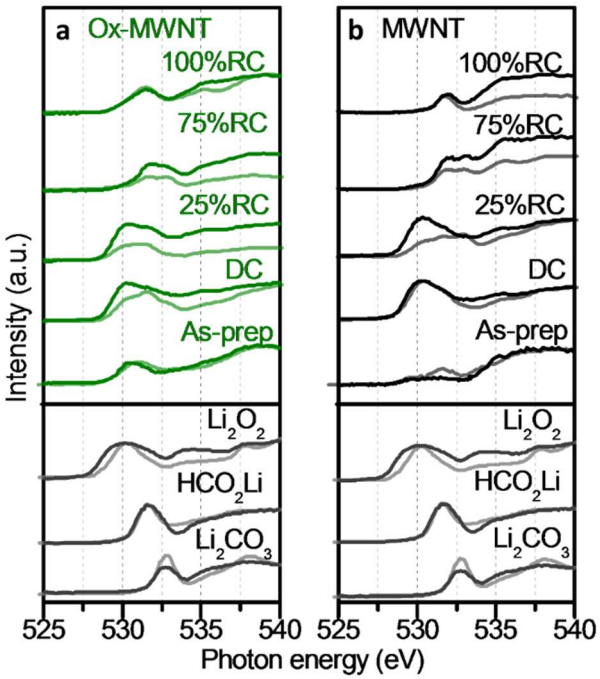

Figure 3.20 - O K-edge XANES (a) Ox-MWNT (green, left panel) and (b) MWNT (black, right panel) with (light color) surface sensitive total electron yield (TEY) and (dark color) bulk-sensitive partial fluorescence yield (PFY) modes. The electrodes were DC to the fixed capacity of 1.2 mAh and then RC to 25% and 75% and 100% RC (to equivalent capacity) at current rate of 50 mA g^{-1}. Reference spectra (gray, bottom) are Li_2O_2, Li_2CO_3 and HCO_2Li.

the more disordered electrodes have lower yields (72~73% for Ox-MWNT and Ox-MWNT-900 versus 78% for MWNT and 83% for G-MWNT, **Table 3.2**). This suggests (1) larger amount of isolated Li_2O_2 present in the separator with more ordered carbon electrodes due to solvation-based process and (2) occurrence of unintended reactions transforming Li_2O_2 to

side products during RC. That is, the Li_2O_2, present on separator and occurrence of side reactions, are not involved in O_2 evolution.

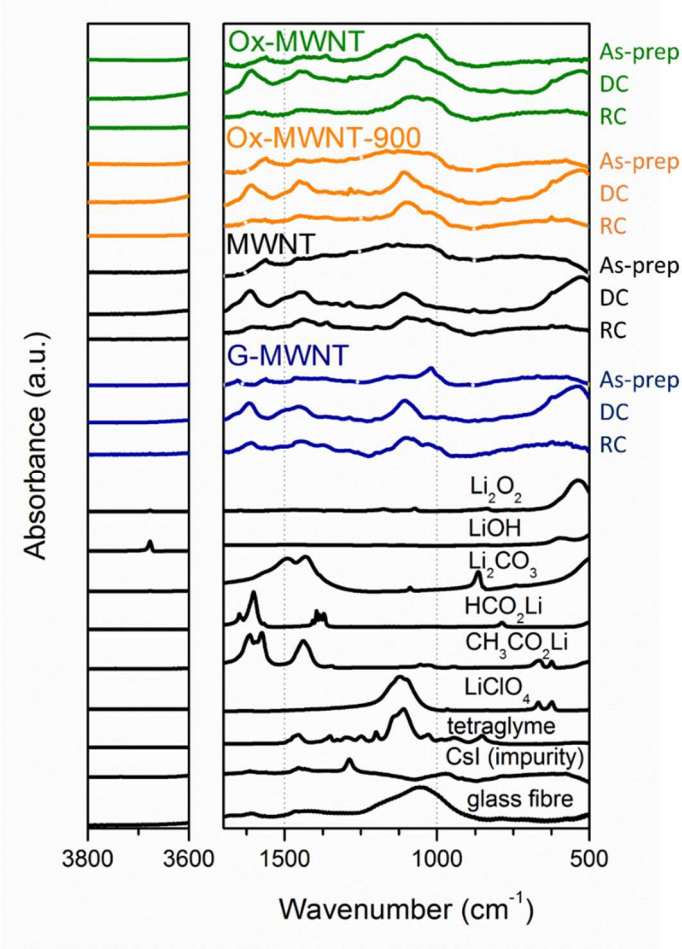

Figure 3.21 - Fournier transform infrared (FTIR) spectra of as-prepared (As-prep), DC (to 2 V) and RC (equivalent to DC capacity) electrodes and reference powders (bottom) in transmission mode. The predominant presence of Li_2O_2 (ν(Li-O) assigned to the absorption peaks at 530 cm^{-1}) can be identified for all electrodes. In addition, typical side products of lithium formate (HCO_2Li, $\nu(CO_2^-)$ at ~1370 cm^{-1}), lithium acetate (CH_3CO_2Li, $\nu(CO_2^-)$ at ~1615 cm^{-1}) are present after DC.

The RC related side reactions were investigated by gas and chemical analyses. There are low degrees of H_2 evolution from 3.5 V (**Figure 3.19**) and notable CO_2 evolution over 4.2 V (**Figure 3.12c**). The O K-edge XANES spectra show pronounced formate (HCO_2Li, 531.7 eV) and Li_2CO_3-associated features (532.7 eV) during RC (**Figure 3.20**): The carboxylate-related signal is observed after DC (more significant for Ox-MWNT) and throughout the RC process for both Ox-MWNT and MWNT, which is further corroborated from the Fourier

transform infrared (FTIR) spectra (**Figure 3.21**). In contrast, the carbonate-related feature appears during RC, and can only be observed at 25% RC for MWNT in the TEY (surface-sensitive total electron yield) mode, and is apparent at 75% RC for both MWNT and Ox-MWNT in the TEY and PFY (bulk-sensitive partial fluorescence yield) modes. After 100% RC (to equivalent DC capacity) the carbonate signal almost disappears for both electrodes (see below). Considering the RC potential according to the depth of RC, lithium carbonates formed are present above 3.75 V at the Li_2O_2 surface and remains prominent up to 4.2 V, before being eliminated. The carbonate decomposition occurs upon satisfying the conditions that (1) Li_2O_2 is mostly decomposed, (2) the carbonates are in contact with the electrode surface and (3) the potential is over 4.2 V, as shown in *in situ* gas analysis results (**Figure 3.12, 3.13** and **3.17**).

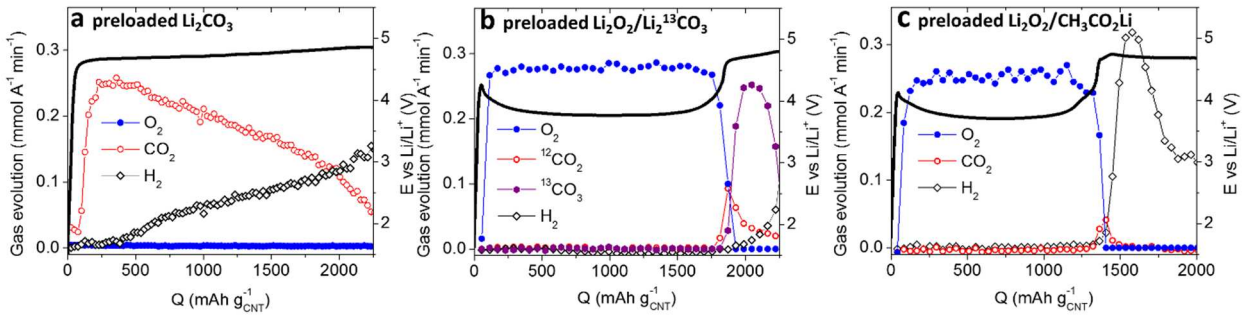

Figure 3.22 - *In situ* OEMS analysis for MWNT electrodes preloaded with (a) Li_2CO_3 (b) mixture of Li_2O_2 and $Li_2{}^{13}CO_3$ (^{13}C isotope labeled) and (c) mixture of Li_2O_2 and CH_3CO_2Li. The Li_2O_2 to $Li_2{}^{13}CO_3$/ CH_3CO_2Li mass ratio is 4:1. The oxidations were performed in 0.5 M LiTFSI/tetraglyme at current rate 0.1 mA cm^{-1} (0.114 mA). Unlike quantitative measurements for O_2 and CO_2 evolution, the H_2 evolution rates are qualitatively compared.

The Li_2CO_3 predominantly evolves CO_2 during decomposition (onset at 4.5 V). The mixture of Li_2O_2/$Li_2{}^{13}CO_3$ shows the occurrence of Li_2CO_3 decomposition just after termination of Li_2O_2 decomposition (O_2 evolution). In addition, the evolution of $^{12}CO_2$ indicates the formation of $Li_2{}^{12}CO_3$ originating from electrolyte and carbon electrode degradation,[10] which is decoupled from concurrent $^{13}CO_2$ evolution. Unlike Li_2O_2 and Li_2CO_3, the lithium carboxylates do not produce CO_2 or O_2 during oxidation process. Instead, the mixture of Li_2O_2/CH_3CO_2Li shows a sharp H_2 evolution peak after the complete Li_2O_2 decomposition. The sudden increase of H_2 evolution feature is distinct from standard electrolyte oxidation showing the plateau of H_2 evolution (like the feature observed over 1750 mAh g^{-1} in (c)), suggesting the contribution of CH_3CO_2Li oxidation for other side reactions.

To further clarify the gas evolution trends of side products, additional preloaded analysis tests were carried out. The oxidation of preloaded Li_2CO_3 produces significant CO_2 at potentials > 4.5V, but with no O_2 evolution (**Figure 3.22a**). Furthermore, the mixture of preloaded Li_2O_2 and isotope labeled $Li_2{}^{13}CO_3$ results in both $^{13}CO_2$ and $^{12}CO_2$ evolution, commencing when Li_2O_2 is near completion and is signified with the switching (increase) in potential (**Figure 3.22b**). The small amount of $^{12}CO_2$ evolution reflects the formation of side products ($Li_2{}^{12}CO_3$) via degradation of the electrolyte and carbon electrode during Li_2O_2 decomposition,[10] which is in good agreement with the CO_2 evolution trend following Li_2O_2 oxidation, in the case with only preloaded Li_2O_2 (**Figure 3.13d-e**). On the basis of this knowledge, the increasing CO_2 evolution rate with steeply decreasing O_2 occurring in all electrodes at the end of RC process can be understood (**Figure 3.12**). It is noted that lithium carboxylates do not produce either CO_2 or O_2, but results in the sharp increase of H_2 after the decomposition of Li_2O_2 (preloaded Li_2O_2/CH_3CO_2Li with MWNT, **Figure 3.22c**). This indicates the presence of residual carboxylates that may be involved in other side reactions.

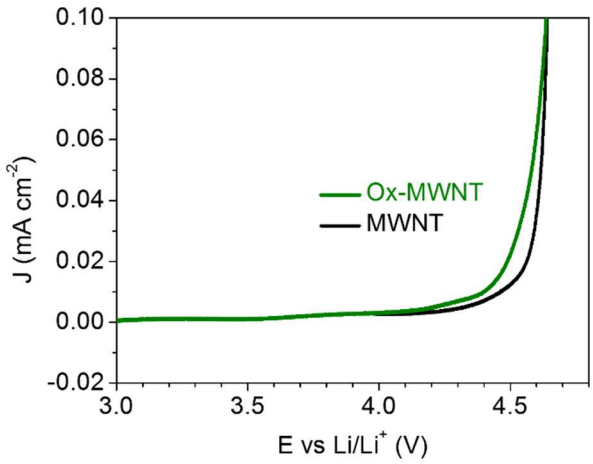

Figure 3.23 - Anodic LSVs of blank Ox-MWNT and MWNT electrodes (without prior reduction process) under Ar in 0.5 M $LiClO_4$/tetraglyme and at sweep rate of 0.05 mV s^{-1}, showing appearance of Ox-MWNT oxidation at lower potential than MWNT.

Along with side reactions occurring at the Li_2O_2/electrolyte interface, the effect of oxygen functional groups on the Ox-MWNT surface is intriguing. The stability of oxygen functional groups can be tested by anodic LSV in Ar using blank electrodes (without prior DC, **Figure 3.23**). The Ox-MWNT shows lower oxidation potential compared to MWNT, implying that oxygen functional groups on the bare surface degrade and can facilitate the oxidation of tetraglyme (at over 4.1 V). However, once Li_2O_2 is deposited, the oxygen functional groups underneath have strong interaction with Li_2O_2. This is shown from the Li_2O_2 particle-preloaded Ox-MWNT during overcharge (**Figure 3.13d-e**), where O_2 evolution continues together with CO_2 evolution even at over 4.75 V. The difficulty in the complete elimination of Li_2O_2 and side products leads to the oxygen functional groups being covered and deactivated at the end of Li_2O_2 oxidation.

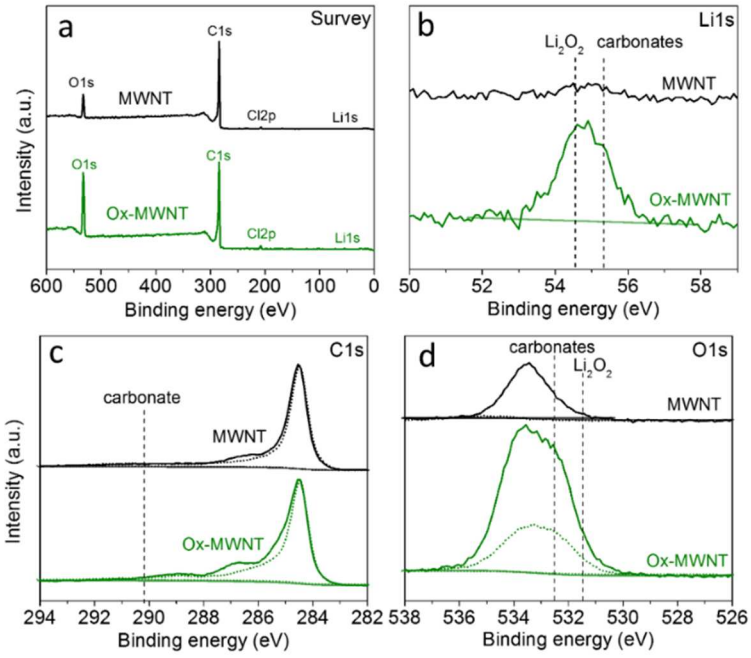

Figure 3.24 - XPS of Ox-MWNT and MWNT electrodes following 100% RC (a) wide scan (b) Li 1s (c) C 1s and (d) O 1s binding energy regions. The dotted spectra in C 1s and O 1s show the as-prepared electrodes for comparison. The dashed vertical lines denote the peak assignments of Li_2O_2 (Li 1s: 54.5 eV, O 1s: 531.5), carbonates (Li 1s: 55.3 eV, O 1s: 532.5 eV C 1s: 290.2 eV).[6, 13] The DC capacity was fixed at 1.2 mAh with RC to the equivalent capacity.

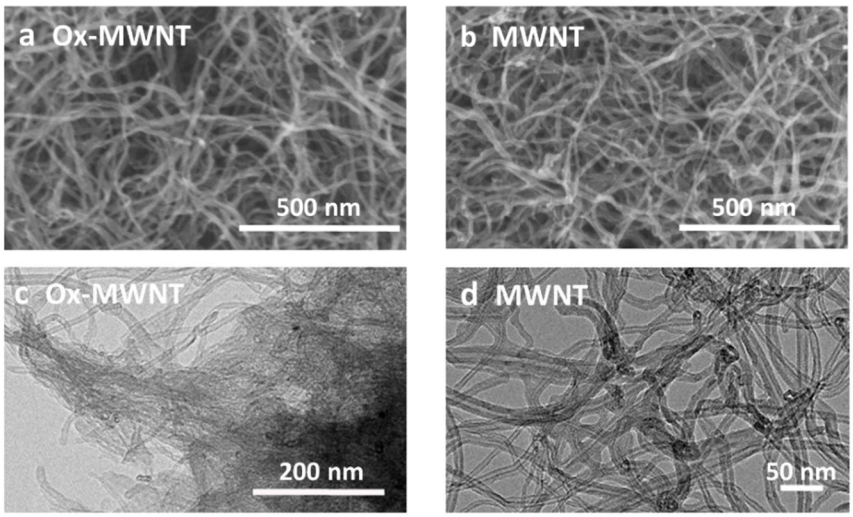

Figure 3.25 - (a-b) SEM and (c-d) TEM images of Ox-MWNT and MWNT electrodes after 100% RC (following DC to 1.2 mAh). The residual products that thinly cover Ox-MWNT are observed from TEM whereas SEM images with lower magnification do not show this feature.

In the case of electrochemically formed Li_2O_2 on Ox-MWNT, where almost all the oxygen functional groups on the electrode surface are covered with *a*-Li_2O_2 film, the effect of oxygen functional groups/Li_2O_2 interaction is more prominent. Towards the end of RC, there is lower throughput of O_2 evolution (downward step in O_2 evolution rate) compared to the other electrodes (**Figure 3.12**) and suggests the presence of residual and inactive Li_2O_2 that is anchored to the oxygen functional groups. This is confirmed from surface-sensitive XPS of the RC electrodes. The Li_2O_2 and lithium carbonates are present for Ox-MWNT in Li 1s and O 1s region (atomic ratio Li/C of 0.086) in contrast to the MWNT (**Figure 3.24**). TEM

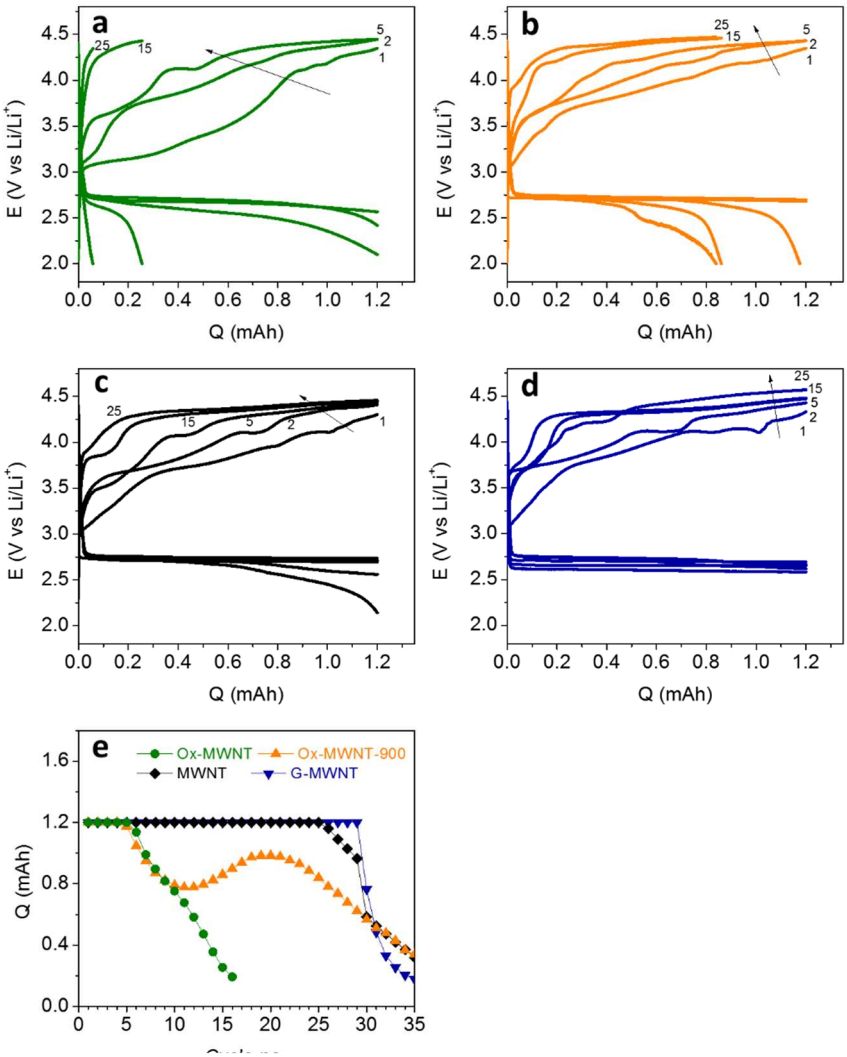

Figure 3.26 - Galvanostatic cycling with DC-RC profiles of (a) Ox-MWNT, (b) Ox-MWNT-900, (c) MWNT, and (d) G-MWNT with electrode mass of 1.2 mg. The cycling was performed in 0.5 M $LiClO_4$/tetraglyme at current density of 50 mA g^{-1}, and fixed capacity of 1.2 mAh. (e) Comparison of capacity retention.

images further supports the presence of residual products thinly covering the Ox-MWNT surface, which is not noticeable on the MWNT surface (**Figure 3.25**). We note that the amount of residual lithium compounds is small: O K-edge XANES shows small residual features of carboxylates and carbonates after 100% RC (**Figure 3.24**) and SEM analysis show no obvious residual features (**Figure 3.25**). However, the effect of these side products and degraded oxygen functional groups on the carbon nanotube surface is significant: The deactivated oxygen functional groups by the residual lithium compounds are ceases to function during the second cycled DC-RC process, which results in a rapid rise in RC

potential (**Figure 3.26**). The deactivated surface presumably promotes the accumulation of side products and leads to lower capacity retention during cycling (**Figure 3.26**). On the contrary the ordered carbon electrodes act as a stable electrode with more complete decomposition of lithium compounds upon cycling **(Figure 3.26**), although some surface degradation is also observed from the high RC potential as demonstrated by the increased O/C atomic ratio at 0.099 (O 1s peak increase in **Figure 3.24d**) after the first cycle for MWNT. These results show the critical effect of carbon electrode surfaces for stability at high potential and cycling. The defect-less and highly ordered carbon electrode is required to improve stability of electrode while disordered sites such as defective edge and functional moiety connecting with carbon backbone via covalent bonding can exacerbate side-reactions. This result affirms the necessity of intensive efforts to reduce side reactions during the DC and RC process to attain reversible Li-O_2 electrochemistry. The coating of carbon electrode surface with thin and protective layer would be one promising approach, which is currently under investigation.

3.4 - Conclusion

We have demonstrated that tuning the surface chemistry of carbon nanotube-based electrodes leads to drastically different Li-O_2 electrochemical behaviors. New insights are gained into the influence towards DC capacity and RC overpotential. The presence of oxygen functional groups on the carbon nanotube surfaces leads to the predominant surface-adsorption-based Li_2O_2 nucleation and growth. The rapid passivation of Li_2O_2 results in formation of amorphous Li_2O_2 with lower DC capacity than in comparison to carbon electrodes with more ordered structures, while this is still significantly superior to that from carbon-free and heavy inorganic electrodes.[21,52] More importantly, the resulting amorphous Li_2O_2 facilely decomposes rendering low overpotential for RC. On the other hand,

the highly uniform and graphitized carbon nanotubes lead to the formation of aggregated and crystalline Li_2O_2 via solvation-based process, which enables for far larger DC capacities but also larger RC potential. The further tuning of oxygen moieties allowed for the engineering of the resulting Li_2O_2 structure and delineated the origin of the wide range of Li_2O_2 decomposition potentials, which has implications in that the Li_2O_2 structure formed on DC directly influences the RC overpotential. Our findings clearly identify the critical role of carbon surface characteristics to Li–O_2 cell performance by controlling oxygen functional groups, defective edges and graphitization of carbon nanotubes, and demonstrate the strategy for facile decomposition of Li_2O_2. This study also has broader implications that can be applied to guide rational design strategies for carbonaceous electrodes.

Chapter 4

Elucidating the influence of metal and metal oxide promoters for oxygen evolution in Li-O_2 batteries

Chapter 4 contains *unpublished* work.

4.1 - Introduction

The intense focus on post Li-ion batteries with ultra-high energy densities is generating enormous interest in aprotic lithium oxygen (Li-O_2) batteries [1,2]. The theoretical specific energy of Li-O_2 batteries is extremely attractive (~3.5 kWh/kg), operating with an overall $2e^-$ transfer oxygen-peroxide (O_2/O_2^{2-}) redox couple *via* $2Li^+ + O_2 + 2e^- \leftrightarrow Li_2O_2$ (E^o = 2.96 V vs Li/Li^+), forming insulting lithium peroxide (Li_2O_2) as the discharge product.[3,4] In reality however, the actual performance of Li-O_2 cells has thus far been underwhelming,[1] with notable challenges associated with poor cycleability (<100 cycles) and large overpotentials (η >1 V), observed during recharge.[5,6]

Typically with carbon-based electrodes, discharge occurs at ~2.6-2.7 V (η <400 mV), however, the voltage gap between discharge (DC) and recharge (RC) routinely results in low round trip efficiencies of ~65%.[5] The origin of the large RC overpotential has been attributed to (1) the low conductivity of the wide-bandgap Li_2O_2 resulting in sluggish charge transport and (2) side products consisting of lithium carbonate (Li_2CO_3 and lithium alkyl carbonates) and lithium carboxylates ($LiCO_2R$, R is hydrogen or alkyl) from parasitic side reactions due to electrolyte and electrode instabilities with LiO_2 and Li_2O_2.[6-9] These highly insulating side products at the Li_2O_2/electrode and Li_2O_2/electrolyte interfaces is presumed to be detrimental and consequently lead to the increase in RC potential.[3,10,11] Numerous endeavours have been directed toward reducing the large RC overpotential including the

notable use nanostructured metal and metal oxides (denoted as M(O)), largely owing to its established use in aqueous oxygen evolution (OER) electrocatalysis.[12]

It has been asserted that the conventional sense of electrocatalysis is not applicable to the Li-O_2 electrochemistry due to the formation of insoluble Li_2O_2, which precludes any turnover of potential active sites as the M(O) surfaces becomes passivated (particularly during RC), which further questions the role of M(O) "catalysts".[13] Nevertheless, a significant number of reports have indeed shown reduced RC overpotentials along with the adoption of the term "promoter" reflecting its differentiation from conventional electrocatalysis.[12,14] More importantly, as parasitic side reactions are prevalent in the Li-O_2 field,[9] the reduction in RC potential should not be taken as evidence that the desired reaction (Li_2O_2 electrooxidation) is occurring, namely, it is highly possible that reversibility can become compromised when M(O) promoters are employed.[13] For instance, there is the assertion in literature that if the RC potential is maintained below 4 V, reversibility can be improved with side reactions reduced, or even avoided.[15,16] We will show that this is not the case, even with Ru NPs, which is widely employed in the Li-O_2 battery field. More notably, the comparison amongst the literature is not feasible with respect to the true OER activity (towards Li_2O_2 oxidation), due to different experimental conditions, namely, Li-O_2 cell tests amongst the literature are conducted with different promoters, mass loading, size, carbon, total electrode mass, and test conditions (e.g. current rate and cut-off potential).

The aforementioned reasons and the continued emphasis on the utilization of M(O) promoters have prompted us to elucidate (1) the efficacy towards the reduction in RC overpotential (2) the true and predominant processes (both positive and negative) occurring in M(O) containing Li-O_2 cells, and lastly, (3) the role and origin of M(O)s to the observed behavior. We have synthesized Au, Pt, Pd, Ru and Co_3O_4 NPs on multi-walled carbon nanotubes (denoted as M(O)/CNT) and have benchmarked the M(O) oxygen evolution

reaction (OER) activity together with complementary chemical analysis and quantitative evaluation of reversibility. In this work, we have used the term “promoter” to differentiate between conventional electrocatalysis. We have utilized the M(O) promoter loading of ~40 wt.% (relative to mass of CNT) and with NP size (<10 nm) allows for the evaluation of the intrinsic influence. Our findings indicate that with the exception of Au/CNT, the RC overpotential is notably lowered with M(O)/CNTs. However, we show that there is no improvement with respect to reversibility which consistently results in ~60% O_2 recovery. Moreover, the M(O)/CNT (aside from Au/CNT) reduce the potential for electrolyte oxidation. We show that there is no correlation between RC overpotential and cycleability, where the ability to avoid side reactions or effectively decompose side products becomes important. Lastly, we further extend the study to connect the effect of M(O) NP size, where we show that M(O) NPs below 10 nm show a relatively weak correlation with size and OER activity. In all our findings show that M(O) promoters appear to mask the underlying issue of reversibility in Li-O_2 batteries and affirm the necessity in identifying electrolytes that promote reversible Li-O_2 electrochemistry.

4.2 - Experimental

4.2.1 - Synthesis of M(O)/CNTs

The multi-walled carbon nanotubes (CNTs) used throughout the study have an outer diameter of 10-20 nm (Sigma Aldrich). The corresponding M(O)/CNTs were synthesized as follows:

Au NPs/CNT

CNT-supported Au NPs (diameter (*d*) = ~8 nm) were synthesized *via* a modified procedure described by Murphy *et al.*[17-19] by dispersing 0.1 g CNT and 0.397 g trisodium citrate ($Na_3C_6H_5O_7 \cdot 2H_2O$) into 480 mL of water followed by the addition of 0.142 g of $HAuCl_4$ in 20 mL of water. Next, 0.042 g of $NaBH_4$ in 10 mL of water was rapidly added under

vigorous stirring. The Au/CNTs thoroughly washed and collected by repeated centrifugation with water and ethanol followed by drying in a vacuum oven at 45 ^{o}C overnight.

CNT-supported Au NPs (diameter (*d*) = ~6 nm) with an 80 mL aqueous solution containing ~0.17 mM gold(III) chloride trihydrate ($HAuCl_4 \cdot 3H_2O$, ≥99.9% trace metals basis, Sigma-Aldrich) and 0.41 mM trisodium citrate ($Na_3C_6H_5O_7 \cdot 2H_2O$) was prepared. Trisodium citrate acts as a capping agent and thus restricts particle growth. 50 mg CNT powder was added to the above solution and dispersed by tip sonication in ice-bath for 10 mins. Next, 0.5 mL of a 0.1 M $NaBH_4$ solution was added at once into the suspension under constant stirring. Stirring was continued for another 20 mins in ice-bath. The Au/CNT was then collected by centrifugation and washed with water and ethanol for more than five times. The Au/CNT was dried in vacuum oven at 45 °C.

Pt NPs/CNT

CNT-supported Pt NPs (*d* = ~5 nm) were synthesized with a modified method from the Au NPs with sodium borohydride ($NaBH_4$) as the reducing agent and sodium citrate ($Na_3C_6H_5O_7 \cdot 2H_2O$) as a stabilizing agent.[17,18] To obtain Pt NPs with size of ~5 nm, 75 mg of chloroplatinic acid hexahydrate $H_2PtCl_6 \cdot 6H_2O$, Sigma-Aldrich) was dissolved with 128 mg of $Na_3C_6H_5O_7 \cdot 2H_2O$ in 40 mL water and 0.45 mL of 1 M NaOH. This was followed by the addition of 30 mg of CNT. After tip sonication and stirring, 1.6 mL of 0.1 M $NaBH_4$ solution was added into the suspension under vigorous stirring at 25 °C. After stirring for 6 h, the precipitate was collected by centrifugation. The mixture was washed repeatedly with water and ethanol and dried overnight in a vacuum oven at 45 °C.

Pd NPs/CNT

CNT-supported Pd NPs (*d* = ~5-6 nm) were synthesized with sodium borohydride ($NaBH_4$) as a reducing agent and sodium citrate ($Na_3C_6H_5O_7 \cdot 2H_2O$) as a stabilizing agent.[20] For controlling the particle size of Pd NPs to be ~5nm, the ratio of sodium citrate to palladium

chloride is adjusted to be 3:1. The detailed synthetic procedure is as follows: 40 mg $PdCl_2$ (~0.22 mmol, dissolved in 0.1 M HCl) solution and 500 mg sodium citrate (1.7 mmol) were dissolved into 120 ml water, then 36 mg CNT was added and tip sonicated for 10 mins in ice-bath. 5 ml of 0.1 M $NaBH_4$ solution was added into the suspension dropwise under vigorous stirring at 25 °C. After the suspension was stirred for 4 h, the black precipitate was collected by centrifugation, washed with water and ethanol repeatedly, and dried overnight in a vacuum oven at 45 °C.

The Pd/CNTs with size ~3-4 nm was synthesized in similar fashion except the ratio of sodium citrate to PdCl2 was 8:1 and the reduction temperature was 0 ^oC. Lastly, the Pd/CNT with size ~17 nm was obtained by utilizing bubbling Ar/H_2 (1:1) gas into the 5nm Pd/CNT precursor solution for 12 h at 25 ^oC.

Ru NPs/CNT

The Ru NPs (*d* = ~1.5 nm) colloidal solution was synthesized by immersing 365 mg $RuCl_3 \cdot nH_2O$ in 20 mL of ethylene glycol. The pH was subsequently adjusted to ~11 by adding 10 mL of 0.1 M NaOH in ethylene glycol. After stirring for 30 mins, the mixture was heated to 200 ^oC under inert N_2 atmosphere for 4 hours. To synthesize the Ru/CNTs, 45 mg of CNTs was dispersed in 80 mL of ethanol and tip sonicated for 10 mins. Next while being stirred, 12 mL of the Ru colloidal solution was added after which the pH was adjusted to ~5 by the addition of 0.1 M HCl followed by 6 hours of stirring. Afterwards, the mixture was thoroughly washed with ethanol and acetone by centrifugation before drying inside a vacuum oven at 105 ^oC.

CNT-supported Ru NPs (*d* = ~5 nm) were synthesized via the classical ‘polyol’ method[21] by reduction of ruthenium(III) chloride ($RuCl_3$, Ru content 45-55%, Sigma-Aldrich) in a liquid polyol. $RuCl_3$ and sodium acetate (CH_3CO_2Na, anhydrous, ≥99.9%, Sigma-Aldrich) were dissolved in 100 ml of ethylene glycol at 80 °C, forming a dark red transparent solution.

Ru particle size is adjusted by the concentration of acetate salt. The solution was refluxed at 210 °C for 3 hours under Ar atmosphere with Ar gas flow rate at ~20 ml min^{-1}. 50 mg CNT was dispersed in 100 ml isopropanol (IPA) by tip sonification for 10 mins. Ru polyol colloidal solution was then added to this CNT/IPA suspension under vigorous stirring. After stirring at constant rate at room temperature (25 °C). The Ru/CNT was collected by centrifugation, and washed by water and ethanol repeatedly. At last, the Ru/CNT was dried in vacuum oven at 45 °C.

Co_3O_4 NPs/CNT

Co_3O_4 NPs (d = 8-9 nm) were synthesized by slightly modifying the procedure reported earlier.[22] For the actual synthesis of Co_3O_4 nanoparticles, 0.3 g of cobalt acetate tetrahydrate ($Co(C_2H_5O_2)_2 \cdot 4H_2O$, 99%, Wako) was dissolved in 30.0 mL de-ionized water and this solution was added to 2 mL of 25% (v/v) aqueous NH_3 under vigorous stirring at 298 K. After 20 min, 100 μL of H_2O_2 solution was added as an oxidizing agent to ensure complete oxidation of Co^{2+} to Co^{3+}. The mixture was stirred for another 12 h at 298 K and the Co_3O_4 nanoparticles were collected by centrifugation followed by drying at 353 K. The Co_3O_4 nanoparticles were then mixed with CNT to make the loading of ~40%. The mixture was ground in a mortar and pestle, dispersed in isopropanol and ultrasonicated in a tip sonicator for 10 min. The slurry was then used to prepare freestanding electrodes as described in the next section.

Preparation of binder-free electrodes

Binder-free electrodes were prepared by adding pristine CNTs, metal/CNTs, or metal oxide/CNTs and dispersing in isopropanol (Wako) with the use of a bath sonicator for 10 min, followed by vacuum filtration through glass fibre (GF/C, Whatman) filter. After air-drying, individual electrode disks with 12 mm diameter were cut. The attached glass fibre was typically left with the electrode and used as part of the separator during cell assembly.

The electrodes were subsequently dried at 120ºC in a Büchi glass vacuum oven (B-585) overnight under vacuum prior to transfer into the Ar-filled glovebox without exposure to air. Cell assembly was carried out as described in Chapter 2.

4.2.2 - Characterisations

To compare with the pristine CNT electrode, all capacities and current density are normalized to the mass of CNT (1.2 mg). For the electrochemical testing, two-electrode cells were utilized as described in chapter 2 and 3. This study utilizes *in situ* on-line electrochemical mass spectrometry (OEMS), which is described in detail in chapter 2 and 3 and **Appendix A**. For the OEMS measurements, involved DC and RC to the fixed capacity of 1000 mAh g^{-1}_{CNT} (1.2 mAh). The XANES analysis were conducted as part of the collaboration with Ritsumeikan University, and were performed at BL-3 or BL-11 (soft X-ray beamline). The XPS measurements (PHI ESCA 5400MC) were conducted with monochromatized Al-Kα (1486.6 eV) X-ray source. The pass energy was 71.55 eV (wide scan) and 35.75 eV (individual narrow scan). The samples for XANES and XPS were dried in vacuum at 80 ºC before inserting into a transfer vessel inside a glove box, which permitted transfer into the XANES and XPS chambers without exposure to air.The SEM and FTIR characterisations were performed in an identical manner as described in chapter 3.

4.3 Results and discussion

Metal and metal oxide (Au, Pt, Pd, Ru and Co_3O_4) NPs were incorporated onto CNTs (denoted as M(O)/CNT) to form binder-free electrodes as shown in **Figure 4.1**. The M(O) loading was kept at ~40 wt.% (**Figure 4.1**, TGA) with respect to CNT mass of 1.2 mg. The M(O)/CNTs were prepared without chemical oxidation or functionalization of the CNT surfaces, eliminating the concerns of the influence of oxygen functional groups.[23] Transmission electron microscopy (TEM) shows that the Au and Co_3O_4 NPs are ~10 nm with

Pt and Pd NPs at ~5-6 nm and Ru NPs at 1.5 nm in size with x-ray diffraction (XRD, **Figure 1** and **Table 4.1**) confirming the presence of the M(O)/CNTs.

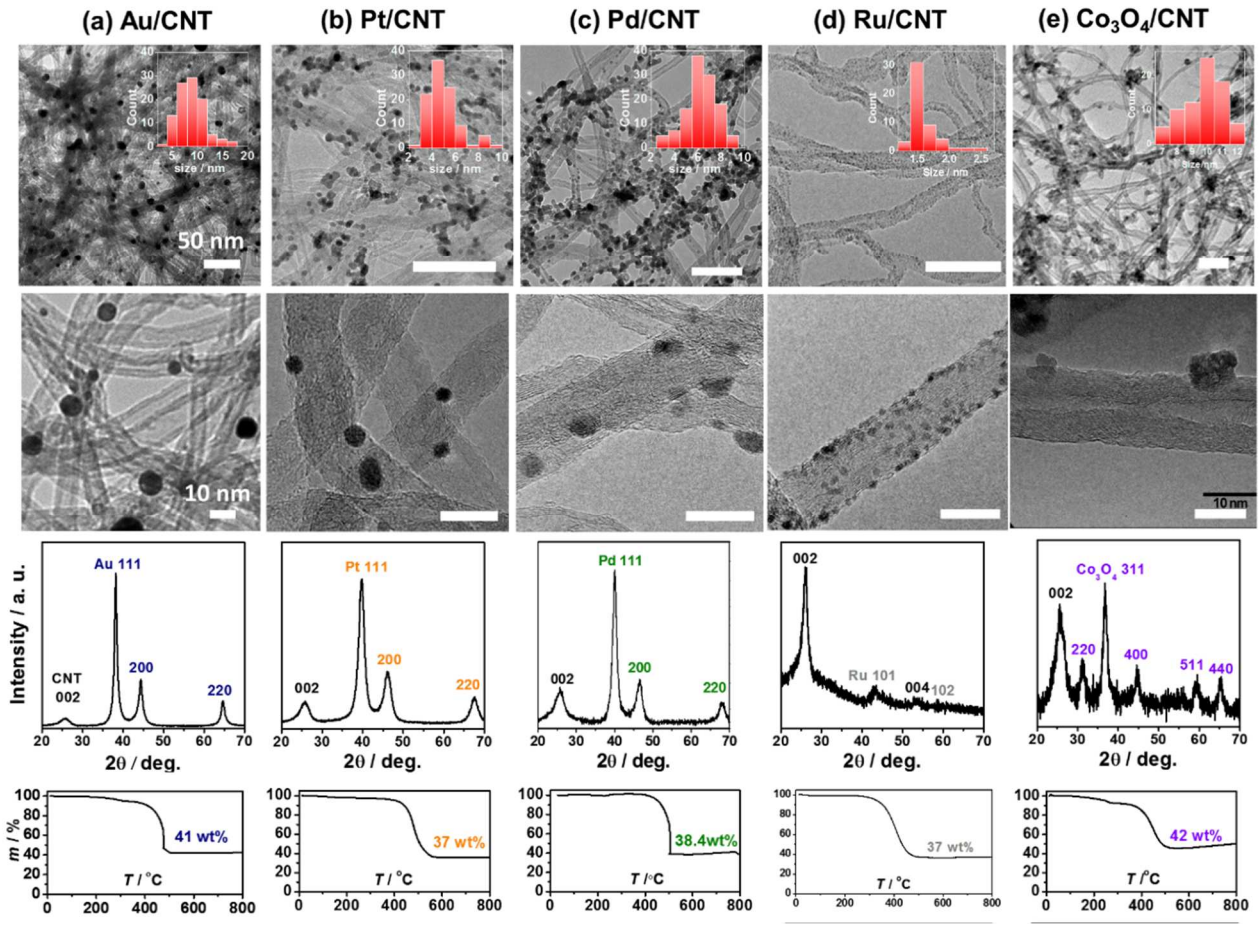

Figure 4.1 – Transmission electron micrographs (TEM), X-ray diffractograms (XRD) and thermogravimetric analysis (TGA) of as-prepared M(O)/CNTs with (a) Au/CNT, (b) Pt/CNT, (c) Pd/CNT, (d) Ru/CNT and (e) Co_3O_4/CNT. The scale bars indicate (top) 50 nm for the lower magnification TEM images and (bottom) 10 nm for the higher magnification TEM images. The inset is the particle size distribution.

Table 4.1 – Physical parameters of as prepared M(O)/CNT from TEM, XRD (Sherrer equation) and TGA analysis

		Au/CNT	Pt/CNT	Pd/CNT	Ru/CNT	Co_3O_4/CNT
Size (nm)	**TEM**	8.8	4.9	6.3	1.6	9.7
	XRD	8.9	5.2	6.4	1.5	9.5

Binder-free M(O)/CNT electrodes from **Figure 4.1** were tested in Li-O_2 cells utilizing 0.5 M LiTFSI/tetraglyme (<20 ppm H_2O from Karl-Fischer titration). Galvanostatic DC was conducted to the cutoff potential of 2.2 V followed by RC to the equivalent capacity at the current density of 50 mA g^{-1} (**Figure 4.2**). The DC potential plateaus are all comparable at ~2.7 V, indicating the insensitivity or absence of any significant promotion effect towards ORR irrespective of M(O) NPs.[24-26] The DC capacity varies, ranging from the promoter-

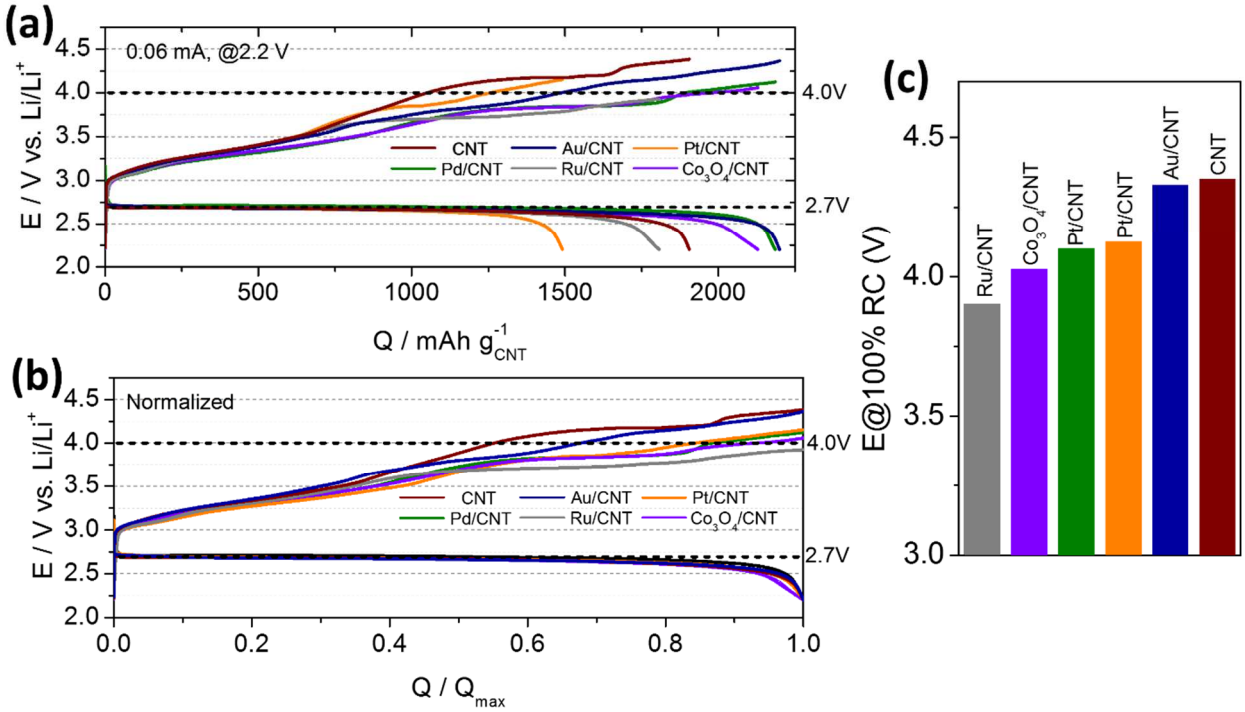

Figure 4.2 – First cycle discharge (DC) and recharge (RC) profiles for M(O)/CNT (<10 nm) (a) Galvanostatic testing performed with 0.5 M LiTFSI/tetraglyme at current density of 50 mA g^{-1}_{CNT} (b) Corresponding capacity normalized DC-RC profiles and (c) Summary of potential at the end of RC.

free CNT at ~1900 mAh g^{-1}_{CNT}, while Pd/CNT and Au/CNT and Co_3O_4/CNT provide higher capacities of over 2000 mAh g^{-1}_{CNT} and Pt/CNT and Ru/CNT exhibit lower capacities in the range of 1500–1800 mAh g^{-1}_{CNT}. The difference in capacity indicate that there is a combination of possible influencing factors with more at play than the intrinsic O_2 and LiO_2 adsorption affinity of the promoter surface.[5,27] Overall, the capacities are distributed within 20% of the CNT capacity. Turning our attention RC, the initial 400 mAh g^{-1}_{CNT} (~25% RC) shows comparable potential profiles (**Figure 4.2a-b**). Subsequently, we observe

diverging and rising RC potentials, finishing with different potentials at the end of RC (**Figure 4.2c**).[3] Furthermore, the resulting depth of RC in which 4 V is reached (**Figure 4.2b**) is earliest for CNT and Au/CNT at 55% and 66% of RC, respectively. In contrast, Pt/CNT, Pd/CNT and Co_3O_4/CNT reach 4 V later, at 84, 86 and 93% of RC, respectively. Ru/CNT is the notable exception in which RC is completed before 4 V is reached. In all, it is clear that the M(O)/CNT electrodes, with the exception of Au/CNT, significantly suppress the rise in RC potential giving higher round-trip efficiencies in comparison to CNT.

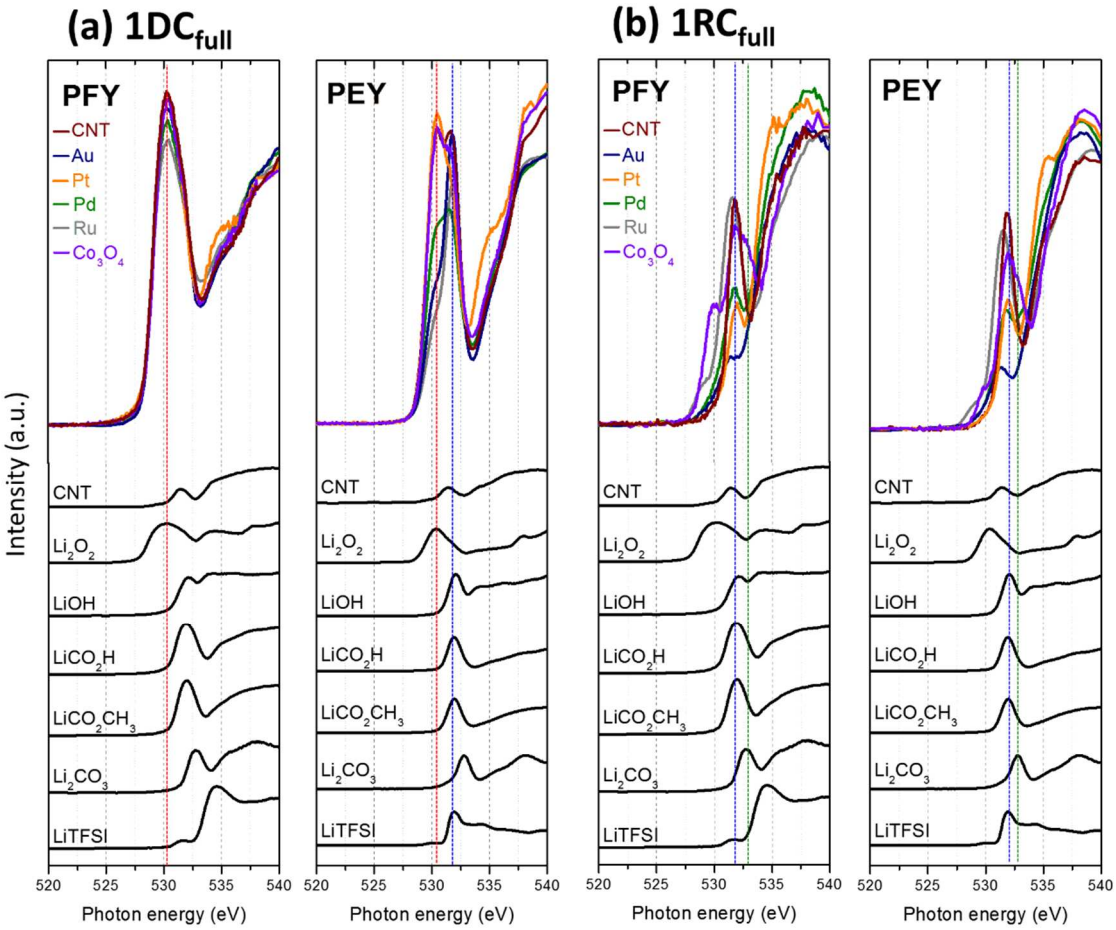

Figure 4.3 – O K-edge XANES analysis of the DC-RC electrodes with bulk-sensitive partial fluorescence yield and surface-sensitive partial electron yield modes (a) DC to 2.2V and (b) RC to equivalent capacity. The spectra are overlapped to emphasize the three peak locations (Li_2O_2, Li carboxylates, and Li_2CO_3), while the spectra separated plots are in Figure C1. The coloured vertical lines in (a and b) emphasize the presence of (red) Li_2O_2 (blue) Li carboxylates and (green) indicates Li_2CO_3

Complementary chemical analyses with XANES and FTIR were performed with the DC and RC electrodes. Following DC, the O K-edge XANES in **Figure 4.3a** (separated spectra in appendix C, **Figure C1)** identifies Li_2O_2 as the predominant product with the clear σ*(O–O) feature at 530 eV for all electrodes. FTIR corroborates the predominant Li_2O_2 product with the adsorption feature at 515 cm^{-1} (**Figure 4.4**). Upon closer comparison

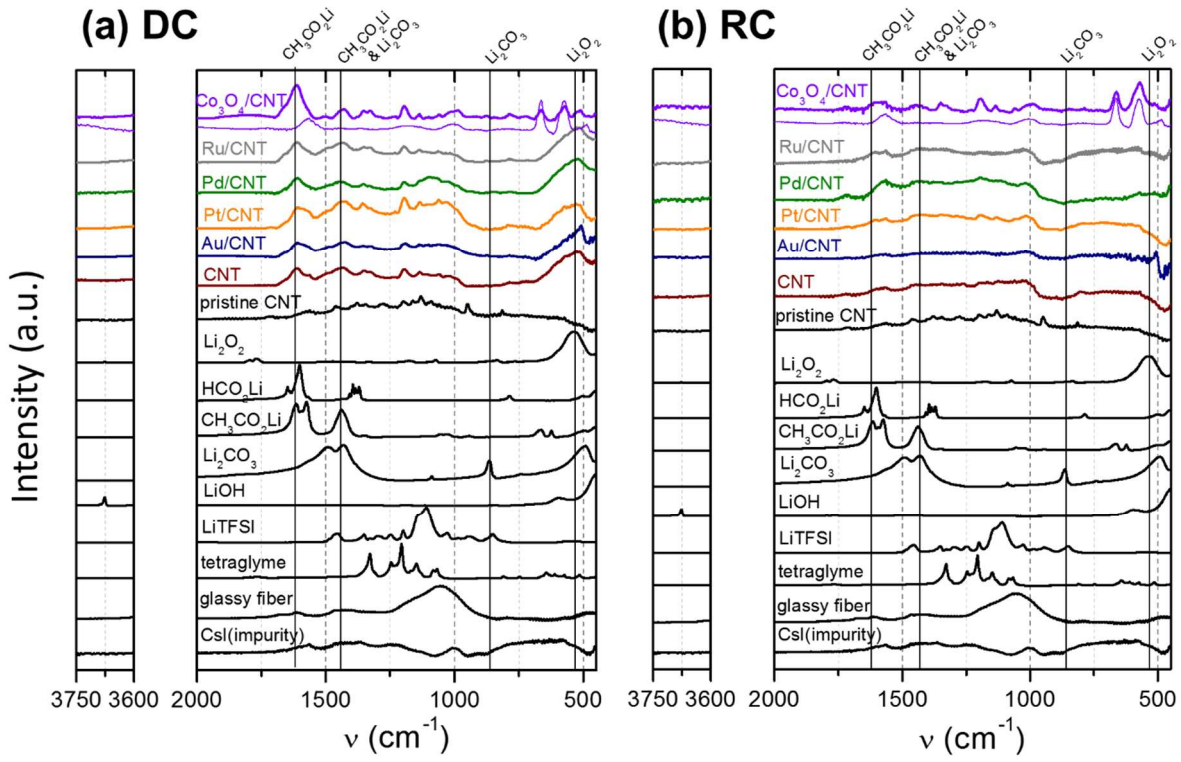

Figure 4.4 – FTIR analysis of DC and RC electrodes (a) DC to 2.2 V and (b) RC to equivalent capacity. The DC involved the cutoff of 2.2 V with RC to the equivalent capacity along with standard powders for comparison. The thin line for Co_3O_4/CNT is the spectra for the as-prepared electrode.

between the surface-sensitive partial electron yield (PEY) and bulk-sensitive partial florescence yield (PFY) modes (**Figure 4.3**) reveals that the outermost surface contains lithium carboxylates (lithium formate ($LiCO_2H$) and acetate ($LiCO_2CH_3$)), evidenced in the PEY mode with the shoulder at ~532 eV. The presence of lithium carboxylates is corroborated by FTIR with the presence of CO_2^- stretching bands observed at 1370–1615 cm^{-1}. Lithium carboxylates are however, notably prevalent for Ru/CNT and Pd/CNT, which is also observed in the Li K-edge spectra (**Figure C2)**. It should be noted that the existence of

lithium hydroxide (LiOH), of which its O K-edge peak is in close proximity to the lithium carboxylates can be discounted on the basis of the Li K-edge (**Figure C2**) and FTIR results (**Figure 4.4**), show the absence of the OH stretching band at ~3678 cm^{-1}. The DC product morphology (**Figure 4.5**) characterized with scanning electron microscopy (SEM) is thin-film-like for all electrodes, indicative of negligible H_2O.

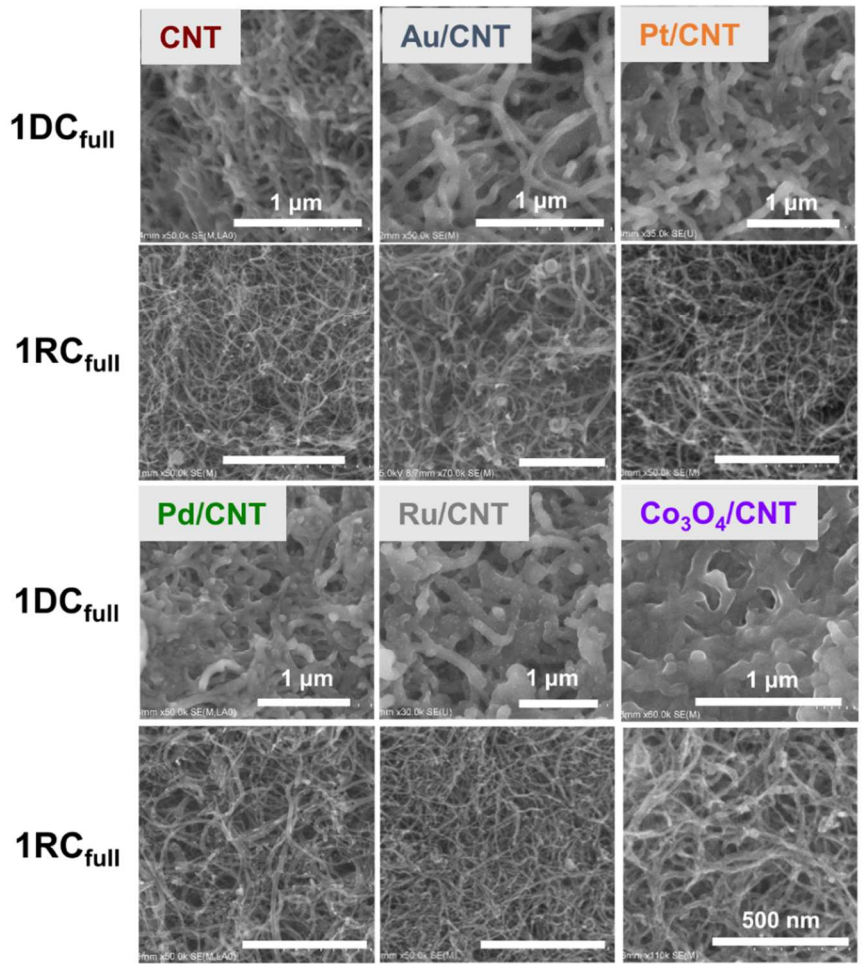

Figure 4.5 – Scanning electron micrographs (SEM) following (a) DC and (b) RC. SEM images are after DC to the cutoff of 2.2 V and following RC to the equivalent capacity.

Following RC, the O K-edge XANES (**Figure 4.3b**) and FTIR (**Figure 4.4**) identify that Li_2O_2 is no longer present. However, regarding the detection of side products, the small absorption peak feature at 532.8 eV is associated with lithium carboxylates with an additional

shoulder arising from π* (C=O) of Li_2CO_3. Additionally, Ru/CNT and Co_3O_4/CNT show pre-edge features at 527.5 eV, indicative of RuO_2[28] and Co_3O_4 (as-prep in **Figure C1**). The RC electrodes with SEM analysis reveals that the existing film products are mostly removed from the M(O)/CNT framework (**Figure 4.5**). In all, these results corroborate that the predominant Li–O_2 electrochemical processes are involved in the formation and decomposition of Li_2O_2 during DC and RC, respectively.

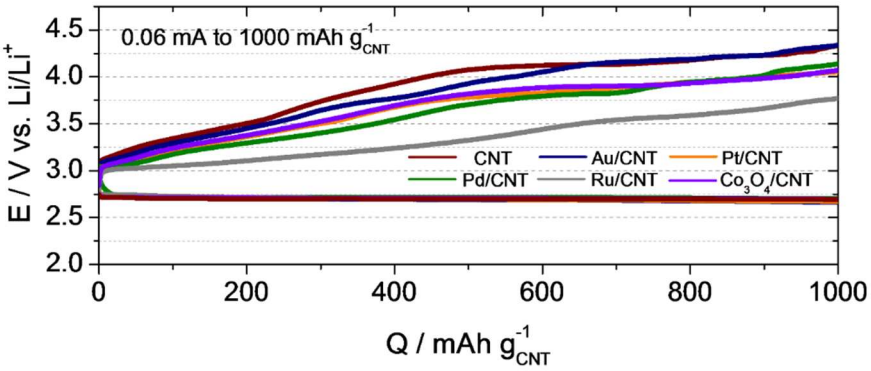

Figure 4.6 –Combined DC-RC profiles captured from the OEMS data in Figure 4.7. The potential at the end of RC (100% RC) correlates well with the full discharge (to 2.2 V) found in Figure 4.2 implying that the RC behavior is irrespective of the depth of DC or amount of Li_2O_2.

Next, to evaluate the gas evolution trends and to quantitatively evaluate reversibility, *in situ* on-line electrochemical mass spectrometry (OEMS) was performed at the fixed capacity of 1000 mAh g^{-1}_{CNT} (**Figure 4.7**). The RC profiles show similar overpotentials trends irrespective of whether DC is to 2 V or at the fixed capacity of 1000 mAh g^{-1} (**Figure 4.6**). *In situ* pressure monitoring during DC reveal comparable values of overall ~2.0-2.1 e^-/O_2 (**Figure 4.7** and **Table 4.2**), suggesting that Li_2O_2 formation is the predominant process. However, as supported by XANES (**Figure 4.3**), despite the overall DC value of 2 e^-/O_2, the electrodes nevertheless contain side products. The *in situ* OEMS measurements of the subsequent RC shows predominantly O_2 evolution for all electrodes at an overall ~3.3-3.6 e^-/O_2 equating to round-trip O_2 efficiencies of 57-64% (**Table 4.2**). The predominant O_2

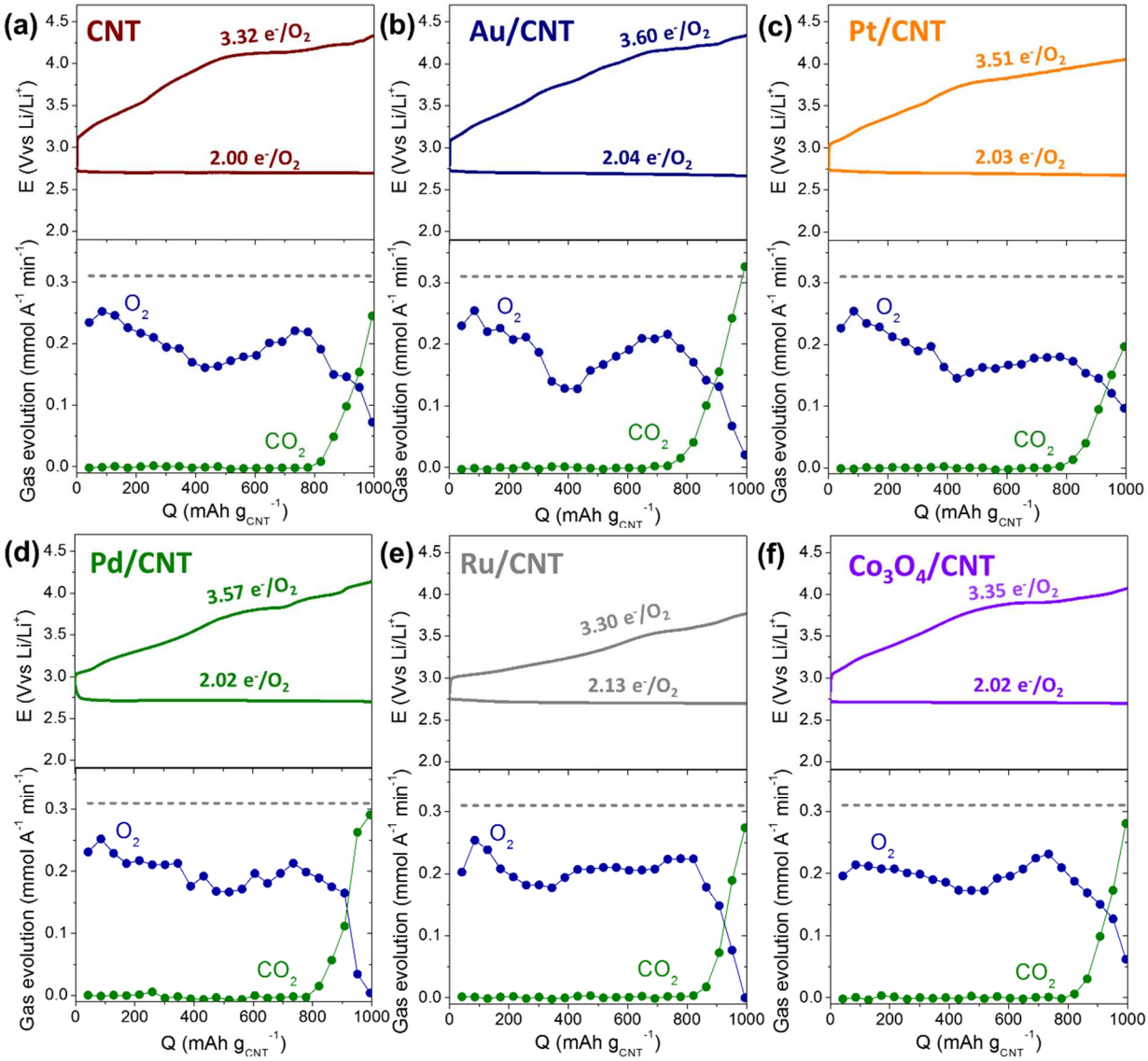

Figure 4.7 – *In situ* on-line electrochemical mass spectrometry (OEMS) performed with 0.5 M LiTFSI/tetraglyme at current density of 50 mA g^{-1} to the fixed capacity of 1000 mAh g^{-1}. (a-f) CNT, Au/CNT, Pt/CNT, Pd/CNT, Ru/CNT and Co_3O_4/CNT, respectively. The overall DC and RC e^-/O_2 values are included (found in tabulated form in **Table 4.2**). The dashed lines indicate the 2 e^-/O_2 evolution rate.

evolution shows that M(O) promoters do contribute in reducing the potential to decompose Li_2O_2. However, the 2 e^-/O_2 evolution rate is not reached at any stage of RC, indicating the entire process involves a mixture of Li_2O_2 oxidation accompanied by parasitic processes. More importantly, these findings unequivocally show that reducing the RC potential with M(O) promoters is not accompanied by any significant enhancement in reversibility. This is exemplified with Ru/CNT where 100% RC completes at 3.77 V (comparable to

literature),[15,28] but exhibits comparable reversibility to CNT (both at ~3.3 e^-/O_2). As RC further proceeds, CO_2 evolution is observed for all electrodes, occurring at ~75-80% of RC. There are notable differences in the CO_2 evolution onset potentials (**Figure 4.7** and **Table 4.2**) showing improved kinetics of M(O)/CNTs toward the decomposition of side products. The CO_2 onset potential is highest for CNT and Au/CNT at ~4.16 V, while Ru/CNT at the lowest potential at 3.6 V (**Table 4.2**). The O_2 and CO_2 evolution trends together show that Au/CNT and Pd/CNT have slightly higher overall e^-/O_2 values at ~3.6 e^-/O_2 and this is accompanied by greater degrees of CO_2 evolution (79 and 31% greater CO_2,respectively than CNT), with the other M(O)/CNTs showing comparable CO_2 evolution to CNT.

Table 4.2 – Summary of *in situ* gas analysis results. DC values obtained through in situ pressure monitoring while mass spectrometry measurements were utilized during RC.

	CNT	**Au/CNT**	**Pt/CNT**	**Pd/CNT**	**Ru/CNT**	**Co_3O_4/CNT**
Overall DC (e^-/O_2)	2.00	2.04	2.03	2.02	2.13	2.02
Overall RC (e^-/O_2)	3.32	3.60	3.51	3.57	3.30	3.35
O_2 evolved/consumed (%)	60	57	58	57	64	60
CO_2 onset potential (V)	4.17	4.16	3.92	3.92	3.60	3.92
Potential at 1300 mAh g^{-1} overcharge (V)	4.71	4.68	4.14	4.41	3.91	4.43

The overcharge behavior and gas evolution (>100% RC) was concurrently evaluated (**Figure 4.8**). Upon overcharge, negligible O_2 evolution is observed for all electrodes indicating the Li_2O_2 is no longer present, which is in agreement with XANES results following RC (**Figure 4.3**). With CNT, overcharging reveals the high potential tail with the CO_2 evolution rate peaking at 103-108% RC, coinciding with the onset of H_2 evolution and the increase in potential, which reaches to a new plateau at ~4.7 V (**Table 4.2**). Taking this

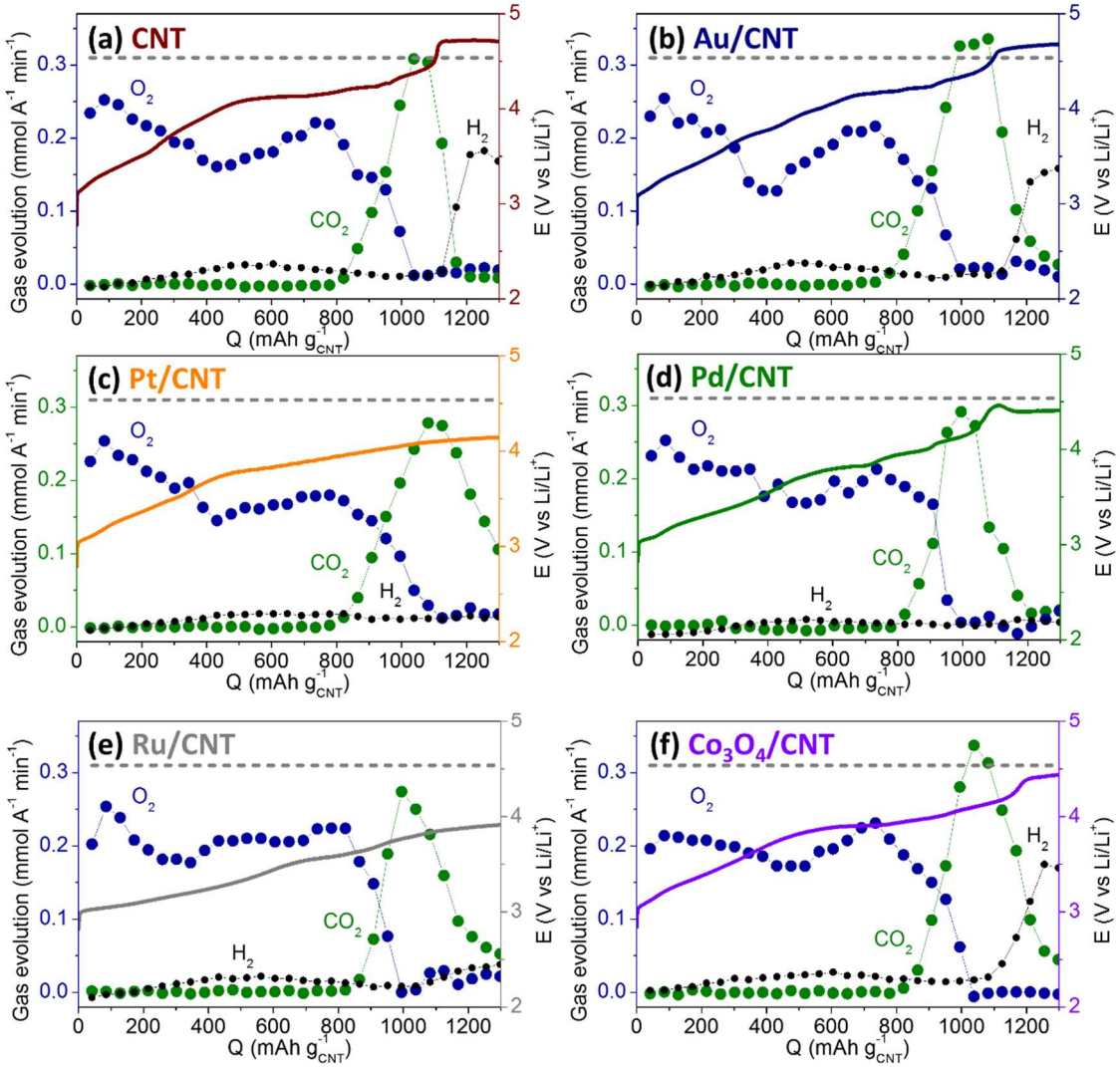

Figure 4.8 - *In situ* OEMS showing complete O_2, CO_2 and H_2 evolution profiles up to 1300 mAh g^{-1} (overcharge), extended from Figure 4.5 performed with 0.5 M LiTFSI/tetraglyme at current density of 50 mA g^{-1} of (a) CNT (b) Au/CNT (c) Pt/CNT (d) Pd/CNT (e) Ru/CNT and (f) Co_3O_4/CNT. The H_2 evolution is not calibrated and is for qualitative comparison. These data are the extended gas evolution spectra shown in Figure 4.7. The dashed lines indicates the 2 e^-/O_2 evolution rate

together, the peak in CO_2 evolution is ascribed with the end of side product oxidation, which is followed by the transition to electrolyte oxidation. The continuation of CO_2 evolution during overcharge is consistent with the XANES results (**Figure 4.3**), which indicates remaining Li carbonate and carboxylates after 100% RC. Similar to CNT, Au/CNT, Pd/CNT and Co_3O_4/CNT also exhibit the transition to a higher voltage plateau, however, Pt/CNT and Ru/CNT do not show any change with respect to potential with the absence in any transition

even up to 130% RC (1300 mAh g^{-1}) reaching the potential of 4.14 and 3.91 V (**Table 4.2**), respectively. Also noteworthy is that Pt/CNT, Pd/CNT and Ru/CNT do not show significant H_2 evolution during overcharge, with Pd/CNT not exhibiting gas evolution despite the transition plateau to higher potential (to ~4.4 V, **Table 4.2**). The examination of the Pt/CNT, Pd/CNT and Ru/CNT mass spectrometry data during overcharge (from m/z = 0 to 80), do not indicate any fragments outside of those related with CO_2 and H_2. This indicates that with Ru/CNT and Pt/CNT, electrolyte decomposition occurs at ~4 V and is accompanied with CO_2 evolution. Moreover, the unwavering potential of Pt/CNT and Ru/CNT even at 130% RC, indicates that this is a steady process which appears to occur in perpetuity and can be ascribed to the perpetual production and decomposition of CO_2 evolving side products (Li carbonates). In all, these results reveal that with the exception of Au/CNT, the potential for electrolyte oxidation is lowered in the presence of M(O)/CNT, particularly with Ru/CNT and Pt/CNT which also present different decomposition pathways.

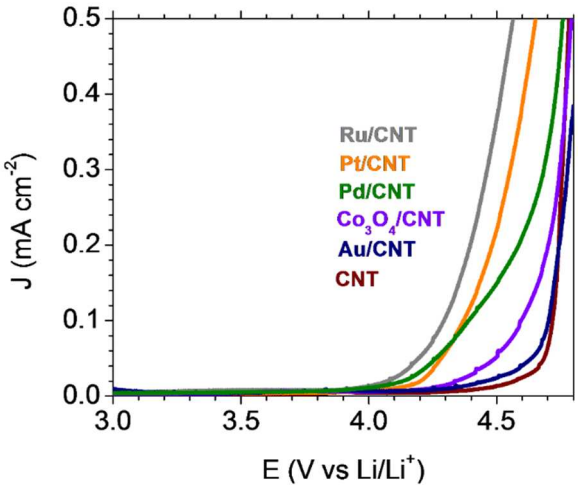

Figure 4.9 – Anodic linear sweep voltammograms (LSV) of M(O)/CNTs performed under Ar with 0.5M LiTFSI/tetraglyme with at 0.05 mV s^{-1} from 3 to 4.8 V. The in situ OEMS data is presented in Figure 4.10.

Additional anodic linear sweep voltammetry (LSVs) without prior reduction (**Figure 4.9**) corroborate the catalytic activity of M(O)/CNTs (with the exception of Au/CNT)

towards the oxidation of electrolyte. The corresponding OEMS results (**Figure 4.10**) show that Pt/CNT, Ru/CNT do not exhibit H_2 evolution until ~4.2 and 4.7 V, respectively, which correlates well with the galvanostatic overcharge results (**Figure 4.8**), corroborating that electrolyte oxidation with Pt/CNT and Ru/CNT is not accompanied with H_2 evolution. Pd/CNT decomposes electrolyte in a manner that produces no significant H_2 evolution even up to 4.8V.

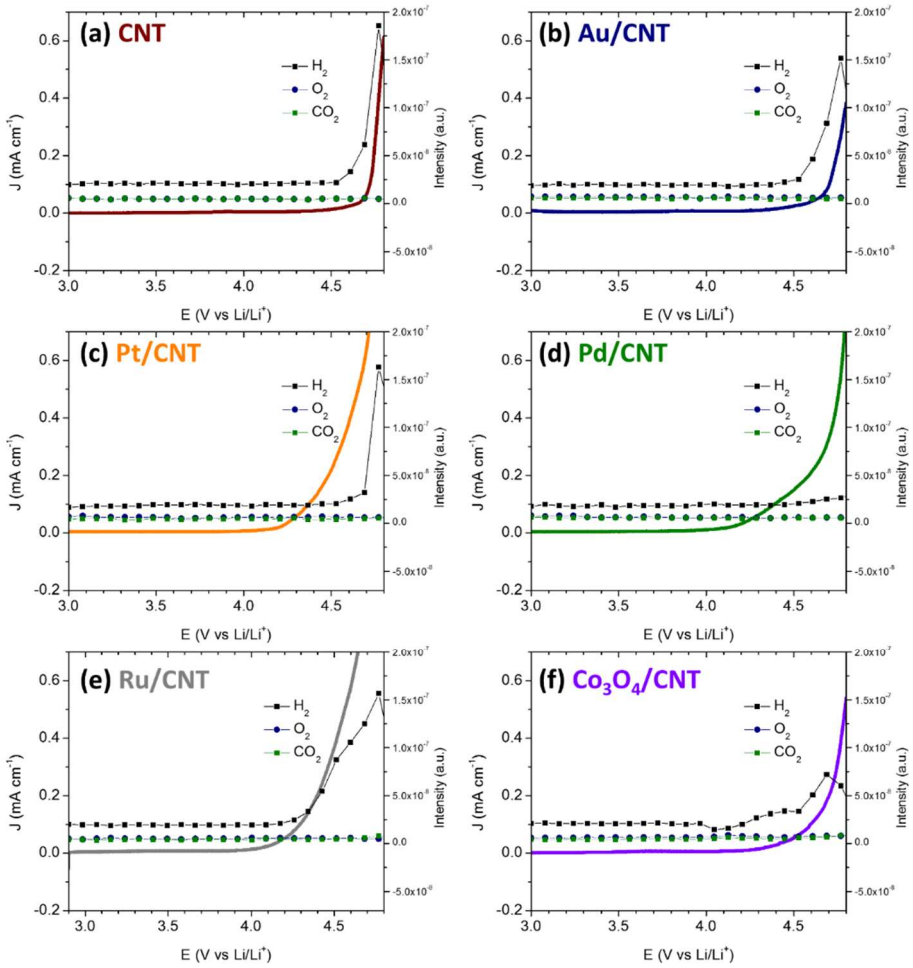

Figure 4.10 - *In situ* OEMS of anodic LSV without prior DC performed with 0.5 M LiTFSI/tetraglyme from 3 to 4.8 V at 0.05 mV s^{-1} showing qualitative comparison of O_2, CO_2 and H_2 evolution profiles (a) CNT (b) Au/CNT (c) Pt/CNT (d) Pd/CNT (e) Ru/CNT and (f) Co_3O_4/CNT

Although the M(O)/CNTs exhibit comparable reversibility in the first cycle (~60% O_2 recovery), the cycling stability is also interesting to evaluate. The evaluation of cycleability

was performed at the fixed capacity of 1000 mAh g^{-1}_{CNT} at the current density of 50 mA g^{-1} with respect to the mass of CNT in **Figure 4.11 (**cycle separated in **Figure C3**). We observe that CNT and Au/CNT are the only two electrodes able to retain its capacity at >1400 h (equivalent to > 36 cycles) of cycling, while in contrast, Ru/CNT and Pt/CNT, do maintain reduced overpotentials but show significant earlier capacity fade at ~800-900 h of cycling and

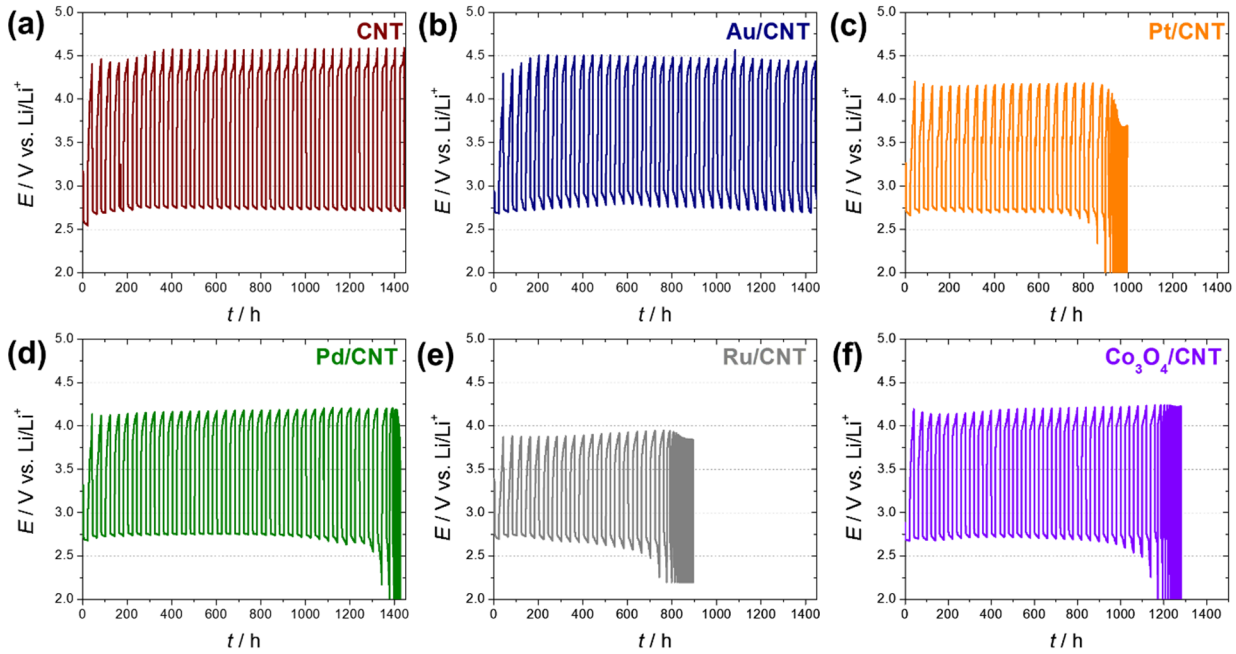

Figure 4.11 – Cycling performance of M(O)/CNTs (a-f) CNT, Au/CNT, Pt/CNT, Pd/CNT, Ru/CNT and $C_{o3}O_4$/CNT, respectively. Cycling performed at the fixed capacity of 1000 mAh g^{-1}_{CNT} with RC to the equilvent DC capacity. Testing performed with 0.5M LiTFSI/tetraglyme at current density of 50 mA/g_{CNT}. The galvanostatic plots of capacity versus voltage is presented in Figure C3.

can only maintain 1000 mAh g^{-1} for 19 and 22 cycles, respectively. This furthermore indicates that there is no correlation between the first cycle RC overpotential and cycleability where, CNT provides sustained capacity retention despite having the highest overpotential. In subsequent cycles, side reactions (electrolyte and electrode decomposition) become prominent[29-31] with the failure mechanism ascribed to the accumulation of passivating side products on the electrode surfaces which stifling charge transfer, indicating that to achieve sustained capacity retention, lower degrees of side reactions and/or the ability to

effectively decompose side products becomes very important.[11,32] We have previously reported that the efficient elimination of Li carbonate and carboxylates with nanoporous NiO plates allows for prolonged cycling.[11] Correlating cycleability with the *in situ* OEMS results presented above (**Figure 4.5**), Au/CNT exhibits the greatest amount of CO_2 evolution indicating its promotion behavior towards decomposing side products which can lead to the increase in cycleability. On the other hand, the poor capacity retention of Ru/CNT and Pt/CNT, can be related to the perpetual side product formation/decomposition at ~4 V, as evidenced CO_2 evolution during overcharge (**Figure 4.8**).

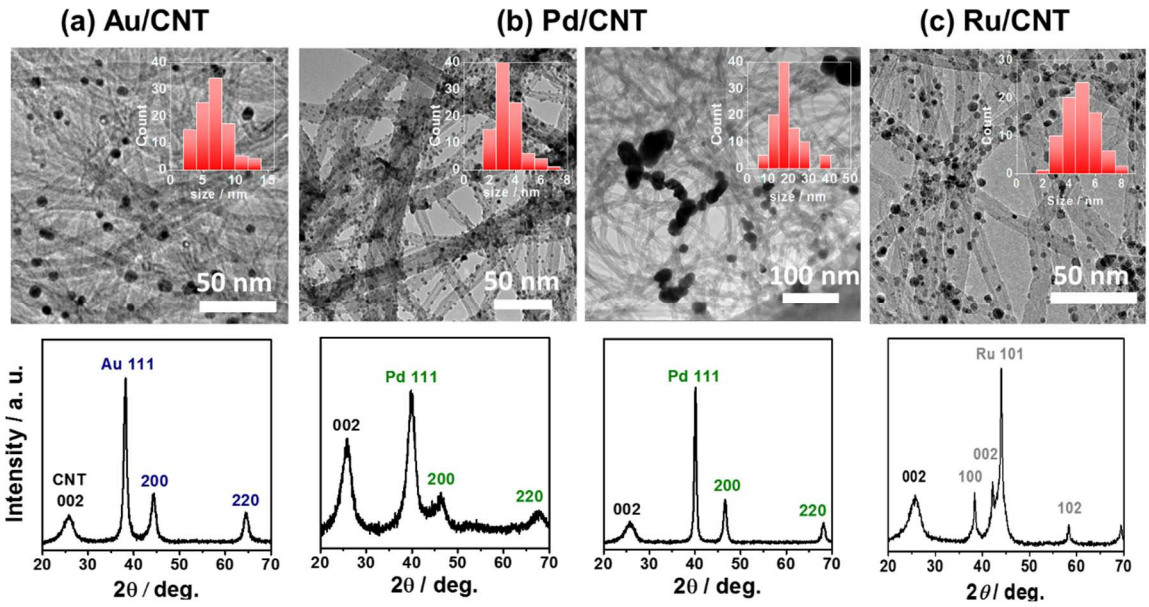

Figure 4.12 – Modulation of M(O) NP size (a) Au/CNT (b) Pd/CNT and (c) Ru/CNT with corresponding TEM and XRD analyses. The inset is the particle size distribution.

Table 4.3 – Summary of modulation of Au/CNT, Pd/CNT and Ru/CNT size from Figure 4.8

		Au/CNT	Pd/CNT		Ru/CNT
Size (nm)	**TEM**	6.5	3.4	17	5.6
	XRD	7.3	4.1	16.4	6.6

To further extend our investigation, the effect of particle size, the M(O) NP size was modulated by reducing the Au/CNT size at 6.5 nm, reducing and increasing Pd/CNT to 3.4

and 17 nm, and increasing Ru/CNT size to 5.6 nm, while keeping the loading at ~40 wt% (**Figure 4.12** and **Table 4.3**). The DC-RC profiles at the fixed capacity of 1000 mAh g^{-1} in **Figure 4.13** (with DC to 2.2 V in **Figure C4**), reveal that there is an overpotential dependence on M(O) NP size, with the tendency of slightly lower RC overpotentials for smaller NP size. More importantly, even when the size of Ru/CNT increases from 1.6 to ~5 nm, the potential at the end of RC is < 4 V and the overall trend in potential remains the same (end potential is Au > Pd > Ru) irrespective of particle size. Individually, Pd/CNT and Ru/CNT exhibit < 100 mV difference (when < ~10 nm in size) throughout RC (**Figure 4.13**), while the maximum difference for Au/CNT is < 200 mV. Accordingly, *in situ* OEMS reveals that irrespective of M(O) NP size, CO_2 evolution imitates at comparable potentials at ~4.1 V for Au/CNT, ~3.9 V for Pd/CNT and ~ 3.6V for Ru/CNT. With respect to reversibility, *in situ* OEMS (for Au/CNT and Pd/CNT) reveals comparable reversibility irrespective of particle size (at ~3.3-3.6 e^-/O_2) (**Figure C5**). Overall, these results are in line with the notion that OER activity (see below) is predominantly surface specific[33] and additionally, is not strongly correlated with NP size.

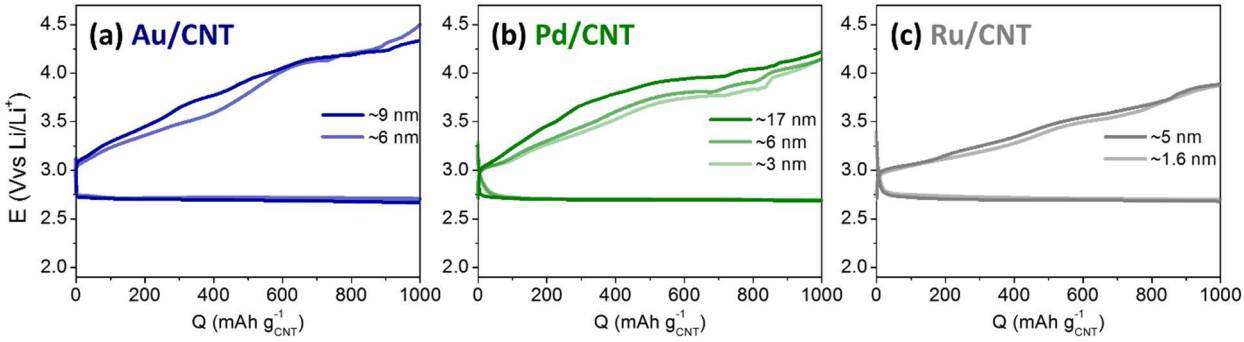

Figure 4.13 – Effect of M(O) NP size on DC-RC profiles (a) Au/CNT (b) Pd/CNT and (c) Ru/CNT. Performed with 0.5 M LiTFSI/tetraglyme with current density of 50 mA g^{-1}_{CNT}.

Moving on to the origin of the reduced RC potential, there have been several proposals including: (1) the adsorption affinity of O_2 and LiO_2 with the electrode

surfaces,[28] (2) possible conversion reactions involving Li-metal-oxide formation and delithation, (3) soluble metal ions resulting in *in situ* doping of Li_2O_2,[34] or impurities produced *in situ* such as water acting as a redox mediators,[35] which will be expanded upon below.

The use of LiTFSI/tetraglyme with moderate donor numbers (DN) (16.6 and 5.4 kcal mol^{-1} for tetraglyme and $TFSI^-$ anion, respectively),[36,37] means that after the first ORR Li/e^- transfer ($Li^+ + O_2* + e^- \rightarrow LiO_2$, the asterisk * denotes surface adsorbed species), the mobility of the LiO_2 intermediate is governed by the competition between the solvation affinity of the electrolyte (Li_2O_2 formation *via* solution ($2LiO_2(sol) \rightarrow Li_2O_2 + O_2$)) and the adsorption affinity to the electrode surface.[38,39] We have shown in our previous report with RuO_2 NPs on CNT[28] that the reduction in overpotential for Li_2O_2 decomposition is ascribed to the strong adsorption affinity of O_2 and LiO_2 of the preceding DC, leading to the preferential surface-adsorption-based nucleation and growth of Li_2O_2 ($LiO_2* + Li^+ + e^- \rightarrow Li_2O_2$) and consequently, promotes the formation of conformal and amorphous Li_2O_2.[40,41] Consequently, charge transport is more facile with the higher electronic and ionic conductivities of amorphous Li_2O_2 (5.02×10^{-9} and 7.10×10^{-8} S cm^{-1}, respectively) in comparison to crystalline Li_2O_2 (~10^{-20} S cm^{-1} for both electronic an ionic conductivities),[42,43] allowing for the facile decomposition of Li_2O_2.[31] Equally noteworthy are computation and experimental studies on the O_2 adsorption energy of metal and carbon surfaces, [27,44] where Ru is noted for its high O_2 adsorption energy following the order Ru > Pt ≈ Pd > Au > C, which notably follows the OER activity trend in our present study.

The occurrence chemical conversion reactions has been speculated to contribute to the promotion of bulk Li_2O_2 oxidation in preloaded electrodes by way of Li-metal-oxide

formation followed by delithation.[14] It should be noted that, the potential range of these reports is ≥3.9 V, with full delithiation requiring >4.5 V, which is not necessary in line with the case of electrochemically formed Li_2O_2.[14] Our results show that electrochemically formed Li_2O_2 in the presence of M(O) promoters, the majority of Li_2O_2 decomposition occurs below 4 V. Moreover, this is not necessary applicable to promoters including Pt, Au, and Pd with the formation of Li-metal-oxides. Moreover, our previous work with XRD analysis of RuO_2/CNT, and XANES analysis with NiO/CNT[11] following RC and CeO_2/CNT[38] throughout RC, have shown no indication of the change to a lithiated phase involving the change in oxidation state of the M(O). We note that the metal K and L-edge XANES was not probed with the depth of RC, which can be the key of the high activity with Ru. Certainly the observation of RuO_2 in the O K-edge XANES (**Figure 4.3c-d**) following RC, may warrant further investigation.

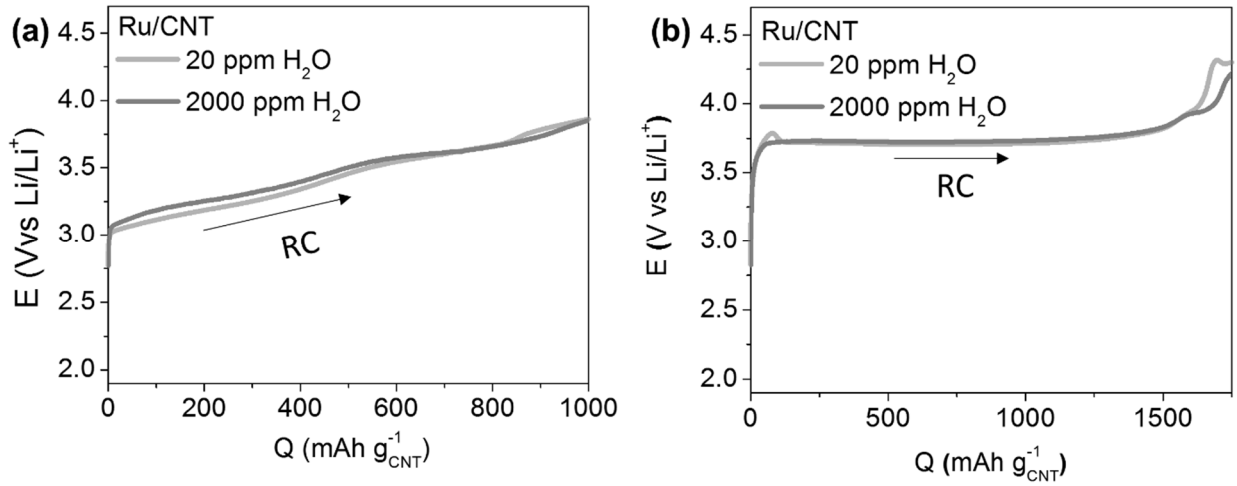

Figure 4.14 – Influence of H_2O (20 ppm and 2000 ppm) with Ru/CNT (a) Galvanostatic RC result after DC to 1000 mAh g^{-1}_{CNT} at 50 mA g^{-1}_{CNT} (b) Preloaded Li_2O_2 with Ru/CNT performed at 0.1 mA cm^{-2}. These cell tests were obtaind with 0.5 M $LiClO_4$/tetraglyme.

The *in situ* formation of impurities such as water, acting as redox shuttles during cell operation [14,35,41] is not believed to be the origin of the reduced overpotentials and OER activity. Cell tests with Ru/CNT reveal similar RC profiles with 2000 or 20 ppm of H_2O for both preloaded Li_2O_2 or electrochemically formed Li_2O_2 (**Figure 4.14**). The possible *in situ*

doping of dissolved metal ions within the Li_2O_2 deposits, has been suggested computationally to promote charge transport for RC resulting in reduced RC overpotential.[34] However, we have conducted tests with CNT containing 10 mM $RuCl_3$, as an electrolyte additive, which resulted in the rapid increase in RC potential (data not shown). This suggests that significant Ru dissolution and doping (0.1 mM corresponds to 20% molar ratio of Ru dissolution) is not the source of the reduced RC potential, although tests with lower concentrations or spectroscopic analysis of the electrolytes can conclusively disprove this possibility.

4.4 - Conclusion

We have investigated the behavior of M(O) promoters in Li-O_2 cells regarding their efficacy in lowering RC overpotential, the true and predominant DC and RC processes, and the possible origin in reduction of RC overpotential. We find that on one hand, all of the promoters analyzed with the exception of Au/CNT, significantly reduce the RC overpotential with Ru/CNT resulting in the highest round-trip efficiency. The predominant processes occurring during DC and RC is Li_2O_2 formation and decomposition, respectably. However, more importantly, we show that while RC overpotential is reduced, M(O)/CNTs have comparable reversibility (~60%) to the promoter free CNT. Regarding negative effects of M(O) promoters, we demonstrated that with the exception of Au/CNT notably reduce the potential to oxidize the electrolyte. We further investigate the effect of M(O) NP size which identifies that for NPs below ~10 nm, there is relatively weak correlation between NP size and RC overpotential. Our findings offer improved understanding of M(O) NPs and their role toward RC potential, electrolyte stability and reversibility.

Chapter 5

Conclusions and outlook

The development of next generation, post Li-ion batteries is a highly challenging endeavour. Although the challenges associated with Li-O_2 batteries are clearly significant, the lessons learned from this endeavour can be utilized in other post Li-ion battery chemistries including Li-S, Na-O_2, K-O_2 and Mg-O_2 which face similar chemical transformation and interfacial challenges. It cannot be understated that additional work with significant investments to improve fundamental understanding is required and to further extend this knowledge to develop rational solutions. This step-by-step approach will take time and resources and breakthroughs, although unpredictable, are certainly possible. The work presented in this thesis has contributed to the advancement of the non-aqueous Li-O_2 battery with the following studies:

In Chapter 2, the experimental methods central to this thesis is introduced including the electrochemical cells, testing conditions, and post-mortem characterisations. Our analyses essentially consists of three aspects which are morphological, chemical, and quantitative analysis. Our approach of correlating these three characterisation avenues allows for greater understanding by providing a more complete picture of the processes occurring in our Li-O_2 cells. We emphasize the quantitative *in situ* on-line electrochemical mass spectrometry (OEMS) technique to evaluate gas evolution and reversibility, which was constructed and utilized within the laboratory.

In Chapter 3, we elucidated the role of carbon surface chemistry toward the electrochemical behavior in Li-O_2 cells. Through tailoring carbon nanotube surfaces to decouple surface functional groups, defective edges, and degree of graphitization we elucidated the parameters that govern DC capacity, RC potential and the implications to

stability. More ordered and uniform carbon leads to the bias toward solvation-based Li_2O_2 growth, delaying electrode passivation and results in increased capacities. Conversely, the presence of oxygen functional groups, favors surface-adsorption based Li_2O_2 nucleation and growth resulting in more rapid electrode coverage and lower capacities. Consequently, the overwhelmingly surface-adsorption pathway leads to for the formation of amorphous phase Li_2O_2 which can facilely decompose during RC. Lastly, the presence of oxygen functional groups are shown to degrade and defective carbon edges are shown to induce side product accumulation resulting in poor capacity retention upon cycling.

In Chapter 4, we examined the ongoing issue of "solid catalysts" by investigating metal/metal oxide (M(O)) NPs on CNT regarding their efficacy to RC overpotential and actual processes occurring during DC and RC. By analyzing Au, Pt, Pd, Ru, and Co_3O_4 M(O)/CNTs we show that with the exception of Au/CNT, all, M(O)/CNTs lower the RC overpotential, with Ru/CNT exhibiting the lowest RC potential. The predominant processes occurring during DC and RC is Li_2O_2 formation and decomposition, respectively. However we show that despite the reduction in RC overpotential, all M(O)/CNTs result in the similar reversibility of ~60%. Moreover, we show that M(O)/CNTs lower the potential of electrolyte oxidation in comparison to pristine CNT. In all, our findings show that M(O) promoters fundamentally do not mitigate the underlying issue of reversibility in Li-O_2 batteries and affirm the necessity in identifying electrolytes that promote reversible Li-O_2 electrochemistry.

In terms of lessons learned, clearly in this field, the confirmation of the true reactions occurring in Li-O_2 cells is critical. The reaction products should not only be confirmed through spectroscopic techniques but should also be evaluated with quantitative techniques when evaluating reversibility. Accordingly, the utility of *in situ* quantitative gas analysis has been thoroughly established in the field and future work should without question, utilize this technique. Furthermore, to obtain a clearer picture of the predominant processes occurring,

electrochemical characterisations need to be complemented with chemical analysis and morphology analysis which we believe we have convincingly shown in chapter 4.

With respect to future directions of research, the formation of singlet O_2, has been reported at potentials >3.5 V *via* operando EPR (electron paramagnetic resonance) and has been identified as the possible dominant source of RC instabilities.[1] This finding requires further investigation into its confirmation and understanding the mechanism of singlet O_2 formation, severity within the Li-O_2 parasitic chemistry, and its potential role in electrolyte degradation. Taking this further, perhaps avoiding singlet O_2 formation by decomposing Li_2O_2 at low potentials *via* soluble redox mediators to chemically oxidizing Li_2O_2 (ie. LiI, TEMPO)[2] is one possible promising approach in conjunction with more stable carbon-free electrodes and electrolytes.[3] However, in terms of the larger picture, the instability of organic solvents and polymers with LiO_2 and Li_2O_2 has proven to be extremely difficult to completely mitigate,[4] even if the superoxide intermediate is bypassed[5], meaning this approach will have its intrinsic limitations. Recently, the radical approach of molten nitrate salts (operating at ~120-130 ^oC) reported by Liox Inc.[6] has shown some promise in terms of avoiding electrolyte decomposition, although carbon electrode degradation and the decomposition of Li_2O_2 onto inactive components remain as issues. This new development indicates that molten nitrate salts should be investigated further to identify of similar materials along with methods to lower the melting point. Potential solutions of the remaining issues can potentially be approached via hierarchical, nanostructured and non-carbon-based electrodes.

Apendix A

In situ on-line electrochemical mass spectrometry

This section builds on the discussion in Chapter 2 and deals with the specifics with respect to the LabVIEW interface and operation of the on-line electrochemical mass spectrometry (OEMS), quantification procedures, and additional discussions regarding the construction and testing of our OEMS apparatus.

OEMS operation

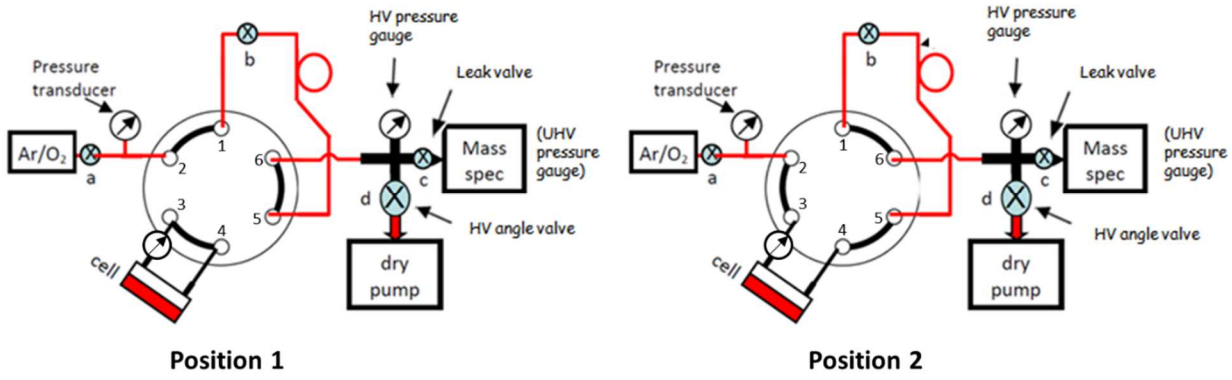

Figure A1 – Schematic diagram of the two positions of the GC switching valve, used during sample injection. Note that valve-b is a 3-way valve allowing it to be open, close, or vent. Vent means that valve-b would be connecting valco port 5 to the outside atmosphere.

For discharge (DC), the cell is first mounted with Ar flowing in position 2 and valve "b" at vent where leak testing was performed under Ar at ~22.8 psi, with the cell isolated in position 2 and valve "a" and "b" in the closed position. After clearing the leak check, valve "a" is switch to O_2 (99.99995% purity, Tomoe Shokai) with valve "b" to vent in order to purge out residual Ar followed by closing valve "b" and ensuring the final pressure is at ~22.8 psi by closing valve "a" and finally isolating the cell in position 1. LabVIEW is used

to record the pressure data throughout discharge. Following DC, the cell is purged with Ar to remove residual O_2 by setting the setup in position 2 with valve “a” and “b” at Ar and vent, respectively. This Ar purging and cell relaxing process at open-circuit potential typically is carried out for ~5 to 6 hours.

Recharge (RC) was performed under Ar (99.995%, Tomoe Shokai) at ~22.8 psi, where the GC valve periodically inject the gas contents of the cell which is detected by a residual gas analyzer (RGA200, Stanford Research Systems). More precisely, while concurrent RC, the cell is isolated in position 1 for a set integration period to allow for gas accumulation to occur. Regarding the other valves, valve “a” is connected to Ar while valve “b” is in the close position. After the integration period, the GC switching valve switches from position 2, then quickly back to position 1 (~500 milliseconds), where a portion of the gas contents of the cell will be inserted into the transfer line (between port 5 and valve, “b” **Figure A1**), which is actually under vacuum during the integration period. When the valve switches back to position 1, the contents of the transfer line will be pushed into the NW-25 cross, where the sample cross pressure rises to ~3-4 mbar, where a portion crosses the leak valve and is subsequently detected by the MS/RGA. After sample injection and detection, the cell was purged for a short period (~90 seconds) to remove residual gas from affecting the following sample injections. This is done in position 2 with valve “b” set to vent. The quadruple MS residual gas analyzer features a faraday cup detector.

With respect to quantification, the volume of the cell head space is a very important parameter that needs to be accurate determined which precludes meaningful quantification. The cell headspace volume could be determined by attaching 1, 2 and 5 mL standard volume loops (VICI Valco instruments) in place of the cell (ports 3 and 4). By pressurizing the setup (with each standard volume loop) to the same pressure in position 2, with valve “b” closed where valve “a” is closed when the set pressure 22.8 psi is reached. This is followed by the

closing the HV angle valve (valve “d”) and valve “b” opened, to release the pressurized contents into the NW25 sample cross. By correlating the pressure rise for each known volume, a calibration curve could be obtained. A representative volume calibration curve is shown in **Figure A2**.

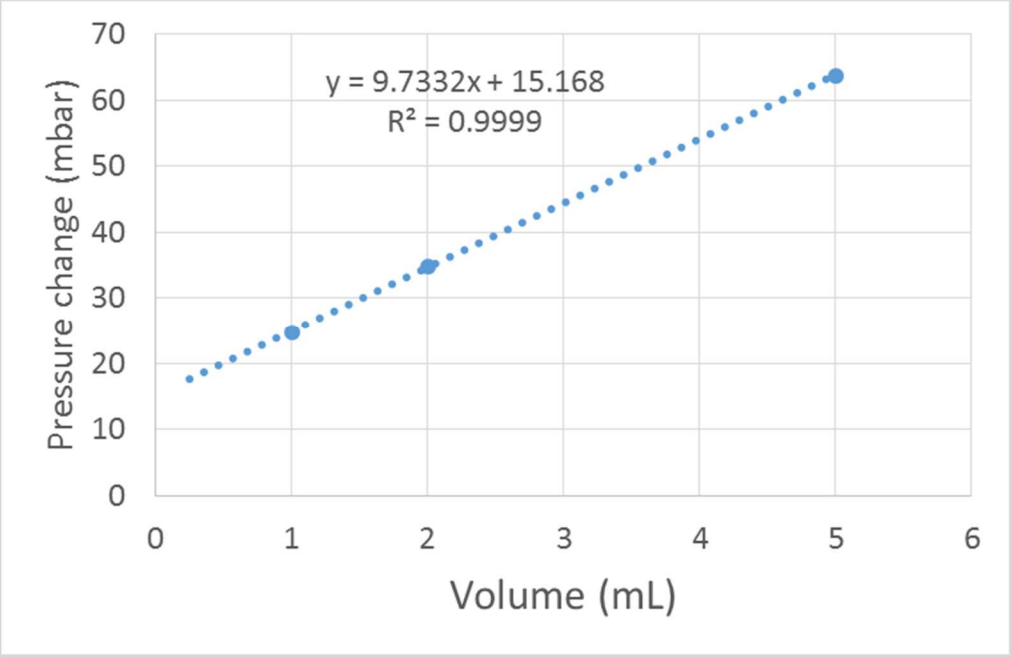

Figure A2 – Representative volume calibration curve used to determine the cell headspace volume for quantitative OEMS analysis

There are several methods used in quantifying the OEMS results. With the headspace volume known from the volume calibration curve, the pressure rise during each integration period can be determined using the ideal gas law. This is extremely versatile in regions where the predominant gas evolution is from a single gas which can be corroborated from the mass spectrometry results. Next, by utilizing samples that evolve single gas such as preloaded commercial Li_2O_2, samples with high single gas evolution regions (ie. CMK-3 carbon-based Li-O_2 cells), calibration curves can also be obtained. A sample calibration procedure is demonstrated in **Figure A3**, where the raw mass spectra and pressure data can be used together to construct the calibration curve consisting of m/z=32 signal intensity

corresponding to O_2 evolution as a function of mol of O_2. The two methods (calibration and pressure) can be used complement each other to ensure the quantification is accurate. It should be noted that when calibration is used to convert the RC spectra, the volume deviation between the calibration data and the target sample should be quite small (<100 μL) to minimize quantification errors.

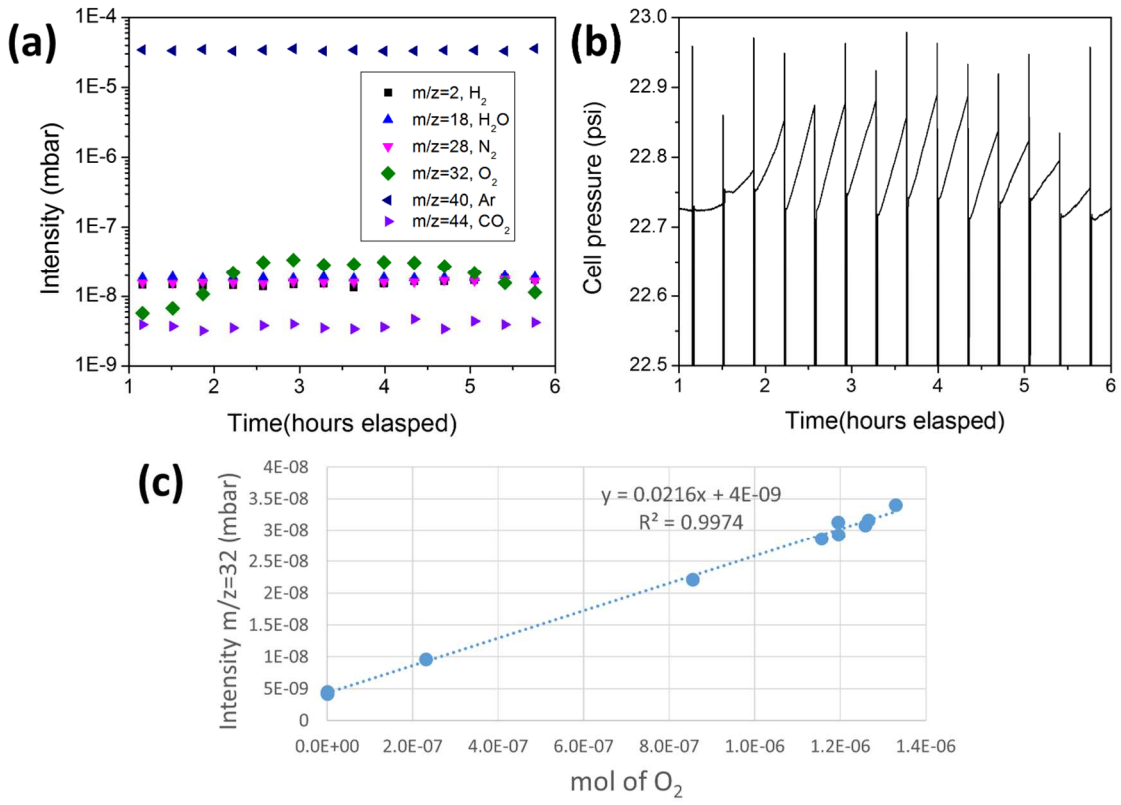

Figure A3– Calibration for quantification of mass spectra data (a) Raw intensities of selected m/z values from the anodic linear sweep voltammogram of CMK-3 mesoporous carbon at 0.05 mV s^{-1} following galvanostatic DC (b) Corresponding pressure response of the same spectra (c) Calibration obtained from mass spectra and pressure data to give m/z intensity signal as a function of mol of O_2.

In terms of applicable standard samples for quantification confirmation, Li-O_2 batteries are dominated by parasitic side reactions and are not stable in terms of providing a standard. However, Na-O_2 batteries have been shown to exhibit ~1 e-/O_2 during DC and RC[1,2] as shown in **Figure A4**.

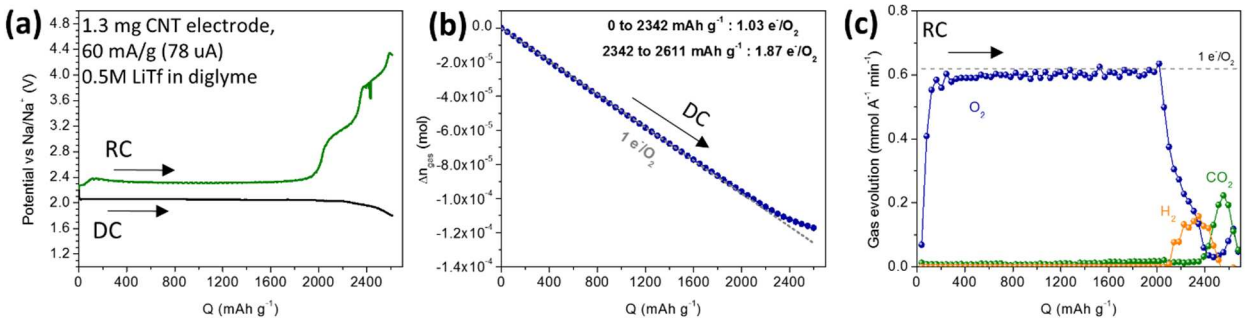

Figure A4 – DC-RC coupled with OEMS of Na-O_2 cell containing 0.5 M Li triflate/diglyme with CNT electrode at current density of 60 mA g^{-1} (a) DC-RC profile (b) in situ pressure drop measurement during DC (c) in situ mass spectrometry measurements during RC. The dashed lines indicates 1 e^-/O_2 evolution rate.

LabVIEW VI Interface

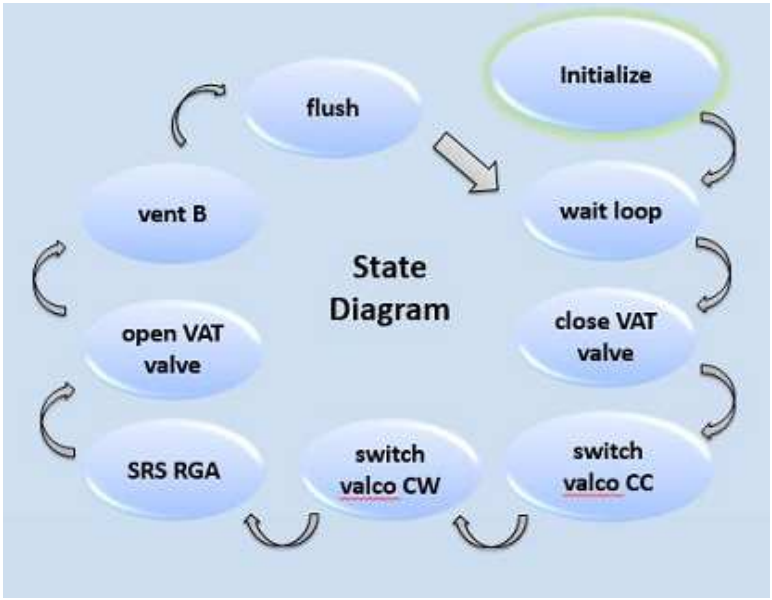

Figure A5– High level state diagram of LabVIEW interface used for OEMS automation.

The constructed LabVIEW VI (virtual instrument) interface has versatility in mind with a state machine architecture allowing for it to function in perpetuity. The utilization of "states" allows for a flexible modular architecture that allows the states to be reordered, skipped, and isolated, which is useful for debugging. From a top level perspective, the VI functions essentially as loop as illustrated in **Figure A5**.

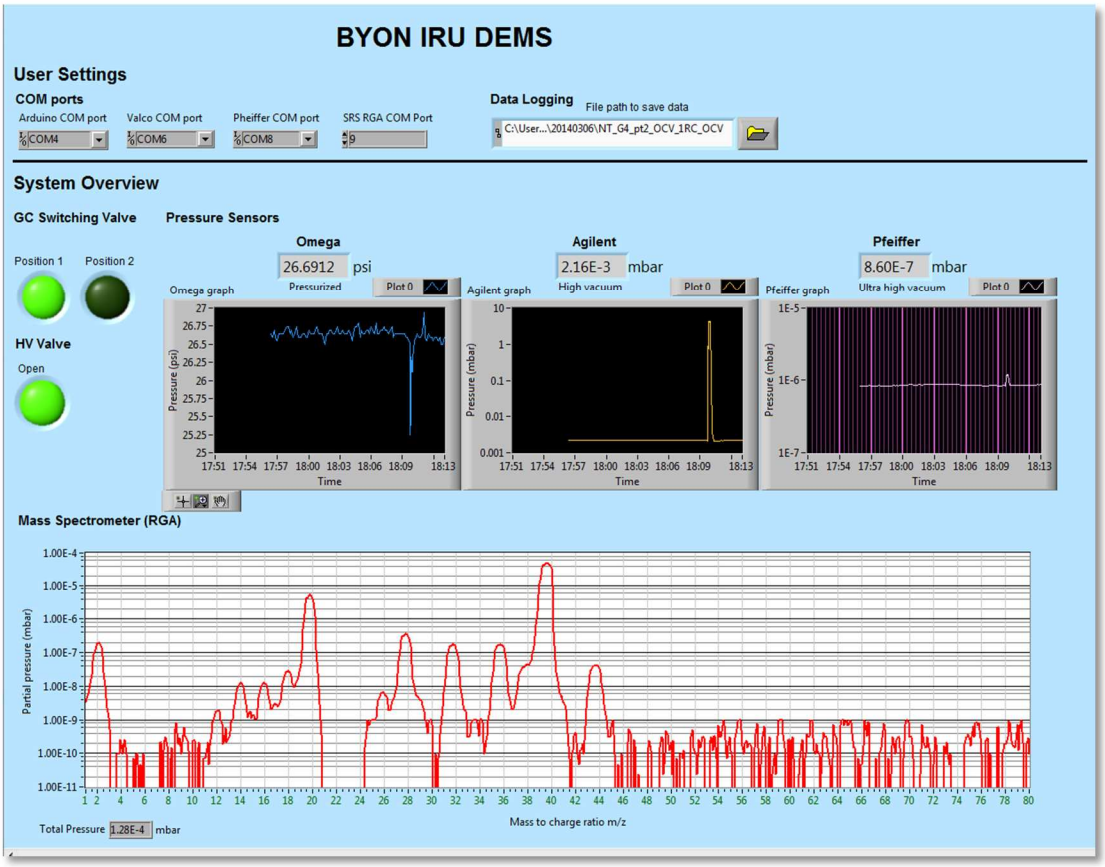

Figure A6 – The "front panel" of the LabVIEW VI interface, during the development stages of the OEMS. There are indicators for the status of the GC valve, pressure and history of pressure and the latest mass spectrometry scan.

The "initialization" state sets the device communication ports, initializes the format of the output text files. The "wait loop" is where the VI spends a significant amount of its time, where the pressure data is recorded and time is incremented until the time elapsed matches the cycle time set by the user. Once the elapsed time matches the cycle time, sample injection occurs by first transitioning to the "close VAT valve" state which closes the valve-d, followed quickly by two sequential states of "switch valvco CC" (counter clockwise) and "switch valco CW" (clockwise) which correspond to switching the GC valve from position 1 to 2 and then back to position 1. Concurrently occurring in these two valco states is the continuous recording of all the pressure data. Next, the "SRS RGA" state deals with reading the RGA and recording the MS data. This portion of the VI is based off of pre-written code

provided as an example from the RGA manufacturer, Stanford Research Systems. The subsequent states is as described in the previous section in OEMS operation, section A.1 with the "open VAT valve" state involved with valve-d reopening, "vent B" involved with setting valve-b to vent and finally flushing which holds the valve-b at vent for 90 seconds before finally returning to the "wait loop" state. An image of the front panel of the LabVIEW VI is in **Figure A6**.

Additional OEMS construction and testing discussion

The leak valve (**Figure A1**), with respect to the number of turns was calibrated/determined by flowing in position 2, an Ar/O_2 mixture at 90 sccm Ar, and 10 sccm O_2 through a 2 mL sample loop with valve b to open. The gas mixture was isolated by changing to position 1 followed by Ar purging with b-open followed by b-close. After equilibrating for several minutes, the gas mixture was injected by switching to position 2, then back to 1 in the period of ~300 ms. The O_2 signal notably increased in compared to the background and this served as the first step in leak valve calibration.

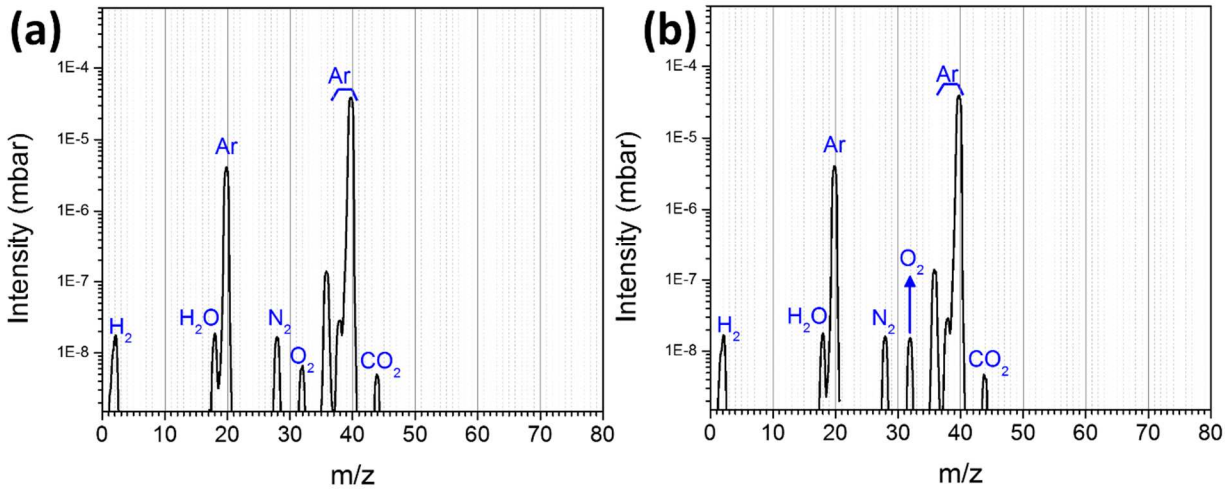

Figure A7 – Mass spectrometry spectra from residual gas analyzer (a) background spectra when cell is under OCP conditions and (b) typical spectra under RC conditions with O_2 evolution occurring

After initial assembly, the background spectra of the mass spectrometer was taken. The typical background with the OEMS cell under open circuit conditions is shown in **Figure A7a.** The background signals should remain constant throughout standard OEMS operation. As one would suspect, the background signals consist of H_2 (m/z=2), H_2O (m/z=18), N_2 (m/z 28), O_2 (m/z=32), Ar (m/z=20, 36, 40) and CO_2 (m/z=28, 44). The typical spectra under RC conditions is shown in **Figure A6b**, where there is a notable increase in O_2 m/z signal at 32.

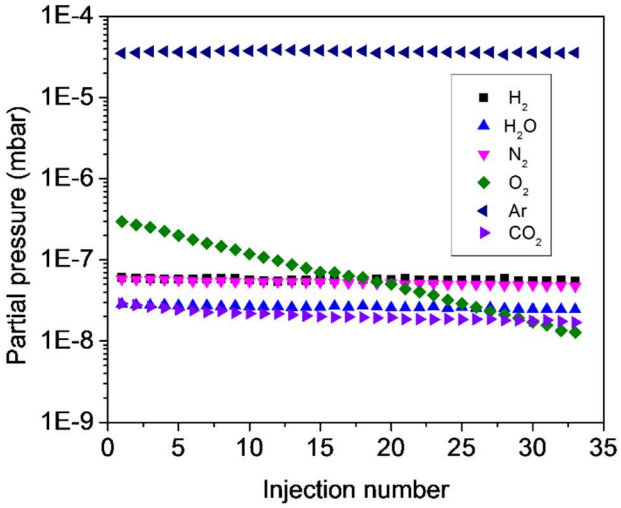

Figure A8 – OEMS mass spectrometry during development with valve-b in the close state during operation. After filling a standard volume loop with 95% Ar and 5% O_2 mixture, sample injection reveals that the O_2 response (green) does not return to its background value even through many subsequent injections

During the development phase, the issue of residual gas remaining in the cell after sample injection became an issue. This was prior to fitting valve-b (**Figure A1**) with a 3-way automated valve where valve-b could only either opened or closed. In this situation, valve-b is in the closed throughout operation. The origin of this residual gas issue is ascribed to the convection of gases in the cell resulting in backflow and inability to remove all the gaseous contents of the current integration period during sample injection.[3] The issue is illustrated in **Figure A8**, where we have filled the a standard volume loop (in place of the cell, attached to) with 95% Ar and 5% O_2 mixture, followed by the repeated sample injection (GC valve from position 1 to 2 then back to position 1). The subsequent injections show reduced O_2

response, however, the value is not a background values. Different attempts to resolve this issue included, increasing the sample tube volume, and increasing the injection time, however, none of these were effective solutions. However, this issue was ultimately solved by purging the cell with Ar after each cycle by modifying valve-b to an automated 3-way valve (with a Swagelok actuator) controlled by LabVIEW.

Apendix B

Supplementary information for Chapter 3

Electrolyte wettability of (surface-modified) carbon nanotube electrodes

Initial motivation for the use of tetraglyme is its relatively high stability in Li-O_2 cells versus other solvents including DMSO and alkyl/cyclic carbonates,[1-3] of which reasonable stability is important for our systematic study focusing on the surface characteristics of multi-walled carbon electrodes. The modifications of the carbon nanotube surfaces including oxidation and removal of defects/oxygen moieties alters the surface properties of carbon nanotube from hydrophilic to hydrophobic, respectively. In this respect, tetraglyme, processing a low dielectric constant (ε = 7.79)[4,5] is defined as a low-polar solvent and gives additional benefit in widespread use for all carbon nanotube electrodes regardless of surface property (from Ox-MWNT to G-MWNT). The observation of negligible contact angles and the thorough permeation of tetraglyme/$LiClO_4$ electrolyte for all of our electrodes indicates the suitable wettability of the electrolyte for all the four carbon nanotube materials tested.

Discussion on calculated (expected) discharge product (Li_2O_2) thicknesses

Based on the BET surface area of the multi-walled carbon nanotubes (~230 m^2 g^{-1}) and the mass of the electrodes (1.2 mg), we can calculate the expected capacity of the cell as a function of assumed Li_2O_2 thickness and compare with the observed values. **Table B1** shows the expected capacity by assuming uniform deposition throughout the 3D carbon nanotube electrode with the thickness between 1-10 nm. The upper value of 10 nm thickness is taken from computational reports on the limitations of charge transport (tunneling and polaron hopping)[6,7] in Li_2O_2. We can see that the expected capacity values do not match with the observe values with the expected capacity of ~7.4 mAh at 10 nm thickness. The result is

ascribed to the additional complexities (ie. mass transport of Li^+ and O_2) within the 3D carbon nanotube matrix and is consistent with our previous observations where the vast majority of the DC product is concentrated at the top most ~20-30% of the O_2 side of the electrode (thickness is ~50 μm),[8] presumably due to delayed disproportionation of LiO_2(sol) from the interior of the 3D electrode.

Taking this further, assume that the DC product covering only 20% of the electrode,[8] and by increasing the thickness to higher values to match values closer to the observed values (**Table B2**). Comparing this to the observed values (**Figure B1**), there is a somewhat reasonable correlation between the observed and calculated values for Ox-MWNT, Ox-MWNT-900 and MWNT. However, there is greater discrepancy when there is greater bias towards the solvation-based Li_2O_2 formation pathway (**Table B2** and **Figure B1**) which is consistent with our previous report.[8] In all these results confirm that there is non-uniform deposition throughout the 3D carbon nanotube electrode matrix, with Li_2O_2 deposition favored in the top part (O_2 side) of the electrode. Additionally, the results show that the entire electrode is not completely utilized and therefore there is a disadvantages to having thicker electrodes. Therefore, use of thinner electrodes (~1/5 of current thickness) should lead to greater coverage and more effective utilization of the electrode. However for better understanding, a detailed study on the effect of capacity versus the thickness of the electrode could also be interesting.

Table B1 – Assuming uniform deposition of the Li_2O_2 discharge product, the expected capacity can be calculated based from BET surface area. The expected capacity is determined from the $2e^-$ per Li_2O_2 unit formula.

Mass of electrode:	1.2	mg	**Li_2O_2 thickness (nm):**	**Li_2O_2 (mol)**	**Expected capacity (mAh)**
BET surface area:	230	$m^2\ g^{-1}$	1	1.39E-05	0.744863994
Density of Li_2O_2:	2.31	$g\ cm^{-3}$	2	2.78E-05	1.489727988
Li_2O_2 molar mass	45.881	$g\ mol^{-1}$	3	4.17E-05	2.234591982

Faraday constant	96485.33	C mol^{-1}	4	5.56E-05	2.979455976
			5	6.95E-05	3.72431997
			6	8.34E-05	4.469183964
			7	9.73E-05	5.214047958
			8	0.000111	5.958911952
			9	0.000125	6.703775946
			10	0.000139	7.44863994

Table B2 – Assuming uniform deposition of the Li_2O_2 discharge product in the top 20% of the electrode, the expected capacity can be calculated based from BET surface area. The expected capacity is determined from the $2e^-$ per Li_2O_2 unit formula.

Mass of electrode:	0.3	mg	**Li_2O_2 thickness (nm):**	**Li_2O_2 (mol)**	**Expected capacity (mAh)**
BET surface area:	230	$m^2\ g^{-1}$	10	2.77919E-05	1.489727988
Density of Li_2O_2:	2.31	g cm^{-3}	15	4.16878E-05	2.234591982
Li_2O_2 molar mass	45.881	g mol^{-1}	20	5.55838E-05	2.979455976
Faraday constant	96485.33	C mol^{-1}	30	8.33757E-05	4.469183964
			35	9.72716E-05	5.214047958
			40	0.000111168	5.958911952
			45	0.000125064	6.703775946
			50	0.000138959	7.44863994

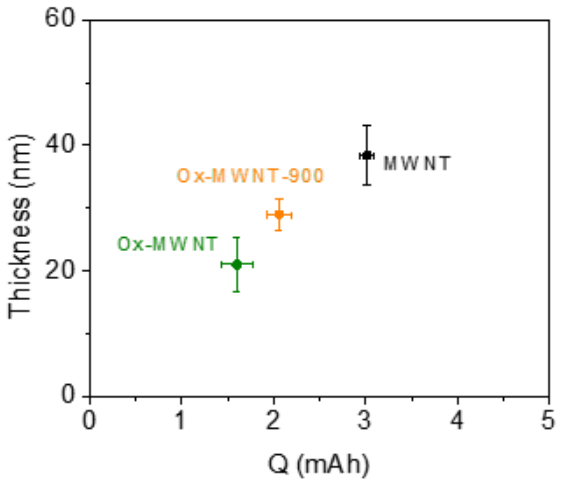

Figure B1 - Thickness and capacity plots taken from the experimentally observed values. The thickness includes the radius of the carbon nanotube which is ~10 nm. The thickness of G-MWNT is not included due to its heavier aggreggation and appears to be greater than 60 nm in the areas where thickness can be measured, ascribed to the greater observed difference when the solvation-based mechanism is more heavily biased.

Apendix C

Appendix contains suplementary Figures C1-C5 for Chapter 4.

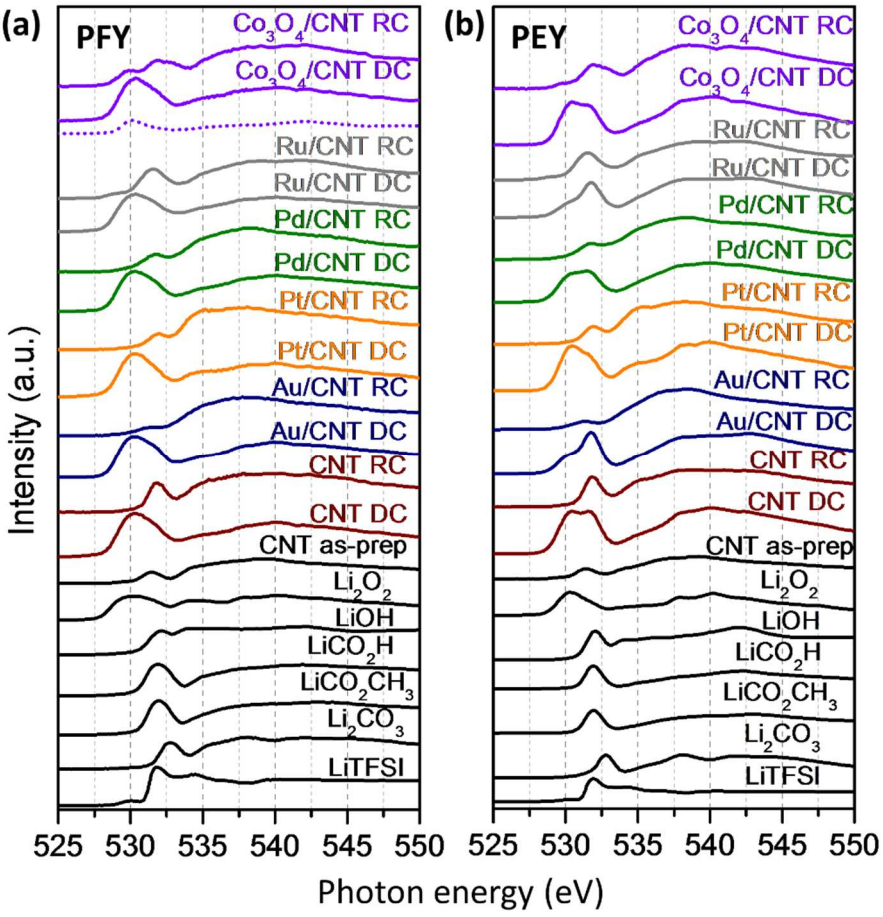

Figure C1 – O K-edge XANES with PFY and PEY modes. The plot is identical to Figure 4.3 except with the spectra separated. The dotted spectra in for Co_3O_4/CNT in the PFY mode is the as prepared electrode.

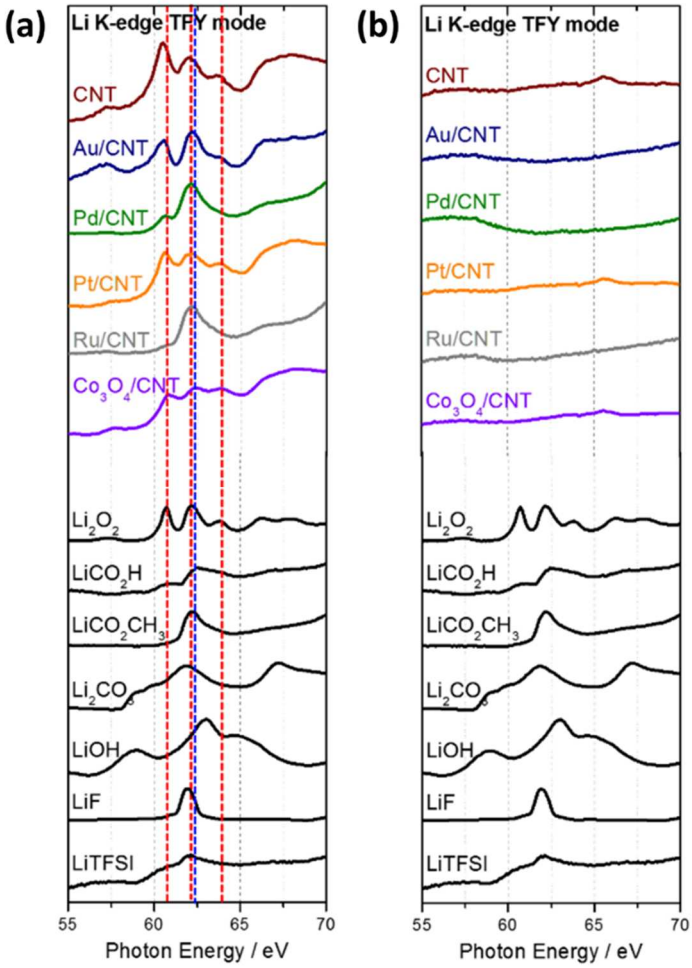

Figure C2 – Li K-edge XANES of CNT and M(O)/CNT (a) DC electrodes (b) RC electrodes. The dashed vertical lines are guides to indicate spectra features associated with (red) Li_2O_2 and (blue) Li carboxylates. These are TFY mode spectra.

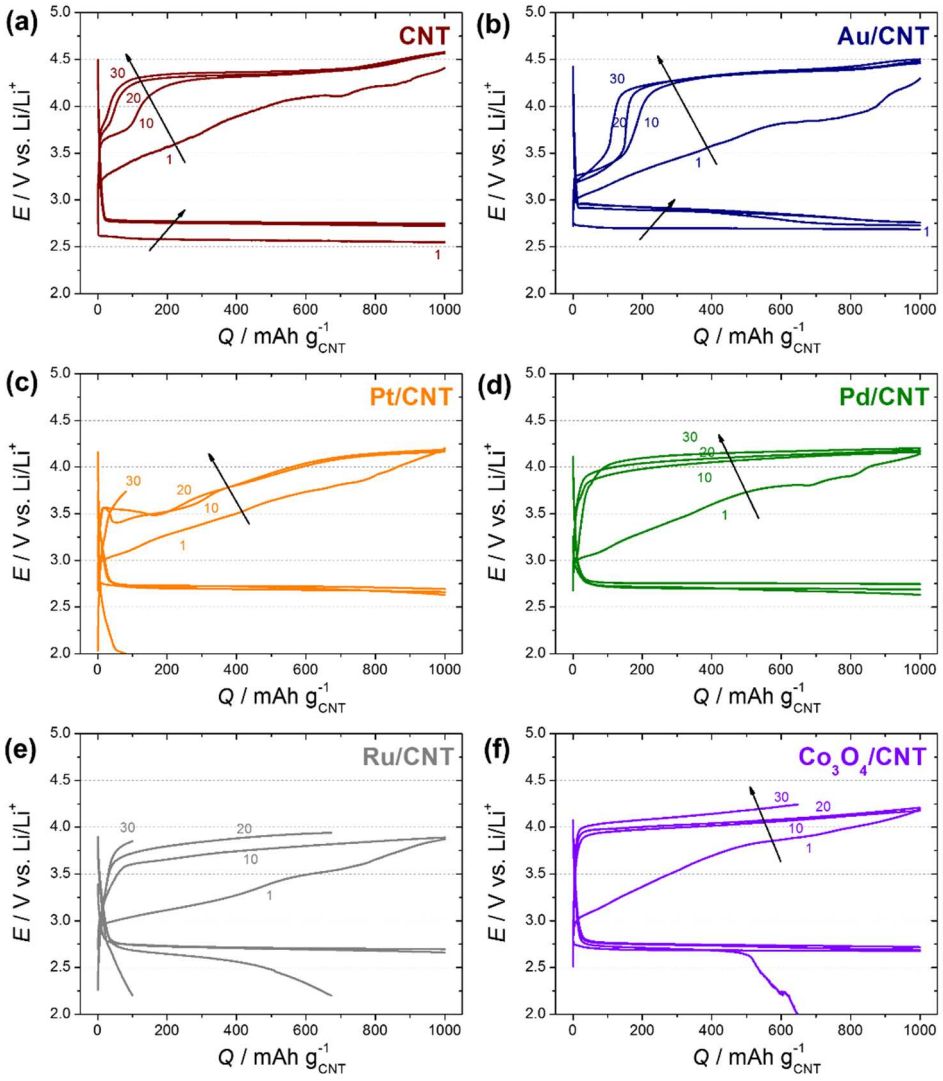

Figure C3 – Galvanostatic (constant current) DC-RC cycling performed with 0.5 M LiTFSI/tetraglyme at current density of 50 mA g^{-1}_{CNT} the fixed capacity of 1000 mAh g^{-1}_{CNT} and then RC to the equivalent DC capacity. The voltage-time plots are presented in Figure 4.11.

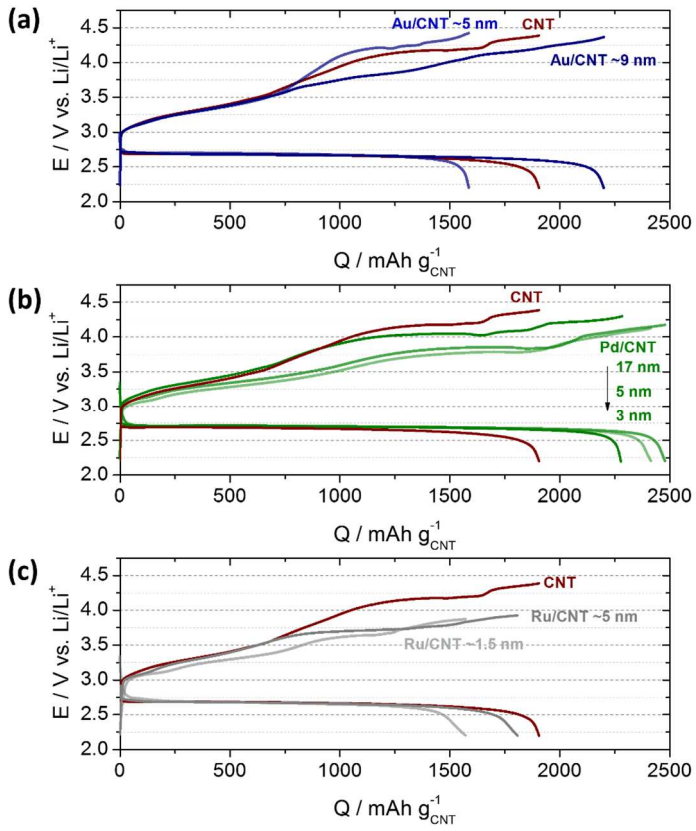

Figure C4 – DC-RC profiles with the DC cutoff condition at 2.2 V with the modulation of particle size along with the comparison with CNT (a) Au/CNT (b) Pd/CNT and (c) Ru/CNT performed 0.5 M LiTFSI/tetraglyme at 50 mA g^{-1}_{CNT}.

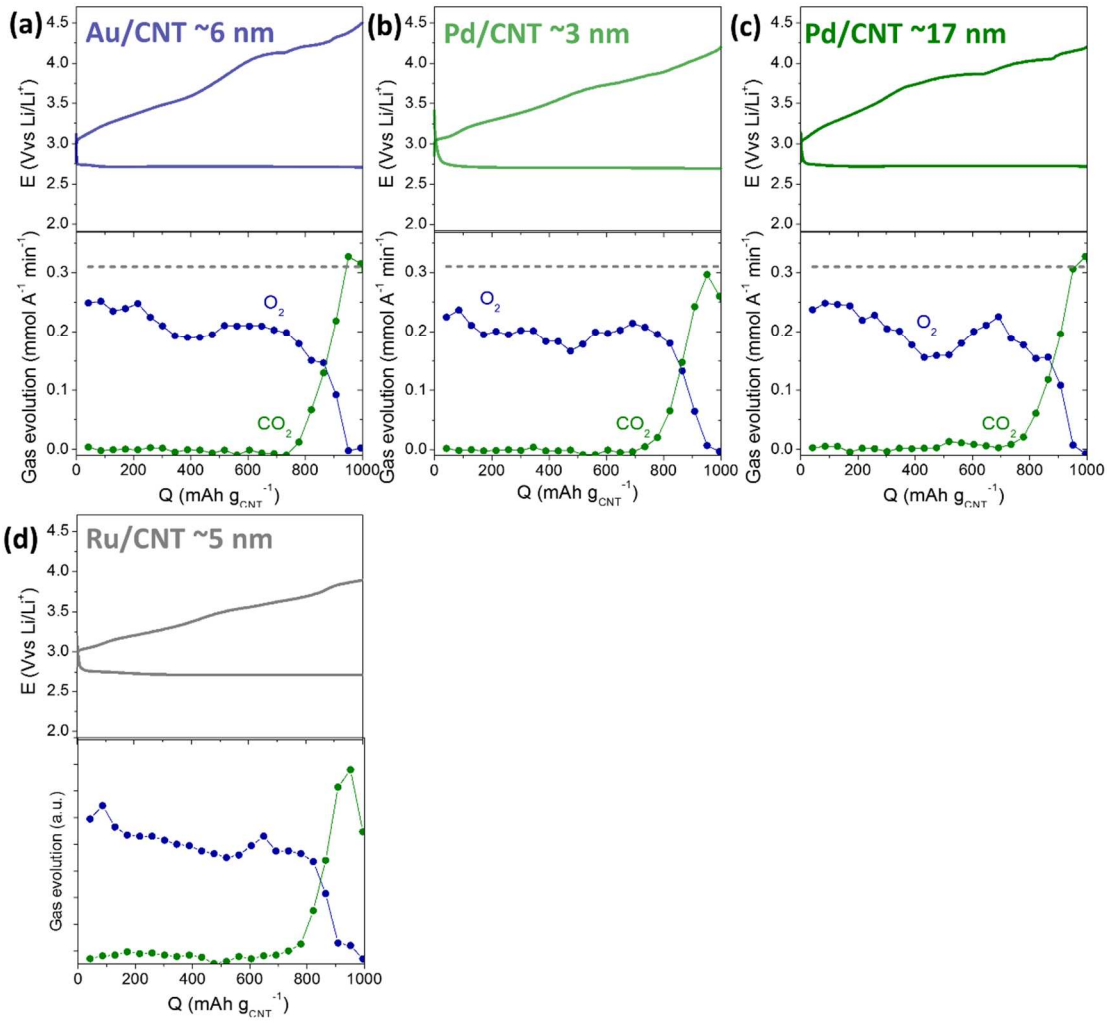

Figure C5 – In situ OEMS showing DC-RC profiles along with gas evolution rates for the different M(O)/CNT NP sizes (a) Au/CNT (b-c) Pd/CNT (d) Ru/CNT performed with 0.5 M LiTFSI/tetraglyme at 50 mA g^{-1}_{CNT}. Note that the gas evolution rates in (d) is the qualitative spectra.

.

References

Chapter 1 references

(1) Chu, S.; Majumdar, A. *Nature* **2012**, *488*, 294.

(2) Larcher, D.; Tarascon, J. *Nat. Chem.* **2015**, *7*, 19.

(3) Schiermeier, Q. *Nature* **2012**, *491*, 656.

(4) Jacquet, J.; Jamieson, D. *Nat. Clim. Change* **2016**, *6*, 643.

(5) Peters, G. P. *Nat. Clim. Change* **2016**.

(6) Wang, K.; Jiang, K.; Chung, B.; Ouchi, T.; Burke, P. J.; Boysen, D. A.; Bradwell, D. J.; Kim, H.; Muecke, U.; Sadoway, D. R. *Nature* **2014**, *514*, 348.

(7) Published Online: JCCCA. http://www.jccca.org/trend_japan/state/.

(8) https://www.epa.gov/ghgemissions/sources-greenhouse-gas-emissions.

(9) Armand, M.; Tarascon, J.-M. *Nature* **2008**, *451*, 652.

(10) Bard, A. J.; Faulkner, L. R. *Electrochemical methods: fundamentals and applications*; Wiley New York, 2001; Vol. 2.

(11) Adelhelm, P.; Hartmann, P.; Bender, C. L.; Busche, M.; Eufinger, C.; Janek, J. *Beilstein J. of Nanotech.* **2015**, *6*, 1016.

(12) Gallagher, K. G.; Goebel, S.; Greszler, T.; Mathias, M.; Oelerich, W.; Eroglu, D.; Srinivasan, V. *Energy Environ. Sci.* **2014**, *7*, 1555.

(13) Published Online: 2014. http://insideevs.com/toyota-continues-move-forward-solid-state-battery-developments/.

(14) Abraham, K.; Jiang, Z. *J. Electrochem. Soc.* **1996**, *143*, 1.

(15) Girishkumar, G.; McCloskey, B.; Luntz, A.; Swanson, S.; Wilcke, W. *J. Chem. Phys. Lett.* **2010**, *1*, 2193.

(16) Lu, J.; Li, L.; Park, J.-B.; Sun, Y.-K.; Wu, F.; Amine, K. *Chem. Rev.* **2014**, *114*, 5611.

(17) Luntz, A. C.; McCloskey, B. D. *Chem. Rev.* **2014**, *114*, 11721.

(18) Sapunkov, O.; Pande, V.; Khetan, A.; Choomwattana, C.; Viswanathan, V. *Trans. Mater. Res.* **2015**, *2*, 045002.

(19) McCloskey, B. D.; Scheffler, R.; Speidel, A.; Girishkumar, G.; Luntz, A. C. *J. Phys. Chem. C.* **2012**, *116*, 23897.

(20) Kraytsberg, A.; Ein-Eli, Y. *J. Power Sources* **2011**, *196*, 886.

(21) Sánchez-Sánchez, C. M.; Bard, A. J. *Anal. Chem* **2009**, *81*, 8094.

(22) Amanchukwu, C. V.; Chang, H.-H.; Gauthier, M.; Feng, S.; Batcho, T. P.; Hammond, P. T. *Chem. Mater.* **2016**.

(23) Lu, J.; Lee, Y. J.; Luo, X.; Lau, K. C.; Asadi, M.; Wang, H.-H.; Brombosz, S.; Wen, J.; Zhai, D.; Chen, Z. *Nature* **2016**.

(24) Lu, Y.-C.; Gallant, B. M.; Kwabi, D. G.; Harding, J. R.; Mitchell, R. R.; Whittingham, M. S.; Shao-Horn, Y. *Energy Environ. Sci.* **2013**, *6*, 750.

(25) McCloskey, B. D.; Bethune, D. S.; Shelby, R. M.; Girishkumar, G.; Luntz, A. C. *J. Chem. Phys. Lett.* **2011**, *2*, 1161.

(26) McCloskey, B. D.; Scheffler, R.; Speidel, A.; Bethune, D. S.; Shelby, R. M.; Luntz, A. *J. Am. Chem. Soc.* **2011**, *133*, 18038.

(27) Aurbach, D.; McCloskey, B. D.; Nazar, L. F.; Bruce, P. G. *Nat. Energy* **2016**, *1*, 16128.

(28) McCloskey, B. D.; Burke, C. M.; Nichols, J. E.; Renfrew, S. E. *Chem. Commun.* **2015**, *51*, 12701.

(29) Yu, Q.; Ye, S. *J. Phys. Chem. C* **2015**, *119*, 12236.

(30) Peng, Z.; Freunberger, S. A.; Hardwick, L. J.; Chen, Y.; Giordani, V.; Bardé, F.; Novák, P.; Graham, D.; Tarascon, J. M.; Bruce, P. G. *Angew. Chem. Int. Ed.* **2011**, *123*, 6475.

(31) Ren, X.; Wu, Y. *J. Am. Chem. Soc.* **2013**, *135*, 2923.

(32) Hartmann, P.; Bender, C. L.; Vračar, M.; Dürr, A. K.; Garsuch, A.; Janek, J.; Adelhelm, P. *Nat. Mater.* **2013**, *12*, 228.

(33) Laoire, C. O.; Mukerjee, S.; Abraham, K. M.; Plichta, E. J.; Hendrickson, M. A. *J. Phys. Chem. C.* **2010**, *114*, 9178.

(34) Johnson, L.; Li, C.; Liu, Z.; Chen, Y.; Freunberger, S. A.; Ashok, P. C.; Praveen, B. B.; Dholakia, K.; Tarascon, J.-M.; Bruce, P. G. *Nat. Chem.* **2014**, *6*, 1091.

(35) Burke, C. M.; Pande, V.; Khetan, A.; Viswanathan, V.; McCloskey, B. D. *Proc. Natl. Acad. Sci. U. S. A.* **2015**, *112*, 9293.

(36) Yang, C.; Wong, R. A.; Hong, M.; Yamanaka, K.; Ohta, T.; Byon, H. R. *Nano Lett.* **2016**, *16*, 2969.

(37) Wong, R. A.; Dutta, A.; Yang, C.; Yamanaka, K.; Ohta, T.; Nakao, A.; Waki, K.; Byon, H. R. *Chem. Mater.* **2016**, *28*, 8006.

(38) Adams, B. D.; Radtke, C.; Black, R.; Trudeau, M. L.; Zaghib, K.; Nazar, L. F. *Energy Environ. Sci.* **2013**, *6*, 1772.

(39) Aetukuri, N. B.; McCloskey, B. D.; García, J. M.; Krupp, L. E.; Viswanathan, V.; Luntz, A. C. *Nat. Chem.* **2015**, *7*, 50.

(40) Sharon, D.; Hirsberg, D.; Salama, M.; Afri, M.; Frimer, A. A.; Noked, M.; Kwak, W.; Sun, Y.-K.; Aurbach, D. *ACS Appl. Mater. Interfaces* **2016**, *8*, 5300.

(41) Yilmaz, E.; Yogi, C.; Yamanaka, K.; Ohta, T.; Byon, H. R. *Nano Lett.* **2013**, *13*, 4679.

(42) Xu, Y.; Shelton, W. A. *J. Electrochem. Soc.* **2011**, *158*, A1177.

(43) Gallant, B. M.; Kwabi, D. G.; Mitchell, R. R.; Zhou, J.; Thompson, C. V.; Shao-Horn, Y. *Energy Environ. Sci.* **2013**, *6*, 2518.

(44) Ottakam Thotiyl, M. M.; Freunberger, S. A.; Peng, Z.; Bruce, P. G. *J. Am. Chem. Soc.* **2012**, *135*, 494.

(45) McCloskey, B. D.; Valery, A.; Luntz, A. C.; Gowda, S. R.; Wallraff, G. M.; Garcia, J. M.; Mori, T.; Krupp, L. E. *J. Phys. Chem. Lett.* **2013**, *4*, 2989.

(46) Zhang, Y.; Cui, Q.; Zhang, X.; McKee, W. C.; Xu, Y.; Ling, S.; Li, H.; Zhong, G.; Yang, Y.; Peng, Z. *Angew. Chem. Int. Ed.* **2016**.

(47) McCloskey, B. D.; Speidel, A.; Scheffler, R.; Miller, D. C.; Viswanathan, V.; Hummelshøj, J. S.; Nørskov, J. K.; Luntz, A. C. *J. Phys. Chem. Lett.* **2012**, *3*, 997.

(48) Gao, X.; Chen, Y.; Johnson, L.; Bruce, P. G. *Nat. Mater.* **2016**.

(49) Tian, F.; Radin, M. D.; Siegel, D. J. *Chem. Mater.* **2014**, *26*, 2952.

(50) Wandt, J.; Jakes, P.; Granwehr, J.; Gasteiger, H. A.; Eichel, R. A. *Angew. Chem.* **2016**, *128*, 7006.

(51) McCloskey, B. D.; Bethune, D. S.; Shelby, R. M.; Mori, T.; Scheffler, R.; Speidel, A.; Sherwood, M.; Luntz, A. C. *J. Phys. Chem. Lett.* **2012**, *3*, 3043.

(52) Kang, S.; Mo, Y.; Ong, S. P.; Ceder, G. *Chem. Mater.* **2013**, *25*, 3328.

(53) Lu, Y.-C.; Shao-Horn, Y. *J. Phys. Chem. Lett.* **2012**, *4*, 93.

(54) Freunberger, S. A.; Chen, Y.; Bardé, F.; Takechi, K.; Mizuno, F.; Bruce, P. G. In *The Lithium Air Battery*; Springer: 2014, p 23.

(55) Goodenough, J. B.; Park, K.-S. *J. Am. Chem. Soc.* **2013**, *135*, 1167.

(56) Freunberger, S. A.; Chen, Y.; Peng, Z.; Griffin, J. M.; Hardwick, L. J.; Bardé, F.; Novák, P.; Bruce, P. G. *J. Am. Chem. Soc.* **2011**, *133*, 8040.

(57) Adams, B. D.; Black, R.; Williams, Z.; Fernandes, R.; Cuisinier, M.; Berg, E. J.; Novak, P.; Murphy, G. K.; Nazar, L. F. *Adv. Energy Mater.* **2015**, *5*.

(58) Kumar, N.; Radin, M. D.; Wood, B. C.; Ogitsu, T.; Siegel, D. J. *J. phys. Chem. C* **2015**, *119*, 9050.

(59) Khetan, A.; Pitsch, H.; Viswanathan, V. *J. Phys. Chem. Lett.* **2014**, *5*, 1318.

(60) Bryantsev, V. S.; Uddin, J.; Giordani, V.; Walker, W.; Addison, D.; Chase, G. V. *J. Electrochem. Soc.* **2013**, *160*, A160.

(61) Bryantsev, V. S.; Giordani, V.; Walker, W.; Blanco, M.; Zecevic, S.; Sasaki, K.; Uddin, J.; Addison, D.; Chase, G. V. *J. Phys. Chem. A* **2011**, *115*, 12399.

(62) Schwenke, K. U.; Meini, S.; Wu, X.; Gasteiger, H. A.; Piana, M. *Phys. Chem. Chem. Phys.* **2013**, *15*, 11830.

(63) Takechi, K.; Higashi, S.; Mizuno, F.; Nishikoori, H.; Iba, H.; Shiga, T. *ECS Electrochem. Lett.* **2012**, *1*, A27.

(64) Freunberger, S. A.; Chen, Y.; Drewett, N. E.; Hardwick, L. J.; Bardé, F.; Bruce, P. G. *Angew. Chem. Int. Ed.* **2011**, *50*, 8609.

(65) Hong, M.; Choi, H. C.; Byon, H. R. *Chem. Mater.* **2015**, *27*, 2234.

(66) Giordani, V.; Tozier, D.; Tan, H.; Burke, C. M.; Gallant, B. M.; Uddin, J.; Greer, J. R.; McCloskey, B. D.; Chase, G. V.; Addison, D. *J. Am. Chem. Soc.* **2016**, *138*, 2656.

(67) Black, R.; Lee, J. H.; Adams, B.; Mims, C. A.; Nazar, L. F. *Angew. Chem. Int. Ed.* **2013**, *125*, 410.

(68) Lim, H.-D.; Lee, B.; Zheng, Y.; Hong, J.; Kim, J.; Gwon, H.; Ko, Y.; Lee, M.; Cho, K.; Kang, K. *Nat. Energy* **2016**, *1*, 16066.

(69) Burke, C. M.; Black, R.; Kochetkov, I. R.; Giordani, V.; Addison, D.; Nazar, L. F.; McCloskey, B. D. *ACS Energy Lett.* **2016**, *1*, 747.

(70) Viswanathan, V.; Thygesen, K. S.; Hummelshøj, J.; Nørskov, J. K.; Girishkumar, G.; McCloskey, B.; Luntz, A. *J. Chem. Phys.* **2011**, *135*, 214704.

(71) Radin, M. D.; Siegel, D. J. *Energy Environ. Sci.* **2013**, *6*, 2370.

(72) Liang, Z.; Lu, Y.-C. *J. Am. Chem. Soc.* **2016**, *138*, 7574.

(73) Schwenke, K. U.; Metzger, M.; Restle, T.; Piana, M.; Gasteiger, H. A. *J. Electrochem. Soc.* **2015**, *162*, A573.

(74) Gowda, S.; Brunet, A.; Wallraff, G.; McCloskey, B. *J. Phys. Chem. Lett.* **2012**, *4*, 276.

(75) Thomas, M. L.; Oda, Y.; Tatara, R.; Kwon, H. M.; Ueno, K.; Dokko, K.; Watanabe, M. *Adv. Energy Mater.* **2016**.

(76) Xu, W.; Wang, J.; Ding, F.; Chen, X.; Nasybulin, E.; Zhang, Y.; Zhang, J.-G. *Energy Environ. Sci.* **2014**, *7*, 513.

(77) Liu, Y.; Lin, D.; Yuen, P. Y.; Liu, K.; Xie, J.; Dauskardt, R. H.; Cui, Y. *Adv. Mater.* **2016**.

Chapter 2 references

(1) Yilmaz, E.; Yogi, C.; Yamanaka, K.; Ohta, T.; Byon, H. R. *Nano Lett.* **2013**, *13*, 4679.

(2) Hong, M.; Choi, H. C.; Byon, H. R. *Chem. Mater.* **2015**, *27*, 2234.

(3) McCloskey, B. D.; Scheffler, R.; Speidel, A.; Girishkumar, G.; Luntz, A. C. *J. Phys. Chem. C.* **2012**, *116*, 23897.

(4) Schwenke, K. U.; Meini, S.; Wu, X.; Gasteiger, H. A.; Piana, M. *Phys. Chem. Chem. Phys.* **2013**, *15*, 11830.

(5) Black, R.; Oh, S. H.; Lee, J.-H.; Yim, T.; Adams, B.; Nazar, L. F. *J. Am. Chem. Soc.* **2012**, *134*, 2902.

(6) Kwabi, D. G.; Batcho, T. P.; Amanchukwu, C. V.; Ortiz-Vitoriano, N.; Hammond, P.; Thompson, C. V.; Shao-Horn, Y. *J. Phys. Chem. Lett.* **2014**, *5*, 2850.

(7) McCloskey, B. D.; Burke, C. M.; Nichols, J. E.; Renfrew, S. E. *Chem. Commun.* **2015**, *51*, 12701.

(8) Li, F.; Zhang, T.; Zhou, H. *Energy Environ. Sci.* **2013**, *6*, 1125.

(9) Laoire, C. O.; Mukerjee, S.; Abraham, K. M.; Plichta, E. J.; Hendrickson, M. A. *J. Phys. Chem. C.* **2010**, *114*, 9178.

(10) Younesi, R.; Veith, G. M.; Johansson, P.; Edström, K.; Vegge, T. *Energy Environ. Sci.* **2015**, *8*, 1905.

(11) Wong, R. A.; Dutta, A.; Yang, C.; Yamanaka, K.; Ohta, T.; Nakao, A.; Waki, K.; Byon, H. R. *Chem. Mater.* **2016**, *28*, 8006.

(12) Thomas, M. L.; Yamanaka, K.; Ohta, T.; Byon, H. R. *Chem. Commun.* **2015**, *51*, 3977.

(13) Nasybulin, E.; Xu, W.; Engelhard, M. H.; Nie, Z.; Li, X. S.; Zhang, J.-G. *J. Power Sources* **2013**, *243*, 899.

(14) Yang, C.; Wong, R. A.; Hong, M.; Yamanaka, K.; Ohta, T.; Byon, H. R. *Nano Lett.* **2016**, *16*, 2969.

(15) Kwabi, D. G.; Tułodziecki, M.; Pour, N.; Itkis, D. M.; Thompson, C. V.; Shao-Horn, Y. *The journal of physical chemistry letters* **2016**, *7*, 1204.

(16) Johnson, L.; Li, C.; Liu, Z.; Chen, Y.; Freunberger, S. A.; Ashok, P. C.; Praveen, B. B.; Dholakia, K.; Tarascon, J.-M.; Bruce, P. G. *Nat. Chem.* **2014**, *6*, 1091.

(17) Published Online: 2015.

(18) http://www.shimadzu.com/an/uv/support/fundamentals/structure.html.

(19) Hartmann, P.; Bender, C. L.; Sann, J.; Dürr, A. K.; Jansen, M.; Janek, J.; Adelhelm, P. *Phys. Chem. Chem. Phys.* **2013**, *15*, 11661.

(20) Højberg, J.; Knudsen, K. B.; Hjelm, J.; Vegge, T. *ECS Electrochem. Lett.* **2015**, *4*, A63.

(21) Abd-El-Latif, A.; Bondue, C.; Ernst, S.; Hegemann, M.; Kaul, J.; Khodayari, M.; Mostafa, E.; Stefanova, A.; Baltruschat, H. *Trends Anal. Chem.; TrAC* **2015**, *70*, 4.

(22) Baltruschat, H. *J. Am. Soc. Mass Spectrom.* **2004**, *15*, 1693.

(23) McCloskey, B. D.; Speidel, A.; Scheffler, R.; Miller, D. C.; Viswanathan, V.; Hummelshøj, J. S.; Nørskov, J. K.; Luntz, A. C. *J. Phys. Chem. Lett.* **2012**, *3*, 997.

(24) McCloskey, B. D.; Bethune, D. S.; Shelby, R. M.; Girishkumar, G.; Luntz, A. C. *J. Chem. Phys. Lett.* **2011**, *2*, 1161.

(25) Girishkumar, G.; McCloskey, B.; Luntz, A.; Swanson, S.; Wilcke, W. *J. Chem. Phys. Lett.* **2010**, *1*, 2193.

(26) McCloskey, B. D.; Bethune, D. S.; Shelby, R. M.; Mori, T.; Scheffler, R.; Speidel, A.; Sherwood, M.; Luntz, A. C. *J. Phys. Chem. Lett.* **2012**, *3*, 3043.

(27) Luntz, A. C.; McCloskey, B. D. *Chem. Rev.* **2014**, *114*, 11721.

(28) Tsiouvaras, N.; Meini, S.; Buchberger, I.; Gasteiger, H. *Journal of The Electrochemical Society* **2013**, *160*, A471.

(29) Meini, S.; Tsiouvaras, N.; Schwenke, K. U.; Piana, M.; Beyer, H.; Lange, L.; Gasteiger, H. A. *Phys. Chem. Chem. Phys.* **2013**, *15*, 11478.

(30) Adams, B. D.; Black, R.; Radtke, C.; Williams, Z.; Mehdi, B. L.; Browning, N. D.; Nazar, L. F. *ACS nano* **2014**, *8*, 12483.

(31) Adams, B. D.; Black, R.; Williams, Z.; Fernandes, R.; Cuisinier, M.; Berg, E. J.; Novak, P.; Murphy, G. K.; Nazar, L. F. *Adv. Energy Mater.* **2015**, *5*.

(32) RGA User's manual for SRS 100,200 and 300 amu. [Online Early Access]. http://www.thinksrs.com/products/RGA.htm.

Chapter 3 references

(1) Bruce, P. G.; Freunberger, S. A.; Hardwick, L. J.; Tarascon, J.-M. *Nat. Mater.* **2012**, *11*, 19.

(2) Luntz, A. C.; McCloskey, B. D. *Chem. Rev.* **2014**, *114*, 11721.

(3) McCloskey, B. D.; Burke, C. M.; Nichols, J. E.; Renfrew, S. E. *Chem. Commun.* **2015**, *51*, 12701.

(4) Lu, Y.-C.; Gallant, B. M.; Kwabi, D. G.; Harding, J. R.; Mitchell, R. R.; Whittingham, M. S.; Shao-Horn, Y. *Energy Environ. Sci.* **2013**, *6*, 750.

(5) McCloskey, B. D.; Scheffler, R.; Speidel, A.; Girishkumar, G.; Luntz, A. C. *J. Phys. Chem. C.* **2012**, *116*, 23897.

(6) Itkis, D. M.; Semenenko, D. A.; Kataev, E. Y.; Belova, A. I.; Neudachina, V. S.; Sirotina, A. P.; Hävecker, M.; Teschner, D.; Knop-Gericke, A.; Dudin, P. *Nano Lett.* **2013**, *13*, 4697.

(7) McCloskey, B. D.; Valery, A.; Luntz, A. C.; Gowda, S. R.; Wallraff, G. M.; Garcia, J. M.; Mori, T.; Krupp, L. E. *J. Phys. Chem. Lett.* **2013**, *4*, 2989.

(8) McCloskey, B. D.; Bethune, D. S.; Shelby, R. M.; Girishkumar, G.; Luntz, A. C. *J. Chem. Phys. Lett.* **2011**, *2*, 1161.

(9) Bonnet-Mercier, N.; Wong, R. A.; Thomas, M. L.; Dutta, A.; Yamanaka, K.; Yogi, C.; Ohta, T.; Byon, H. R. *Sci. Rep.* **2014**, *4*, 7127.

(10) McCloskey, B. D.; Speidel, A.; Scheffler, R.; Miller, D. C.; Viswanathan, V.; Hummelshøj, J. S.; Nørskov, J. K.; Luntz, A. C. *J. Phys. Chem. Lett.* **2012**, *3*, 997.

(11) Thotiyl, M. M. O.; Freunberger, S. A.; Peng, Z.; Chen, Y.; Liu, Z.; Bruce, P. G. *Nat. Mater.* **2013**, *12*, 1050.

(12) McCloskey, B. D.; Bethune, D. S.; Shelby, R. M.; Mori, T.; Scheffler, R.; Speidel, A.; Sherwood, M.; Luntz, A. C. *J. Phys. Chem. Lett.* **2012**, *3*, 3043.

(13) Hong, M.; Choi, H. C.; Byon, H. R. *Chem. Mater.* **2015**, *27*, 2234.

(14) Lau, S.; Archer, L. A. *Nano Lett.* **2015**, *15*, 5995.

(15) Aetukuri, N. B.; McCloskey, B. D.; García, J. M.; Krupp, L. E.; Viswanathan, V.; Luntz, A. C. *Nat. Chem.* **2015**, *7*, 50.

(16) Yilmaz, E.; Yogi, C.; Yamanaka, K.; Ohta, T.; Byon, H. R. *Nano Lett.* **2013**, *13*, 4679.

(17) Kundu, S.; Wang, Y.; Xia, W.; Muhler, M. *J. Phys. Chem. C.* **2008**, *112*, 16869.

(18) Luntz, A.; Viswanathan, V.; Voss, J.; Varley, J.; Nørskov, J.; Scheffler, R.; Speidel, A. *J. Phys. Chem. Lett.* **2013**, *4*, 3494.

(19) Lu, Y.-C.; Gasteiger, H. A.; Crumlin, E.; McGuire, R.; Shao-Horn, Y. *J. Electrochem. Soc.* **2010**, *157*, A1016.

(20) Ottakam Thotiyl, M. M.; Freunberger, S. A.; Peng, Z.; Bruce, P. G. *J. Am. Chem. Soc.* **2012**, *135*, 494.

(21) Peng, Z.; Freunberger, S. A.; Chen, Y.; Bruce, P. G. *Science* **2012**, *337*, 563.

(22) Ding, N.; Chien, S. W.; Hor, T. A.; Lum, R.; Zong, Y.; Liu, Z. *J. Mater. Chem. A* **2014**, *2*, 12433.

(23) Meini, S.; Piana, M.; Beyer, H.; Schwämmlein, J.; Gasteiger, H. A. *J. Electrochem. Soc.* **2012**, *159*, A2135.

(24) Xia, G.; Shen, S.; Zhu, F.; Xie, J.; Hu, Y.; Zhu, K.; Zhang, J. *Electrochem. Commun.* **2015**, *60*, 26.

(25) Thomas, M. L.; Yamanaka, K.; Ohta, T.; Byon, H. R. *Chem. Commun.* **2015**, *51*, 3977.

(26) Larcher, D.; Tarascon, J. *Nat. Chem.* **2015**, *7*, 19.

(27) Byon, H. R.; Lee, S. W.; Chen, S.; Hammond, P. T.; Shao-Horn, Y. *Carbon* **2011**, *49*, 457.

(28) Hartmann, P.; Bender, C. L.; Sann, J.; Dürr, A. K.; Jansen, M.; Janek, J.; Adelhelm, P. *Phys. Chem. Chem. Phys.* **2013**, *15*, 11661.

(29) Schwenke, K. U.; Metzger, M.; Restle, T.; Piana, M.; Gasteiger, H. A. *J. Electrochem. Soc.* **2015**, *162*, A573.

(30) Lee, S. W.; Gallant, B. M.; Lee, Y.; Yoshida, N.; Kim, D. Y.; Yamada, Y.; Noda, S.; Yamada, A.; Shao-Horn, Y. *Energy Environ. Sci.* **2012**, *5*, 5437.

(31) Byon, H. R.; Gallant, B. M.; Lee, S. W.; Shao‐Horn, Y. *Adv. Funct. Mater.* **2013**, *23*, 1037.

(32) Waki, K.; Wong, R. A.; Oktaviano, H. S.; Fujio, T.; Nagai, T.; Kimoto, K.; Yamada, K. *Energy Environ. Sci.* **2014**, *7*, 1950.

(33) Yasuda, A.; Kawase, N.; Banhart, F.; Mizutani, W.; Shimizu, T.; Tokumoto, H. *J. Phys. Chem. B.* **2002**, *106*, 1849.

(34) Lee, S. W.; Yabuuchi, N.; Gallant, B. M.; Chen, S.; Kim, B.-S.; Hammond, P. T.; Shao-Horn, Y. *Nat. Nanotechnol.* **2010**, *5*, 531.

(35) Dresselhaus, M. S.; Jorio, A.; Hofmann, M.; Dresselhaus, G.; Saito, R. *Nano Lett.* **2010**, *10*, 751.

(36) Oktaviano, H. S.; Yamada, K.; Waki, K. *J. Mater. Chem.* **2012**, *22*, 25167.

(37) Yang, C.; Wong, R. A.; Hong, M.; Yamanaka, K.; Ohta, T.; Byon, H. R. *Nano Lett.* **2016**, *16*, 2969.

(38) Adams, B. D.; Radtke, C.; Black, R.; Trudeau, M. L.; Zaghib, K.; Nazar, L. F. *Energy Environ. Sci.* **2013**, *6*, 1772.

(39) Johnson, L.; Li, C.; Liu, Z.; Chen, Y.; Freunberger, S. A.; Ashok, P. C.; Praveen, B. B.; Dholakia, K.; Tarascon, J.-M.; Bruce, P. G. *Nat. Chem.* **2014**, *6*, 1091.

(40) Xu, Y.; Shelton, W. A. *J. Electrochem. Soc.* **2011**, *158*, A1177.

(41) Laoire, C. O.; Mukerjee, S.; Abraham, K. M.; Plichta, E. J.; Hendrickson, M. A. *J. Phys. Chem. C.* **2010**, *114*, 9178.

(42) Burke, C. M.; Pande, V.; Khetan, A.; Viswanathan, V.; McCloskey, B. D. *Proc. Natl. Acad. Sci. U. S. A.* **2015**, *112*, 9293.

(43) Wen, R.; Hong, M.; Byon, H. R. *J. Am. Chem. Soc.* **2013**, *135*, 10870.

(44) Eswaran, M.; Munichandraiah, N.; Scanlon, L. *Electrochem. Solid-State Lett.* **2010**, *13*, A121.

(45) Rinaldi, A.; Wijaya, O.; Hoster, H. E.; Yu, D. Y. *ChemSusChem* **2014**, *7*, 1283.

(46) Takagi, H. *Tanso* **2009**, *237*, 67.

(47) Zhang, Y.; Cui, Q.; Zhang, X.; McKee, W. C.; Xu, Y.; Ling, S.; Li, H.; Zhong, G.; Yang, Y.; Peng, Z. *Angew. Chem. Int. Ed.* **2016**.

(48) Tian, F.; Radin, M. D.; Siegel, D. J. *Chem. Mater.* **2014**, *26*, 2952.

(49) Kang, S.; Mo, Y.; Ong, S. P.; Ceder, G. *Chem. Mater.* **2013**, *25*, 3328.

(50) Radin, M. D.; Siegel, D. J. *Energy Environ. Sci.* **2013**, *6*, 2370.

(51) Lu, Y.-C.; Shao-Horn, Y. *J. Phys. Chem. Lett.* **2012**, *4*, 93.

(52) Li, F.; Tang, D.-M.; Chen, Y.; Golberg, D.; Kitaura, H.; Zhang, T.; Yamada, A.; Zhou, H. *Nano Lett.* **2013**, *13*, 4702.

Chapter 4 references

(1) Aurbach, D.; McCloskey, B. D.; Nazar, L. F.; Bruce, P. G. *Nat. Energy* **2016**, *1*, 16128.

(2) Sapunkov, O.; Pande, V.; Khetan, A.; Choomwattana, C.; Viswanathan, V. *Trans. Mater. Res.* **2015**, *2*, 045002.

(3) Luntz, A. C.; McCloskey, B. D. *Chem. Rev.* **2014**, *114*, 11721.

(4) McCloskey, B. D.; Scheffler, R.; Speidel, A.; Girishkumar, G.; Luntz, A. C. *J. Phys. Chem. C.* **2012**, *116*, 23897.

(5) Lu, Y.-C.; Gallant, B. M.; Kwabi, D. G.; Harding, J. R.; Mitchell, R. R.; Whittingham, M. S.; Shao-Horn, Y. *Energy Environ. Sci.* **2013**, *6*, 750.

(6) McCloskey, B. D.; Burke, C. M.; Nichols, J. E.; Renfrew, S. E. *Chem. Commun.* **2015**, *51*, 12701.

(7) Amanchukwu, C. V.; Harding, J. R.; Shao-Horn, Y.; Hammond, P. T. *Chem. Mater.* **2015**, *27*, 550.

(8) Kumar, N.; Radin, M. D.; Wood, B. C.; Ogitsu, T.; Siegel, D. J. *J. phys. Chem. C* **2015**, *119*, 9050.

(9) McCloskey, B. D.; Valery, A.; Luntz, A. C.; Gowda, S. R.; Wallraff, G. M.; Garcia, J. M.; Mori, T.; Krupp, L. E. *J. Phys. Chem. Lett.* **2013**, *4*, 2989.

(10) McCloskey, B. D.; Speidel, A.; Scheffler, R.; Miller, D. C.; Viswanathan, V.; Hummelshøj, J. S.; Nørskov, J. K.; Luntz, A. C. *J. Phys. Chem. Lett.* **2012**, *3*, 997.

(11) Hong, M.; Choi, H. C.; Byon, H. R. *Chem. Mater.* **2015**, *27*, 2234.

(12) Black, R.; Lee, J. H.; Adams, B.; Mims, C. A.; Nazar, L. F. *Angew. Chem. Int. Ed.* **2013**, *125*, 410.

(13) McCloskey, B. D.; Scheffler, R.; Speidel, A.; Bethune, D. S.; Shelby, R. M.; Luntz, A. *J. Am. Chem. Soc.* **2011**, *133*, 18038.

(14) Yao, K. P.; Risch, M.; Sayed, S. Y.; Lee, Y.-L.; Harding, J. R.; Grimaud, A.; Pour, N.; Xu, Z.; Zhou, J.; Mansour, A. *Energy Environ. Sci.* **2015**, *8*, 2417.

(15) Jung, H.-G.; Jeong, Y. S.; Park, J.-B.; Sun, Y.-K.; Scrosati, B.; Lee, Y. J. *Acs Nano* **2013**, *7*, 3532.

(16) Li, F.; Chen, Y.; Tang, D.-M.; Jian, Z.; Liu, C.; Golberg, D.; Yamada, A.; Zhou, H. *Energy Environ. Sci.* **2014**, *7*, 1648.

(17) Jana, N. R.; Gearheart, L.; Murphy, C. J. *Langmuir* **2001**, *17*, 6782.

(18) Jana, N. R.; Gearheart, L.; Murphy, C. J. *Advanced Materials* **2001**, *13*, 1389.

(19) Ji, X.; Song, X.; Li, J.; Bai, Y.; Yang, W.; Peng, X. *Journal of the American Chemical Society* **2007**, *129*, 13939.

(20) Gao, D.; Zhou, H.; Wang, J.; Miao, S.; Yang, F.; Wang, G.; Wang, J.; Bao, X. *Journal of the American Chemical Society* **2015**, *137*, 4288.

(21) Viau, G.; Brayner, R.; Poul, L.; Chakroune, N.; Lacaze, E.; Fiévet-Vincent, F.; Fiévet, F. *Chemistry of Materials* **2003**, *15*, 486.

(22) Yamada, Y.; Yano, K.; Xu, Q.; Fukuzumi, S. *The Journal of Physical Chemistry C* **2010**, *114*, 16456.

(23) Itkis, D. M.; Semenenko, D. A.; Kataev, E. Y.; Belova, A. I.; Neudachina, V. S.; Sirotina, A. P.; Hävecker, M.; Teschner, D.; Knop-Gericke, A.; Dudin, P. *Nano Lett.* **2013**, *13*, 4697.

(24) Harding, J. R.; Lu, Y.-C.; Tsukada, Y.; Shao-Horn, Y. *Phys. Chem. Chem. Phys.* **2012**, *14*, 10540.

(25) Lu, Y.-C.; Gasteiger, H. A.; Crumlin, E.; McGuire, R.; Shao-Horn, Y. *J. Electrochem. Soc.* **2010**, *157*, A1016.

(26) Jeong, Y. S.; Park, J.-B.; Jung, H.-G.; Kim, J.; Luo, X.; Lu, J.; Curtiss, L.; Amine, K.; Sun, Y.-K.; Scrosati, B. *Nano Lett.* **2015**, *15*, 4261.

(27) Lu, Y.-C.; Gasteiger, H. A.; Shao-Horn, Y. *J. Am. Chem. Soc.* **2011**, *133*, 19048.

(28) Yilmaz, E.; Yogi, C.; Yamanaka, K.; Ohta, T.; Byon, H. R. *Nano Lett.* **2013**, *13*, 4679.

(29) McCloskey, B. D.; Bethune, D. S.; Shelby, R. M.; Mori, T.; Scheffler, R.; Speidel, A.; Sherwood, M.; Luntz, A. C. *J. Phys. Chem. Lett.* **2012**, *3*, 3043.

(30) Freunberger, S. A.; Chen, Y.; Drewett, N. E.; Hardwick, L. J.; Bardé, F.; Bruce, P. G. *Angew. Chem. Int. Ed.* **2011**, *50*, 8609.

(31) Wong, R. A.; Dutta, A.; Yang, C.; Yamanaka, K.; Ohta, T.; Nakao, A.; Waki, K.; Byon, H. R. *Chem. Mater.* **2016**, *28*, 8006.

(32) Tan, P.; Wei, Z.; Shyy, W.; Zhao, T.; Zhu, X. *Energy Environ. Sci.* **2016**, *9*, 1783.

(33) Bondue, C.; Reinsberg, P.; Abd-El-Latif, A.; Baltruschat, H. *Physical Chemistry Chemical Physics* **2015**, *17*, 25593.

(34) Radin, M. D.; Monroe, C. W.; Siegel, D. J. *Chem. Mater.* **2015**, *27*, 839.

(35) Meini, S.; Solchenbach, S.; Piana, M.; Gasteiger, H. A. *J. Electrochem. Soc.* **2014**, *161*, A1306.

(36) Laoire, C. O.; Mukerjee, S.; Abraham, K. M.; Plichta, E. J.; Hendrickson, M. A. *J. Phys. Chem. C.* **2010**, *114*, 9178.

(37) Younesi, R.; Veith, G. M.; Johansson, P.; Edström, K.; Vegge, T. *Energy Environ. Sci.* **2015**, *8*, 1905.

(38) Yang, C.; Wong, R. A.; Hong, M.; Yamanaka, K.; Ohta, T.; Byon, H. R. *Nano Lett.* **2016**, *16*, 2969.

(39) Johnson, L.; Li, C.; Liu, Z.; Chen, Y.; Freunberger, S. A.; Ashok, P. C.; Praveen, B. B.; Dholakia, K.; Tarascon, J.-M.; Bruce, P. G. *Nat. Chem.* **2014**, *6*, 1091.

(40) Geng, W.; Ohno, T. *J. Phys. Chem. C* **2015**, *119*, 1024.

(41) Shi, L.; Zhao, T.; Xu, A.; Wei, Z. *ACS Catal.* **2016**, *6*, 6285.

(42) Zhang, Y.; Cui, Q.; Zhang, X.; McKee, W. C.; Xu, Y.; Ling, S.; Li, H.; Zhong, G.; Yang, Y.; Peng, Z. *Angew. Chem. Int. Ed.* **2016**.

(43) Tian, F.; Radin, M. D.; Siegel, D. J. *Chem. Mater.* **2014**, *26*, 2952.

(44) Dathar, G. K. P.; Shelton, W. A.; Xu, Y. *J. Chem. Phys. Lett.* **2012**, *3*, 891.

Chapter 5 references

(1) Wandt, J.; Jakes, P.; Granwehr, J.; Gasteiger, H. A.; Eichel, R. A. *Angew. Chem.* **2016**, *128*, 7006.

(2) Bergner, B. J.; Schürmann, A.; Peppler, K.; Garsuch, A.; Janek, J. r. *J. Am. Chem. Soc.* **2014**, *136*, 15054.

(3) Adams, B. D.; Black, R.; Williams, Z.; Fernandes, R.; Cuisinier, M.; Berg, E. J.; Novak, P.; Murphy, G. K.; Nazar, L. F. *Adv. Energy Mater.* **2015**, *5*.

(4) Khetan, A.; Pitsch, H.; Viswanathan, V. *J. Phys. Chem. Lett.* **2014**, *5*, 2419.

(5) Gao, X.; Chen, Y.; Johnson, L.; Bruce, P. G. *Nat. Mater.* **2016**.

(6) Giordani, V.; Tozier, D.; Tan, H.; Burke, C. M.; Gallant, B. M.; Uddin, J.; Greer, J. R.; McCloskey, B. D.; Chase, G. V.; Addison, D. *J. Am. Chem. Soc.* **2016**, *138*, 2656.

Appendix references

Appendix A

(1) McCloskey, B. D.; Garcia, J. M.; Luntz, A. C. *J. Phys. Chem. Lett.* **2014**, *5*, 1230.

(2) Hartmann, P.; Bender, C. L.; Sann, J.; Dürr, A. K.; Jansen, M.; Janek, J.; Adelhelm, P. *Phys. Chem. Chem. Phys.* **2013**, *15*, 11661.

(3) Clark, E. L.; Singh, M. R.; Kwon, Y.; Bell, A. T. *Anal. Chem.* **2015**, *87*, 8013.

Appendix B

(1) McCloskey, B. D.; Bethune, D. S.; Shelby, R. M.; Girishkumar, G.; Luntz, A. C. *J. Chem. Phys. Lett.* **2011**, *2*, 1161.

(2) McCloskey, B. D.; Valery, A.; Luntz, A. C.; Gowda, S. R.; Wallraff, G. M.; Garcia, J. M.; Mori, T.; Krupp, L. E. *J. Phys. Chem. Lett.* **2013**, *4*, 2989.

(3) Burke, C. M.; Pande, V.; Khetan, A.; Viswanathan, V.; McCloskey, B. D. *Proc. Natl. Acad. Sci. U. S. A.* **2015**, *112*, 9293.

(4) Izutsu, K. *Electrochemistry in nonaqueous solutions*; John Wiley & Sons, 2009.

(5) Laoire, C. O.; Mukerjee, S.; Abraham, K. M.; Plichta, E. J.; Hendrickson, M. A. *J. Phys. Chem. C.* **2010**, *114*, 9178.

(6) Viswanathan, V.; Thygesen, K. S.; Hummelshøj, J.; Nørskov, J. K.; Girishkumar, G.; McCloskey, B.; Luntz, A. *J. Chem. Phys.* **2011**, *135*, 214704.

(7) Radin, M. D.; Siegel, D. J. *Energy Environ. Sci.* **2013**, *6*, 2370.

(8) Yang, C.; Wong, R. A.; Hong, M.; Yamanaka, K.; Ohta, T.; Byon, H. R. *Nano Lett.* **2016**, *16*, 2969.

List of publications and conference presentations

Publications:

1. Wong, R. A.; Dutta, A.; Yang, C.; Yamanaka, K; Ohta, T.; Nakao, A.; Waki, K.;Byon, H. R.; Structurally tuning Li_2O_2 by controlling the surface properties of carbon electrodes: Implications for Li-O_2 batteries. *Chem. Mater.* 28, 8006-8015 (2016).

2. Yang, C.; Wong, R. A.; Hong, M.; Yamanaka, K.; Ohta, T.; Byon, H. R.; Unexpected Li_2O_2 _lm growth on carbon nanotube electrodes with CeO_2 nanoparticles in Li-O_2 batteries. *Nano Lett.* 16, 2969-2974 (2016).

3. Mercier, B. N.; Wong, R. A.; Thomas, L. M.; Dutta, A.; Yamanaka, K.; Yogi, C.; Ohta, T.; Byon, H. R.; A structured three-dimensional polymer electrolyte with enlarged active reaction zone for Li-O_2 batteries. *Sci. Rep.* 4, 7127 (2014).

4. Waki, K.; Wong, R. A.; Oktaviano, H. S.; Fujio, T.; Nagai, T.; Kimoto, K.; Yamada, K.; Non-nitrogen doped and non-metal oxygen reduction electrocatalysts based on carbon nanotubes: mechanism and origin of ORR activity. *Energy Environ. Sci.* 7, 1950-1958 (2014).

5. Oktaviano, H. S.; Wong, R. A.; Waki, K. The role of oxygen functionalities for enhanced oxygen reduction activity in carbon nanotubes. *ECS Trans.* 58, 1509-1516 (2013).

6. Tao, R.; Tomita, T.; Wong, R. A.; Waki, K. Electrochemical and structural analysis of Al-doped ZnO nanorod arrays in dye-sensitized solar cells. *J. Power Sources* 214, 159-165 (2012).

Conference presentations:

1. Wong, R. A.; Waki, K.; Byon, H. R.; Critical role of the surface characteristics of carbon nanotube-based electrodes for Li_2O_2 formation and decomposition and its implications for Li-O_2 batteries. Oral presentation, The 57th Battery Symposium in Japan, Nov 29-Dec 1 2016, Chiba, Japan

2. Wong, R. A.; Waki, K.; Byon, H. R.; Understanding the critical role of carbon nanotube surface chemistry towards the electrochemical behavior in Li-O_2 cells. Poster presentation, ECS PRiME. October 2-7 2016, Honolulu, USA

3. Wong, R. A.; Yang, C.; Dutta, D.; O, M.; Hong, M.; Yamanaka, K.; Ohta, T.; Byon, H. R.; Benchmarking metal and metal oxide promoters for oxygen evolution reaction

in Li-O_2 cells. Oral presentation, The 56th Battery Symposium in Japan. November 11-13 2015, Nagoya, Japan

4. Wong, R. A.; Waki, K.; Byon, H. R.; The role of defects and oxygen functionalities in carbon nanotube-based electrodes for the lithium-oxygen battery. Oral presentation, International Society of Chemistry, 66th annual meeting. October 4-9 2015, Taipei, Taiwan

5. Wong, R. A.; Byon, H. R.; Carbon stability in Li-O_2 batteries: An in situ gas analysis study. Oral presentation, Electrochemistry Society in Japan, Spring Meeting. March 15-17 2015, Yokohama, Japan

6. Wong, R. A.; Byon, H. R.; In situ gas phase characterizations in Li-O_2 batteries. Oral presentation, The 55th Battery Symposium in Japan. November 19-21 2014, Kyoto, Japan